Czech Technical University in Prague
Faculty of Electrical Engineering
Department of Electromagnetic Field

Millimeter wave radio over fiber and free-space optics

Doctoral thesis

Ing. Jan Spáčil

Ph.D. programme: Electrical Engineering and Information Technology P2612
Branch of study: Radioelectronics 2601V010
Supervisor: prof. Ing. Miloš Mazánek, CSc.
Supervisor Specialist: Ing. Tomáš Kořínek, Ph.D.

Prague, February 2024

Thesis Supervisor:
prof. Ing. Miloš Mazánek, CSc.
Department of Electromagnetic Field
Faculty of Electrical Engineering
Czech Technical University in Prague
Technická 2
166 27 Prague 6
Czech Republic

Thesis Supervisor Specialist:
Ing. Tomáš Kořínek, Ph.D.
Department of Electromagnetic Field
Faculty of Electrical Engineering
Czech Technical University in Prague
Technická 2
166 27 Prague 6
Czech Republic

Declaration

I hereby declare I have written this doctoral thesis independently and quoted all the sources of information used in accordance with methodological instructions on ethical principles for writing an academic thesis. Moreover, I state that this thesis has neither been submitted nor accepted for any other degree.

In Prague, February 2024

.....
Ing. Jan Spáčil

Abstract

Currently, the development of networks is focused on 5G technology, which is expanding in both the FR1 band (up to 6 GHz) and the prospective FR2 band (6 GHz to 71 GHz), due to the need for higher data transmission speeds and lower latencies. For effective utilization of 5G and potentially future 6G networks in the FR2 band, a densification of cells is necessary to compensate for the high free-space loss in the radio channel. In my work, I explore the possibilities of expanding and centralizing the infrastructure of 5G networks using fiber optics and free space optical technologies for fronthaul. I also include a study of characteristics and potential disruptive phenomena that can affect such networks, such as SNR (signal-to-noise ratio), dynamic range, phase noise, and atmospheric turbulences. This is achieved using both direct and indirect laser modulations, including the use of Electro-Absorption modulators(EAM), Mach-Zehnder modulators (MZM), and photonic frequency multiplication.

Keywords: Free space optics, Radio over fiber, 5G, LTE, Microwave Photonics.

Abstrakt

V současnosti se rozvoj sítí soustředí na 5G technologii, která se rozšiřuje jak v pásmu FR1 (do 6 GHz), tak i v perspektivním pásmu FR2 (6 až 71 GHz) kvůli potřebě vyšších přenosových rychlostí a nižších latencí. Pro efektivní využití 5G a potenciálně i budoucích 6G sítí v pásmu FR2 je nutné zahušťování buněk, aby se kompenzoval vysoký útlum volného prostoru v rádiovém kanálu. V mé práci zkoumám možnosti rozšíření a centralizace infrastruktury 5G sítí pomocí optických vláken a volného prostoru optických technologií (free space optics) pro fronthaul. Zahrnuji také studii vlastností a možných rušivých jevů, které mohou ovlivnit takové sítě, jako jsou SNR (signal-to-noise ratio), dynamický rozsah, fázový šum a atmosférické turbulence. Toho dosahuji použitím přímých i nepřímých modulací laserů, včetně použití elektroabsorpčních modulátorů, Mach-Zehnderových modulátorů (MZM) a fotonického násobení frekvencí.

Klíčová slova: Bezdrátové optické spoje, Rádio po Optickém Vlíkně, 5G, LTE, Mikrovlnná Fotonika.

Acknowledgements

I would like to express my heartfelt gratitude to everyone I have had the pleasure of collaborating with on this doctoral thesis and jointly advancing knowledge in the field of microwave photonics. Specifically, I extend my thanks to Dr. Jan Bohata and Dr. Dong Nhat Nguyen for their support and cooperation during research, and to Professor Stanislav Zvánovec for his continual support and expert advice throughout my dissertation writing process. I would also like to thank Professor Miloš Mazánek and Dr. Tomáš Kořínek for their support throughout my doctoral studies. Additionally, my gratitude goes to all other members of the Department of Electromagnetic Field.

Finally, I would like to thank everyone who has contributed to my academic and research journey, whether through words of encouragement or direct support.

List of Tables

List of Figures

List of Acronyms

5G 5th generation mobile network. iv, viii, ix, 1, 18–22, 24–27, 38, 39, 49, 68, 72, 73, 75, 76, 87

6G 6th generation mobile network. 87

ADC Analog-to-Digital Converter. 6, 8

APD Avalanche Photodiode. viii, 20, 21

ASE Amplified Spontaneous Emission. 15, 42, 47–49

B2B Back-to-Back. 70, 74, 75

BBU Centralized Baseband Units. 2, 3, 18–20, 45, 72, 87

BER Bit Error Rate. 22, 23

C-RAN Cloud radio access network. viii, 2, 3, 18, 87

CCU Climate Control Unit. 3, 8

CD Chromatic Dispersion. viii, 2, 3, 5, 17, 23, 29, 33, 34, 38, 49, 56, 67, 68, 72, 87

CW Continuous Wave. 30, 34, 58, 62, 63, 65, 66, 73

CWDM Coarse Wavelength Division Multiplexing. 24, 33, 34, 37, 38

DAC Digital-to-Analog Converter. 6, 9, 73

DL Downlink. x, 20, 24, 81–86

DML Directly Modulated Laser. 4, 10, 11, 21, 38, 39, 41, 42, 45, 47, 48, 57–61, 64, 81–83, 86, 88

DSB Double Sideband. 5, 8, 65, 68

DSB-SC Double Sideband-Suppressed Carrier. 23, 65, 72, 73

DSP Digital Signal Processing. 8

DWDM Dense Wavelength Division Multiplexing. 8, 38

EAM Electro-Absorption Modulator. iv, viii, 12, 13, 57, 58, 60

EDFA Erbium-Doped Fiber Amplifier. ix, 14, 15, 23, 38, 41, 42, 45–49, 51, 52, 56, 64, 66–68, 72, 74, 75, 77–83

EVM Error Vector Magnitude. viii–x, 19–21, 24–26, 35–38, 42–45, 47–53, 55–57, 62–65, 68, 70–72, 74, 77–82, 84–86

FKE Franz-Keldysh Effect. 13

FR Frequency Range. iv, v, xiv, xv, 1, 2, 18, 22, 24, 27, 72, 73, 75, 87, 88

FSL Free Space Loss. 59, 75

FSO Free Space optics. ix, 1, 2, 4, 9, 10, 24–26, 38, 39, 41, 43–46, 48–52, 65–67, 69–83, 86, 87

FWM Four-Wave Mixing. 5

HD-FEC Hard-Decision Forward Error Correction. 55, 56

IF Intermediate Frequency. viii, 4, 16, 19, 20, 72–74, 82, 83

IFoF Intermediate Frequency over Fiber. viii, 4, 19, 20

LNA Low-Noise Amplifier. 59, 74, 75

LO Local Frequency. 6, 16, 17, 50, 54, 57, 66, 72, 74, 82, 84, 86

LTE Long Term Evolution. 1, 24, 33, 35, 36, 47, 57, 63, 68, 81, 83–87

LTE-A Long Term Evolution Advanced. 39, 42, 45

MIMO Multiple-Input and Multiple-Output. 3, 8, 9, 19, 20, 22

mmW millimeter wave. viii, 1–3, 16, 18–20, 22, 23, 26, 27, 81, 82, 86, 87

MQW Multiple Quantum Well. 12

MZM Mach-Zehnder modulator. iv, viii, ix, 12–14, 16, 23, 30, 34, 50, 51, 57, 58, 60, 64–66, 69, 72, 73, 75, 81, 82, 86, 88

NR New Radio. 27, 72, 73, 75, 87

NRZ Non-Return-to-Zero. 23

OATT Optical Attenuator. 74, 77, 82–84

OFDM Orthogonal Frequency-Division Multiplexing. 24, 25, 35, 38, 39, 45, 47, 54, 56, 57, 68, 70, 81, 83

OFM Optical Frequency Multiplication. 3, 4, 88

OOK On-Off Keying. 23

PEP Peak Envelope Power. 73

QAM Quadrature Amplitude Modulation. viii, x, 20–22, 24, 25, 33, 35, 38, 39, 49, 50, 52–57, 62, 68, 70, 71, 77, 78, 81, 83–86

QCSE Quantum-Confined Stark Effect. 12, 13

QPSK Quadrature Phase Shift Keying. 21, 23, 25, 56, 68, 70, 71, 77

R&S Rohde & Schwarz. 30, 34, 35, 73, 74

RAN Radio Access Network. 19

RF Radio Frequency. viii, ix, 3–6, 8, 10, 12, 14, 16, 18, 20–23, 25–27, 33, 34, 37, 41, 44, 45, 51–53, 55–59, 62–65, 68, 72–74, 77, 79–81, 83

RIN Relative Intensity Noise. 7

RoF Radio over Fiber. viii, ix, xiv, 1, 3–9, 18–22, 24, 27, 38, 64, 73–75, 77, 78, 80, 81, 87

RoFSO Radio over Free Space optics. ix, xiv, 4, 24, 25, 27, 64, 74, 75, 78, 79, 87

RRH Remote Radio Head. 2–4, 8, 19–21, 45, 72, 74, 87

SBS Stimulated Brillouin Scattering. 5

SFDR Spurious-Free Dynamic Range. ix, xv, 12, 54, 60, 61, 65–67

SMF Single Mode Fiber. ix, 4, 5, 19, 20, 22–25, 30, 33, 34, 39, 41, 45, 46, 49–52, 54, 56, 59, 65–70, 72, 74–79, 81–86

SNR Signal-to-noise ratio. iv, ix, x, 7, 42–45, 53, 55, 59, 65, 70, 71, 77–81, 85

SRS Stimulated Raman Scattering. 5

SSB Single Sideband. 19

TDD Time Division Duplexing. 19, 20

TEC Thermoelectric Cooler. 41, 58, 59

TTD True Time Delays. 28

UL Uplink. x, 20, 24, 81–86

VDL Variable Optical Delay Lines. 29–31, 33

VNA Vector Network Analyzer. 30, 31, 34, 35, 41

WDM Wavelength Division Multiplexing. viii, 21, 25, 51

Contents

Chapter 1

Introduction

The increasing demand for higher data rates in mobile networks and the ever-increasing demands for lower communication latency are constantly increasing the requirements on our wireless transmission network. For this reason, 5G, as the successor to the commercially successful 4G in the form of Long Term Evolution (LTE), seeks to push the limits of 4G. In addition to using conventional frequency bands below 6 GHz (named Frequency Range-1 - FR-1), it also uses frequency bands from 6 GHz to 86 GHz (named Frequency Range-2 - FR-2). In these bands, the effort is to use unlicensed millimeter wave (mmW) bands. These mmW bands allow us to use large amounts of signal bandwidth that would be challenging to implement in the FR-1 bands below 6 GHz for a number of reasons (regulator restrictions, band splitting between different operators).

Of course, the use of bands above 6 GHz has its severely limitations. One of them is free space losses and losses when the signal passes through obstacles. This can be compensated to some extent by antenna arrays that can steer their beam and achieve relatively high gains while having a small physical size, due to the small wavelength at a given frequency. This limitation makes these bands for use in line-of-sight or only over small obstacles.

This leads to massive deployment of this 5G technology in FR-2 bands. To make this technology more competitive, the radio (modulation and signal generation) and processing parts of the receiver and transmitter can be moved away from where the antenna is located, centralizing the computation and signal generation. The transmission between the antenna part and this centralized part is done by means of analog radio signal transmission over optical fiber (Radio over Fiber - RoF). Further centralization in mobile communication networks can be pursued in scenarios where deploying fiber optics is either not cost-effective or feasible. Such situations may arise in contexts where laying fiber optics is impractical, such as when it involves extensive demolition or alteration of existing infrastructure like roads and pathways or in rural areas. In these cases, employing Free

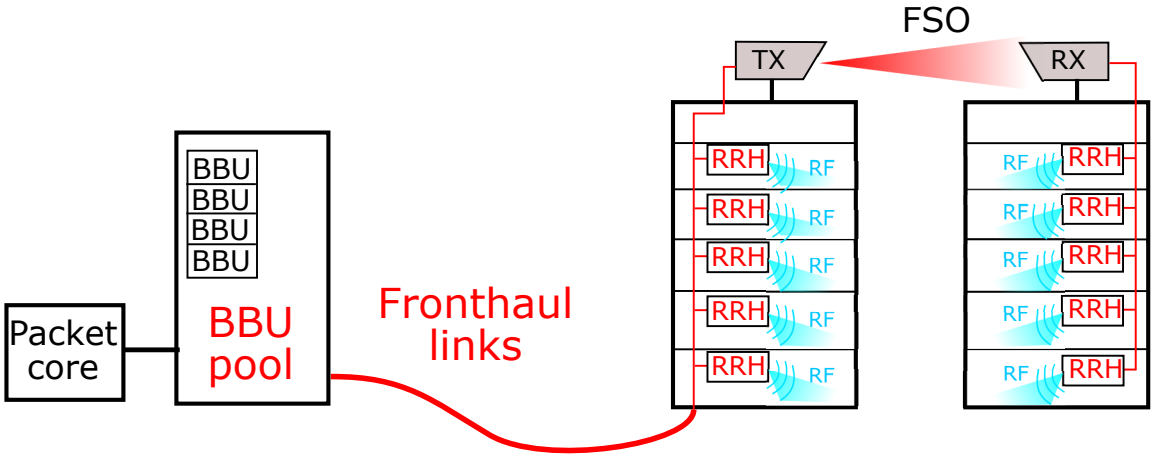

Figure 1.1: Cloud radio access network (C-RAN)

Space optics (FSO) emerges as a viable alternative. FSO technology offers a solution that circumvents the physical limitations and financial constraints associated with fiber optic installations, providing an effective means of optical data transmission without the need for physical cabling. With this centralization, resources can be aggregated and reallocated as needed and better energy efficiency can be achieved with this solution. [1]

The centralized network described above is called cloud radio access networks (C-RAN), or also centralized radio access networks [2]. A representation of what such a network might look like is shown in Figure 1.1. The signal is processed and generated in a centralized baseband units (BBU) pool. In each BBU, the generated analog signal is converted to an optical modulated signal in a fiber optic and further distributed via a fronthaul link to the location where the signal is to be transmitted (office building, shopping mall, etc.). There, in a relatively simple Remote Radio Head (RRH), it is converted by detection PIN diode into an mmW signal which is amplified and radiated by an antenna as required. The received signal at each RRH is processed similarly way back to BBUs pool.

The maximum distance of such a C-RAN is limited by the budget for the total delay over the entire link, chromatic dispersion (CD) and attenuation of fiber. This means both the route over the optical fiber and then the route over the air from the RRH and the receiver. The path in free space in the FR-2 bands above 6 GHz is not very long anymore, due to the high attenuation in free space and the obstacles that generate large attenuations, so the main limit is the length of the optical fiber. The maximum latency for high-priority fronthaul can be 100 µs according to [3]. For medium-priority fronthaul and low-priority fronthaul it is 1 ms [3]. These latency values are quite strict, so any extra delay in the RoF could mean that this limit is not met. For this reason, it is preferable to use analog RoFs where the delay on the components, away from the length of the fiber, is minimal.

This thesis explores the viability of employing both single-mode fibers for the distribution of high-frequency radio and mmW signals to streamlined remote radio antenna units. The study delves into an alternative RoF technique known as optical frequency multiplication (OFM) and photonic mixing. It has been conclusively demonstrated that OFM exhibits a high degree of CD tolerance, enabling its application in scenarios where traditional Intensity Modulation-Direct Detection (IM-DD) systems face challenges. OFM's remarkable characteristic is its ability to facilitate single-mode fiber transmission links that surpass 50 kilometers in length, a performance that outperforms IM-DD systems. [4] This significant extension in the transmission range is particularly noteworthy in contrast to IM-DD systems, which are prone to CD induced amplitude suppression, thereby limiting their effectiveness over extended distances. The resilience of OFM against CD not only enhances the reach of mmW signals but also underscores its potential to revolutionize long-distance communication scenarios, providing a more robust and reliable solution for RRH. This aspect further underscores the importance of exploring and harnessing the capabilities of OFM in advancing telecommunications technologies [5].

1.1 Remote Radio Head based base station architecture

The C-RAN concept with RRH has been introduced in recent years.[6] It is an architecture in which there is one central BBU pool and N distributed RRHs. Figure 1.1 shows an example of such an architecture. The RRH contains an optics-to-RF converter, a power amplifier, a low-noise amplifier for reception, and antennas. The signal itself is processed in the BBU pool. The massive Multiple-Input and Multiple-Output (MIMO) array can be deployed, so the number of individual components of the RRH will increase with N_{tx} transmit and N_{rx} receive MIMO channels.

The adoption of this particular architectural framework can be attributed to several compelling benefits. One factor is the potential for enhanced spectrum utilization, allowing for a more efficient allocation based on the actual utilization within the RRH area. By dynamically adjusting and optimizing spectrum allocation, this architecture provides a responsive and adaptive solution to the varying demands and traffic patterns in the RRH domain.[7]

Furthermore, this architecture boasts lower power consumption and better energy efficiency per transmitted bit as shown in Figure 1.2. The climate control unit (CCU) must also be taken into account in the calculation. What is most important to us is that as the number of RRHs increases, the energy efficiency increases over conventional macro-cells.[8]

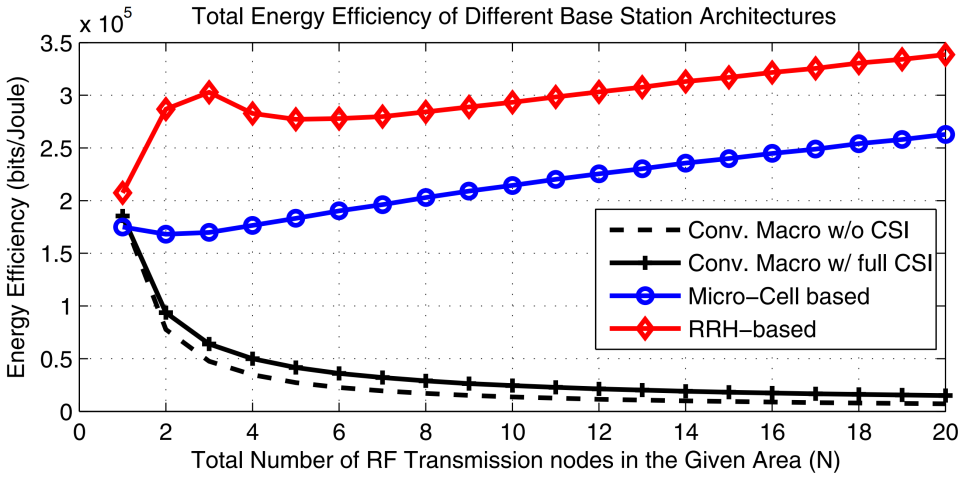

Figure 1.2: BS energy efficiency for varying N with $P_{\mathrm{Tx}} = 10\,\mathrm{W}$ [8]

1.2 Radio over fiber

Analog RoF can be categorized into three subgroups. RF over fiber, where the broadcasted signal is transmitted directly without any frequency conversion. Next, IF over fiber (IFoF), where frequency conversion is required at the RRH. Additionally, in the case of IF over fiber, photonic mixing can also be employed. Going forward, we will focus solely on RF over fiber and IF over fiber with optical mixing and OFM.

In general, RoF can be divided into several component blocks:

- Electrical to optical signal converter
- Optical fiber as the transmission medium
- Optical to electrical signal converter

Where the electrical to optical signal converter can be a directly modulated laser (DML, discussed in more detail in chapter 1.4.1) or the optical signal can be externally modulated (chapter 1.4.2).

As the transmission medium, either multi-mode optical fiber or single mode fiber (SMF) can be used. Throughout this work, SMF is consistently employed and when FSO is used it is referred as RoFSO or medium is specified. Optical fiber introduces significant impairments.

Firstly, there is the attenuation of the optical signal as it propagates through the fiber due to impurities, manifesting as Rayleigh scattering. The typical value of this attenuation is $0.2\,\mathrm{dB\,km^{-1}}$.

Secondly, chromatic dispersion in the fiber, where the refractive index $n(f)$ varies with the frequency f of the optical signal. This is discussed in more detail in chapter **??**.

Thirdly, optical fibers and generally dielectric materials can be polarized by an electric field. The nonlinearity of the optical fiber stems from the fact that this polarization is a nonlinear function of the intensity of the electric field $E(t)$. This leads to a nonlinear refractive index, which depends on the total passing power $P(t)$. This time-dependent power $P(t)$ can cause parasitic phase modulation of the passing optical signal.

Furthermore, optical fibers exhibit a nonlinear phenomenon when in a fiber is more than one frequency component where an optical signal is a new frequency components are generated. This phenomenon is known as Four-Wave Mixing (FWM). Other nonlinear optical phenomena are Stimulated Brillouin Scattering (SBS) and Stimulated Raman Scattering (SRS). SRS involves the transfer of an optical signal from one frequency to a lower frequency signal in the forward direction of propagation. SBS entails the conversion of an optical signal into the backward direction at a frequency higher than that of the original signal. This is a rough list of nonlinear phenomena that are relevant to RoF. [9]–[11]

Next significant impairment of optical fiber is CD, which is another name for group-velocity dispersion, in lightwave systems arises from variations in the group velocity within a fiber due to changes in optical frequency. CD can significantly impair the performance of these systems. The standard measure of CD parameter, widely used in the lightwave community, is denoted as D, with units of $\mathrm{ps\,nm^{-1}\,km^{-1}}$.

In RoF systems using intensity-modulated signals, which can be approximated by Double Sideband (DSB) modulation, the primary impact of CD is the differential phase shift experienced by frequencies in the sidebands around the optical carrier at λ_0. This phase shift disparity leads to the subtraction of signals ($\pm\Delta f_{\mathrm{RF}}$) in the modulated DSB sidebands. For a pure DSB signal, the resultant waveform can be modeled using the equation provided in [4]:

$$P_{\mathrm{RF}} \approx \cos^2 \frac{\pi L D \lambda_0^2 f_{\mathrm{RF}}^2}{c} \tag{1.1}$$

Where P_{RF} is the output RF power and L is the length of SMF. The frequency response of the detected signal exhibits periodic attenuations in the RoF transmission. These periodic attenuations are influenced by both the wavelength of the optical carrier and the length of the SMF employed.

It is important to note that this modeling is applicable only to pure DSB modulation (or intensity modulation). Certain methods of generating modulated signals, such as direct-modulated lasers, may introduce parasitic frequency modulation. In such cases, the effective transmission characteristics become reliant on the ratio between the intensity modulation index m_i and the frequency modulation index m_f. This relationship and its implications on transmission are elaborated in [12].

Photodetection is the process by which an optical signal is converted into a corresponding current. This process is referred to as square-law photodetection, where the output current $I(t)$ is proportional to the received power P_{RX}. There are two types of detection: direct detection and coherent detection. Throughout this work, we focus primarily on direct detection.

Direct detection can be described by equation $I(t) = R\,|E_{\mathrm{RX}}(t)|^2$. Where R is responsivity of photodetector. It follows that the intensity of the received signal $|E_{\mathrm{RX}}(t)|^2$ must be modulated in such a way that the signal can be reconstructed by this detector.

On the other hand, in coherent detection, the received optical signal is mixed with the output of a laser, which serves as a local oscillator (LO). This is followed by photodetection. Mathematically, this can be expressed as $I(t) = R\,|E_{\mathrm{RX}}(t) + E_{\mathrm{LO}}(t)|^2$, where $E_{\mathrm{RX}}(t)$ is the received electric field intensity, and $E_{\mathrm{LO}}(t)$ is the intensity of the LO's electric field. The breakdown of this equation gives:

$$\begin{aligned} I(t) = R\left|A_{\mathrm{RX}}e^{j\omega_{\mathrm{RX}}t+\phi_{\mathrm{RX}}} + A_{\mathrm{LO}}e^{j\omega_{\mathrm{LO}}t+\phi_{\mathrm{LO}}}\right|^2 \\ = R\left[A_{\mathrm{RX}}^2 + A_{\mathrm{LO}}^2 + 2\,|A_{\mathrm{RX}}|\,|A_{\mathrm{LO}}|\cos\left(\omega_{\mathrm{diff}}t + \phi_{\mathrm{RX}} - \phi_{\mathrm{LO}}\right)\right] \end{aligned} \quad (1.2)$$

where $\omega_{\mathrm{diff}} = \omega_{\mathrm{RX}} - \omega_{\mathrm{LO}}$, A_{RX} and A_{LO} are amplitudes of recieved signal and LO signal, ϕ_{RX} and ϕ_{LO} are phased of the two signals. This equation represents the specific mathematical relationship for output current of the coherent detection process. As can be seen, we can use coherent detection for frequency shifting of detected signal.

Direct detection is simpler and more cost-effective because it requires only a standalone detection diode.

1.2.1 Analog vs. digital radio over fiber

RoF technology is commonly classified into two distinct types: analog and digital. Within the analog RoF framework, the RF signal undergoes direct or external modulation to transform it into an optical signal (E/O converter). This optical signal is then transmitted over an optical fiber in its analog form, and at the termination point, it is detected by a suitable optical-to-RF converter, typically a PIN diode. The principle is shown on Figure 1.3b.

Conversely, in a digital RoF system, the RF signal takes a different route. Initially, the RF signal is sampled and quantized into discrete levels in analog-to-digital converter(ADC), converting it into a digital signal. This digital signal is subsequently modulated into an optical signal for transmission over the optical fiber. At the receiving end, the optical signal is detected and transformed back into an analog signal through the use of a digital-to-analog converter(DAC). The principle is shown on Figure 1.3a.

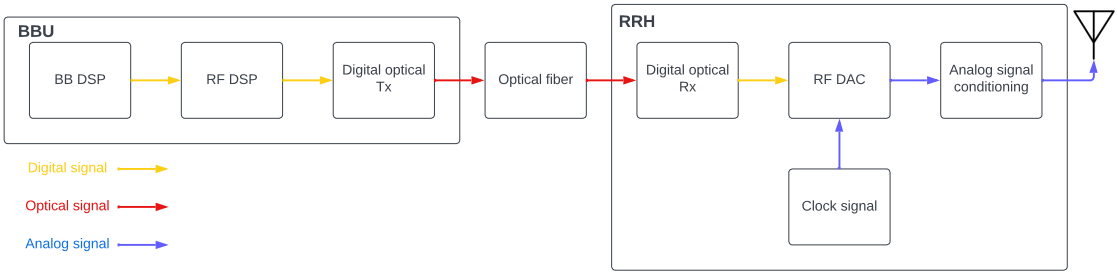

(a) Digital RoF

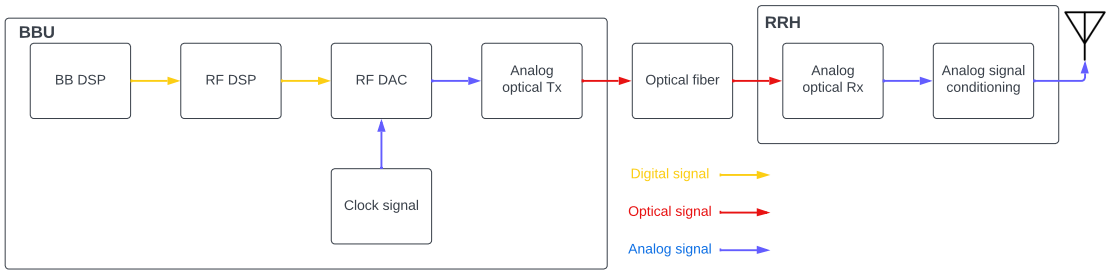

(b) Analog RoF

Figure 1.3: Analog and digital RoF block diagram.

One notable advantage of digital RoF lies in its enhanced resistance to Signal-to-noise ratio (SNR) reduction during transmission. This resilience is attributed to the incorporation of self-correcting codes in the digital signal. As long as a minimum required signal level is maintained, a digital RoF link behaves as a transparent link, providing a robust and reliable communication channel.

In contrast, the analog RoF transmission is inherently analog, and any variations in attenuation, gain, noise, or distortion have a direct impact on the detected signal at the output of the PIN diode. The sensitivity of analog RoF to these factors underscores the challenges associated with maintaining signal integrity over extended transmission distances.

Various sources contribute to noise in analog RoF systems, including the relative intensity noise (RIN) of the laser, the phase noise of the laser and the shot noise of the detection diode. Understanding these sources of noise is crucial for optimizing the performance of analog RoF systems and mitigating the impact of external factors on signal quality.

Upon careful consideration of the advantages and disadvantages presented in this comparison, the question naturally arises: why should one delve into analog RoF? The answer lies in a series of distinct advantages that position analog RoF as a compelling option, notably its low cost, high spectral efficiency, excellent delay (only the speed of

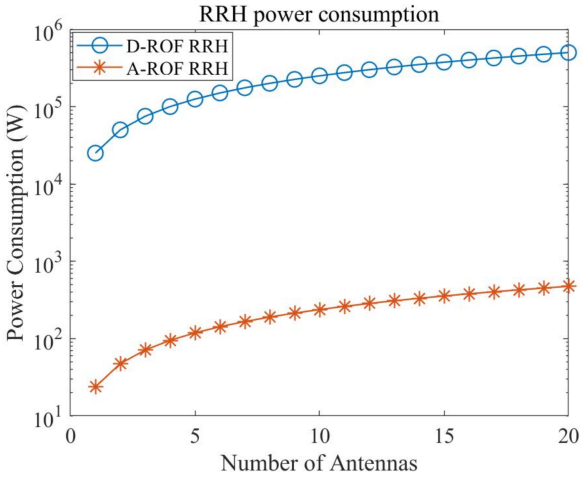

Figure 1.4: Comparison of RRH consumption for analog RoF and digital RoF.[13]

propagation) and impressive power efficiency [6].

The economic appeal of analog RoF becomes particularly pronounced when assessing the cost factor. Digital RoF may not present a financial hurdle in isolation, unless, of course, the deployment scale is massive, involving a substantial number of RRHs. Each RRH, in the context of massive MIMO systems, such as a 16 MIMO configuration, necessitates a corresponding set of 16 separate digital RoFs for communication in a single direction. This implies a considerable amount of digitizing hardware, especially on the RRH side, where sharing and dynamic allocation become impossible requirements.

Additionally, the practicality of analog RoF is emphasised by its compatibility with Dense Wavelength Division Multiplexing (DWDM), a critical consideration for optimizing spectral efficiency. In DWDM systems, individual channels are spaced at grid of 100 GHz or 50 GHz. Analog RoF, leveraging its twice the bandwidth of the optical double sideband (DSB) signal compared to the RF signal, seamlessly fits into this spectrum. In contrast, digital RoF faces challenges in bandwidth requirements. The optical signal's bandwidth must be approximately 40 times greater than its analog counterpart to accommodate the sampled signal and its quantization, preserving the dynamic range. This requirement limits its adaptability to DWDM configurations [13].

To compare the consumption of analog RoF and digital RoF, the model published in [8] is used, where the total consumption is broken down in quite a bit of detail. It is necessary to split the consumption between CU and RRH. The CU consumption consists of the power consumption of CCU, the power supply unit, the CU computing unit which includes the MIMO DSP, baseband modulation, carrier modulation, the ADC in the case of digital RoF and the E/O converter.

On the other hand, the RRH has power consumption in the O/E converter, power supply unit, RRH control unit, electronic bandpass filter and in the case of digital RoF

also has power consumption in the DAC.

When [13] conducted a comparative analysis of an analog RoF system with a transmission rate of $20\,\mathrm{Gbit\,s^{-1}}$ against its digital RoF counterpart, which utilizes sampled data with a transmission rate of $200\,\mathrm{Gbit\,s^{-1}}$ to achieve the same data throughput, the superior energy efficiency of the analog RoF system became evident. This advantage is illustrated in Figure 1.4, as depicted in the corresponding graph in dependence on number of antennas in MIMO.

1.3 Radio over FSO

FSO communication, conventionally utilized for point-to-point optical terrestrial transmission, has recently garnered attention for its potential applications in satellite-to-satellite communication, satellite-to-ground station links, and connections between satellites and High Altitude Platforms (HAP).[14] Particularly noteworthy is its role as a viable alternative to fiber optics, especially in areas lacking established fiber optic infrastructure, where the installation is challenging, or in economically unviable scenarios, such as remote rural areas.

The distinct advantage of FSO technology, as compared to radio links, lies in its utilization of license-free bandwidth, offering heightened security, elevated data rates, and substantial bandwidth. Furthermore, FSO's intrinsic transparency as a transmission medium underscores its independence from any specific protocol transmitted over the channel. This flexibility positions FSO as a versatile solution capable of adapting to diverse communication protocols and technologies, adding to its appeal in evolving telecommunication landscapes.

Despite these advantages, the performance of FSO systems can be susceptible to degradation caused by environmental factors. Primarily influenced by atmospheric conditions, FSO is sensitive to various weather phenomena, including atmospheric turbulence, fog, rain, and snowfall. Atmospheric turbulence, characterized by random changes in refractive index along the FSO beam path, is a critical factor influencing FSO performance. Fluctuations in temperature, pressure, and humidity contribute to changes in refractive index, with temperature variations exerting a predominant effect. The overall impact of turbulence on the received signal is influenced by factors such as the wavelength of the optical signal, the length of the link, and a constant parameter C_n^2 (refractive index structure parameter or scintillation index) which quantifies the strength of turbulence along the entire transmission path. The refractive index structure parameter, as defined by Andrews [11], is expressed as follows:

$$C_n^2 = \left(7.9 \times 10^{-6} \frac{P}{T^2}\right)^2 C_T^2 \tag{1.3}$$

where P represents the atmospheric pressure in millibars, T denotes the absolute temperature in Kelvin, and C_T^2 is the thermal structure parameter. The thermal structure parameter is defined as:

$$C_T^2 = \frac{(T_1 - T_2)^2}{d^{2/3}} \tag{1.4}$$

Here, T_1 and T_2 are temperatures measured at two adjacent points separated by a distance d.

The measure of turbulence strength in the atmosphere is given by the plane wave Rytov variance:

$$\sigma_R^2 = 1.23 k^{\frac{7}{6}} C_n^2 L^{\frac{11}{6}} \tag{1.5}$$

Where $k = \frac{2\pi}{\lambda}$ is the wave number, L is length of the propagated FSO link. Turbulent regime in the atmosphere is weak, moderate, strong and extremely strong when σ_R^2 is $\ll 1$, ~ 1, > 1 and $\gg 1$ respectively. [11], [15]

1.4 Components of the RoF

This section gives a cursory description of the optical components we used in our experiments.

1.4.1 Directly modulated laser

DMLs offer higher power efficiency in generating optical signals compared to transmitters that utilize external modulators. They also benefit from a compact footprint and cost-effective manufacturing.

In DMLs, the injection current is modulated by the RF signal, resulting in a modulated output of optical power. Therefore, in DMLs, the laser simultaneously serves as both the optical source and the modulation device.

Laser diodes can be modulated at high frequencies, suitable for a wide range of applications. Standard diodes can be modulated effectively up to 1 GHz, while specialized ones can achieve significantly higher frequencies, up to 108 GHz[16]. The primary limitations are parasitic inductance and capacitance, and the intrinsic speed of the laser mechanism, which is influenced by transition rates and the relaxation oscillation peak.[1]

[1]Lasers work by running electrons through a loop consisting of three or four quantum transitions. Each of these transitions has its own time constant, which as any circuits person knows, can lead to instability due to accumulated phase shifts. Good lasers have one dominant time constant, namely, the long lifetime of the upper state of the laser transition. The other time constants lead to excess phase

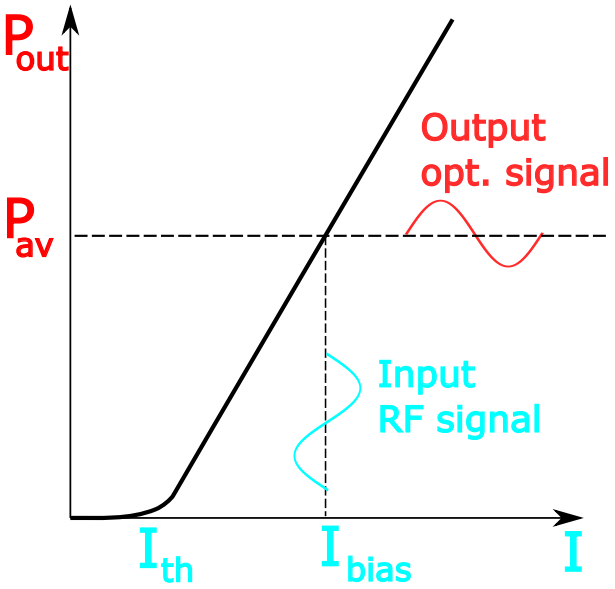

Figure 1.5: Ideal PI curve of a laser diode.

The modulation sensitivity of a laser increases near the relaxation peak but diminishes rapidly beyond it. However, operating in this region is generally not desirable. The relaxation frequency, which dictates the maximum modulation frequency, typically increases with the operating current up to a point near the laser's maximum output power, after which it slightly decreases.

A significant challenge in modulating diode lasers lies in the concurrent modulation of intensity and frequency, which complicates the generation of pure amplitude modulation or frequency modulation through the current tuning.[17], [18]

Intensity modulation of DML can be expressed as:

$$P_{\mathrm{LD}}(t) = s_{\mathrm{LD}} \left(I_{\mathrm{bias}} + I_{\mathrm{sig}}(t) - I_{\mathrm{th}} \right) \tag{1.6}$$

Where $P_{\mathrm{LD}}(t)$ is the output intensity modulated signal, s_{LD} is the laser slope efficiency expressed in $\mathrm{W\,A^{-1}}$, I_{bias} is the DC bias current, $I_{\mathrm{sig}}(t)$ is the signal current and I_{th} is the laser threshold current. This transfer function is illustrated in Figure 1.5. This example curve is strictly linear.

1.4.2 External modulators

External modulation in laser systems involves imposing modulation onto the laser signal after the generation of light. This process is crucial in photonic systems where optical signals, characterized by high carrier frequencies, are transmitted through dielectric

shift, which generally causes ringing in the laser output and level populations whenever a sharp change in pumping occurs, just like a feedback amplifier with too small a phase margin. It isn't really oscillation, but it does limit the modulation response of the laser, and it causes excess noise near the peak. [17]

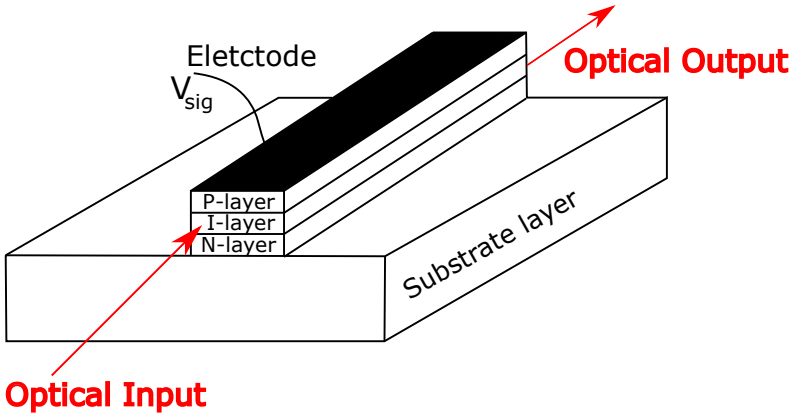

Figure 1.6: The semiconductor EAM.

waveguides rather than metal conductors. This attribute of photonic systems inherently offers an advantage in terms of bandwidth and signal integrity.

For high-fidelity analog applications, it is essential to have an electrical-to-optical transfer characteristic that is highly linear. The lithium niobate Mach-Zehnder modulator (MZM) interferometric intensity modulator stands out in this respect. It offers near-zero second-order distortion, a consistent and reproducible electrical-to-optical transfer characteristic, and is a technology that is both technologically advanced and commercially mature. MZM devices are suitable for a broad spectrum of applications; however, for certain high-performance systems that demand extensive bandwidth, these devices require relatively large modulating voltages. This requirement can lead to RF performance challenges, including increased insertion loss and a higher noise figure. Additionally, the predictable transfer characteristic of the MZM modulator poses limitations on device linearization, which is key to minimizing RF distortion products and improving RF spurious-free dynamic range (SFDR).

In contrast, the quantum-well Electro-Absorption Modulator (EAM) presents several advantages. Its compact form factor, potential for optical and electronic integration, reliability in space applications, and the versatility provided by semiconductor bandgap engineering are notable. These attributes allow for the tailoring of the transfer characteristic to optimize RF performance, making the EAM an attractive alternative in scenarios where traditional MZM modulators may fall short.

1.4.3 Electro-absorption modulator

As illustrated in Figure 1.6, the EAM is fundamentally a p-i-n diode structure. Its intrinsic layer acts as an optical waveguide, which incorporates single or Multiple Quantum Wells (MQWs) as the optically active elements of the modulator. These MQWs are subject to the Quantum-Confined Stark Effect (QCSE), whereby applying a reverse bias voltage

induces a redshift in the confined energy levels. [19]

The modulation of light absorption is achieved by applying a voltage across the waveguide. In the absence of an electric field, the semiconductor remains transparent to light. However, upon the application of voltage, the bandgap energy decreases, leading to light absorption once the photon energy surpasses the bandgap energy. This process attenuates light transmission. By modulating the voltage, both the material's absorption properties and the output light intensity can be controlled. Since most of the energy is transformed into heat, appropriate thermal management solutions are crucial for precise modulation and to mitigate undesirable thermal effects.

The EAM's robust absorption characteristics enable device lengths as short as 100 µm to achieve almost complete optical absorption, suggesting the potential for high-speed operation.

Franz-Keldysh Effect and Quantum-Confined Stark Effect: The Franz-Keldysh Effect (FKE) is a tunneling phenomenon. An applied electric field induces band bending in a semiconductor, allowing electron and hole wavefunctions to tunnel slightly into the forbidden energy gap, resulting in a redshift of the absorption edge. The QCSE extends the FKE to quantum well structures. In addition to the reduced interband energy difference due to band-bending, the confinement of electrons and holes within the well region diminishes energy level broadening. Consequently, the QCSE leads to sharper absorption edges compared to bulk materials. These effects are pivotal considerations in the design of electro-absorption modulators. [20]

1.4.4 Mach-Zehnder modulator

The MZM is an interferometric device constructed from materials exhibiting a pronounced electro-optic effect, such as Lithium Niobate (LiNbO3), Gallium Arsenide (GaAs), or Indium Phosphide (InP). When electric fields are applied to its arms, the optical path lengths within these arms are altered, leading to phase modulation. The process of recombining the two arms, each undergoing differing phase modulations, effectively transforms the phase modulation into intensity modulation.

Within the MZM, the incoming optical signal is split into two distinct paths and subsequently recombined into a single output (Figure 1.7a). This recombination results in either constructive or destructive interference, contingent upon the modulating input voltage V (specifically electric intensity). The intensity of the output optical signal P_O from the MZM is determined by the following relationship:

$$P_O = P_I L_{\text{mzm}} \left[1 + \cos\left(\frac{\pi V}{V_\pi} + \phi_b \right) \right] \tag{1.7}$$

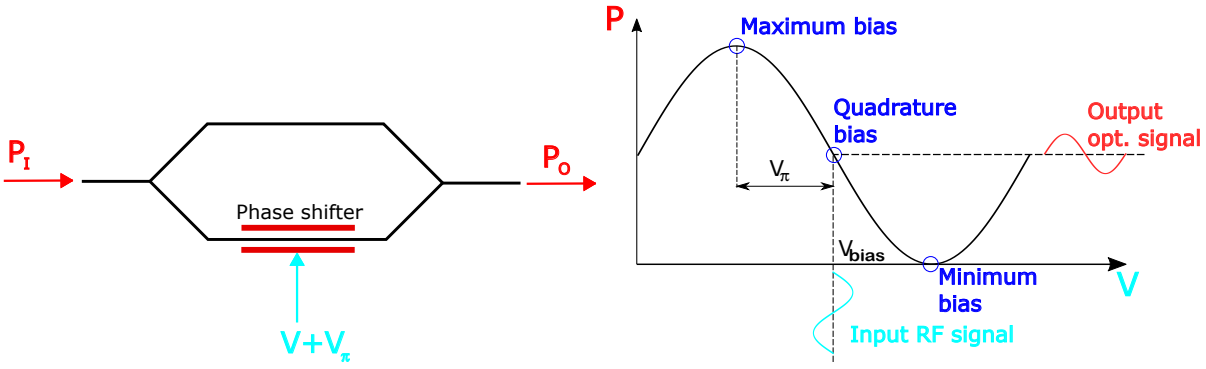

(a) MZM shematic structure. (b) MZM raised cosine transfer characteristic.

Figure 1.7: Mach-Zehnder modulator.

Where L_{mzm} is loss in MZM, V is input modulation voltage, V_π is the voltage requred to vary output optical signal from a minimum to a maximum and ϕ_b is a bias phase (the lengths in a real device are never matched at zero applied bias). [18]

The MZM demonstrates a raised-cosine transfer function (Figure 1.7b) when utilized for electro-optic modulation. Due to the inherent nature of this transfer function, which is not a purely linear conversion, nonlinear distortion becomes a factor in the modulation process.

The Mach-Zehnder Modulator (MZM) is characterized by its capability to handle large maximum optical input power, typically around 20 dBm, and significant RF input power, typically up to 24 dBm. The operating frequency band for a standard MZM typically extends up to 40 GHz. However, state-of-the-art reaching and exceeding 110 GHz, as documented in [21].

1.4.5 Erbium-Doped Fiber Amplifier

First reported in 1987[22], [23], the Erbium-Doped Fiber Amplifier (EDFA) has, in a relatively short time, revolutionized the optical communications industry. Prior to the advent of optical amplifiers, typical optical transmission systems were comprised of digital transmitters and receivers, with spans of transmission optical fiber interspersed with optoelectronic regenerators.

The EDFA uniquely amplifies lightwave signals within the optical domain, maintaining the integrity of the signal throughout. In optical fiber transmission systems, EDFAs serve multiple roles: they can function as power amplifiers to enhance transmitter power, as repeaters or in-line amplifiers to extend system reach, and as preamplifiers to improve receiver sensitivity.

A significant application of optical amplifiers lies in supporting wavelength-division multiplexing, a technique that combines and transmits signals of various wavelengths

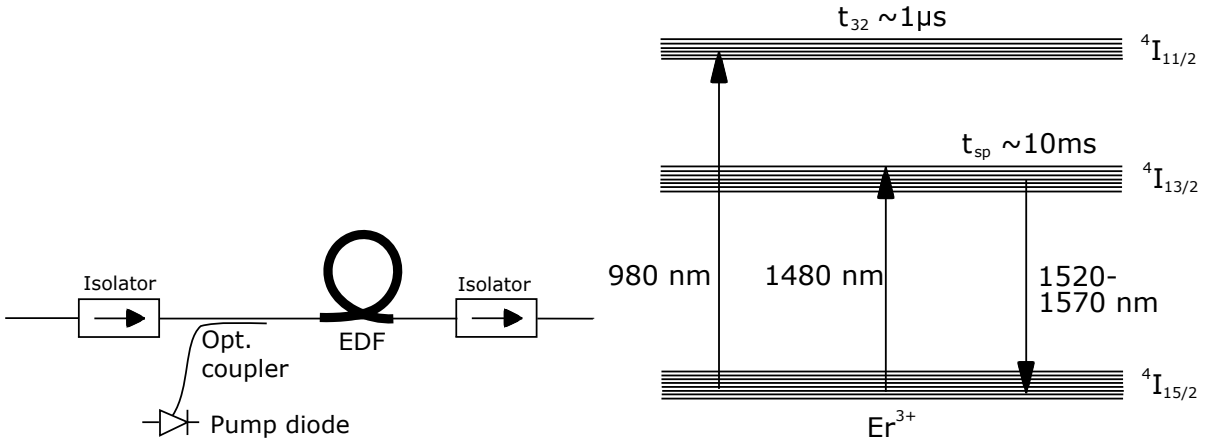

(a) EDFA configuration. (b) Erbium energy-level scheme.

Figure 1.8: Basic erbium-doped fiber amplifier.

concurrently on the same transmission fiber. At the heart of an EDFA is its erbium-doped fiber, typically a single-mode fiber with a core doped with erbium ions. The circular symmetry of the fiber core and the random orientation of the erbium ions within the fiber's glass matrix endow EDFAs with polarization-independent gain, a key advantage of these amplifiers.

The basic EDFA configuration, illustrated in Figure 1.8a, integrates an erbium-doped fiber into the signal transmission path of an optical fiber communications system, along with a pump light source. This pump light, which may either counterpropagate or co-propagate with the signal light, excites erbium atoms from the ground state $^4I_{15/2}$ to a higher energy state $^4I_{11/2}$ (depicted in Figure 1.8b). These atoms then quickly relax to the metastable state $^4I_{13/2}$, where they can linger for an extended duration. Signal photons passing through stimulate these atoms in the metastable state to emit photons at the same frequency, a process known as stimulated emission.

Amplifier noise primarily arises from spontaneous emission, where an atom in the metastable state spontaneously descends to the ground state, emitting a photon. This emission, occurring at a frequency close to the signal, can be further amplified, resulting in Amplified Spontaneous Emission (ASE).

Besides the erbium-doped fiber, a crucial component for EDFAs is the pump source, which provides light at the appropriate wavelength and sufficient power to activate the amplifier. Laser diodes, particularly those at 1480 nm and 980 nm wavelengths, are commonly employed as pump sources. Their ease of manufacture has significantly contributed to the swift integration of EDFAs as practical optical amplifiers in optical communications. [9], [24], [25]

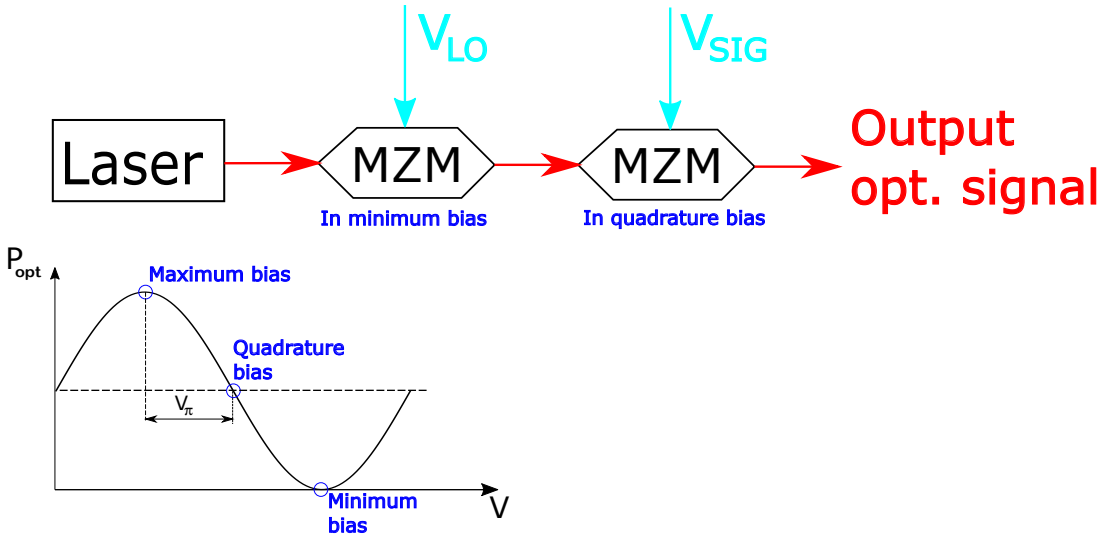

Figure 1.9: An optical scheme for frequency doubling with low frequency another MZM for IF data modulation.

1.4.6 Photonic mixing

Mixers are RF devices that up-convert and down-convert useful signals at the receiver and transmitter. Generally, diodes and transistors are used for this purpose at microwave and mmW frequencies however, photonic mixers are an alternative approach at optical frequencies featuring wide bandwidth. Photonic frequency mixing is a technique that enables the frequency conversion of any given signals in the optical domain to new frequency either in mmW, RF, IF or a baseband. A new signal is generated after the beating two input frequencies at the photodiode.

Equation describes photonic mixing:

$$P_{out}(t) = \frac{\alpha(P_1+P_2)}{2} + \frac{(P_1+P_2)m\alpha}{2}\sin(\omega_{RF}t) + \alpha\sqrt{P_1P_2}\cos(\omega_{LO}t+\phi_{12}(t)) + \frac{m\alpha\sqrt{P_1P_2}}{2}\sin\left[(\omega_{LO}\pm\omega_{RF})t+\phi_{12}(t)\right] \quad (1.8)$$

where $m = \frac{\pi V_0}{V_\pi}$, V_0 is the amplitude of RF signal, V_π is the half-wave voltage of the modulator at the RF input, $P_1 + P_2$ are the output powers of the two laser modes with frequency difference ω_{LO} and relative phase fluctuation $\phi_{12}(t)$, ω_{RF} is RF signal frequency and α is scaling factor. The first term represents the DC current, the second term is the RF signal, the third is LO signal, and the forth terms of equation are the upconverted and downconverted products. The phase noise of the upconverted and downconverted signals given by $\phi_{12}(t)$, which depends on the relative stability of the laser.[26], [27]

Furthermore, photonic mixing offers the potential for improved performance in terms of signal-to-noise ratio and linearity. Optical intensity modulators used in photonic mixers exhibit high linearity and low-noise characteristics, resulting in enhanced signal quality

compared to traditional diode-based mixers.[27]

The local electrical signal (generated prior to fiber propagation) experiences phase-noise degradation similar to a standard electronic frequency multiplier. In addition, the power spectral density of the remote electrical (after having propagated in a given length of optical fiber) signal is impacted by the linewidth of the optical carrier and the CD effect of the transmission fiber.[28]

One implementation of photonic frequency mixers can be done using optical two cascaded intensity modulators, as in Figure 1.9, in a heterodyne optical carrier source configuration. When the first modulator is set in minimum bias, it suppresses the carrier frequency and generate two tones at $\pm 2\omega_{LO}$. The second modulator is set in quadrature bias, and its signal is beat at the photodiode with $\pm 2\omega_{LO}$ and generate converted signal with doubled LO frequency. This configuration is photonic frequency mixer with frequency doubling.[26]

Chapter 2

State of the art

The deployment of wireless networks necessitates the widespread installation of small cells, i.e., up to femto-cells, to ensure comprehensive coverage. In this context, the simplification of remote cell sites emerges as a critical factor for enhancing both cost and energy efficiency. The C-RANs have been introduced as a promising solution to facilitate the support of small-cell-based networks.[29] In C-RAN architectures, essential signal processing functions, including those of BBUs, are centralized within pools located at center stations (CSs). This centralization allows remote cell sites to be relegated to performing straightforward tasks such as signal amplification and managing radio front-ends [30].

The mmW spectrum, particularly from 20 GHz to 30 GHz band, marks a significant milestone as the first spectrum above 6 GHz to be harnessed for mobile networks. This advancement, however, brings forth several challenges, notably the substantial attenuation approximately $3\,\mathrm{dB\,m^{-1}}$ encountered when RF signals traverse metallic cables, which inherently constrains the feasible transmission distance. RoF technology has been proposed as a viable solution to mitigate this limitation, offering a means to extend the reach of these high-frequency signals [31].

2.1 Overview of RoF experiments in FR1 and FR2-1 Bands

In this chapter, we establish a overview of diverse experiments focusing on RoF within the Frequency Range 1 (FR1) band and, notably, the FR2-1 band. The objective is to compile a summary of research works that have addressed this subject, highlighting the methods employed to achieve the outcomes reported in these studies.

The significance of RoF technology, especially in the context of FR2-1, lies in its potential to enhance the performance and efficiency of 5G networks. By examining the methodologies and results of previous experiments, this chapter aims to provide valu-

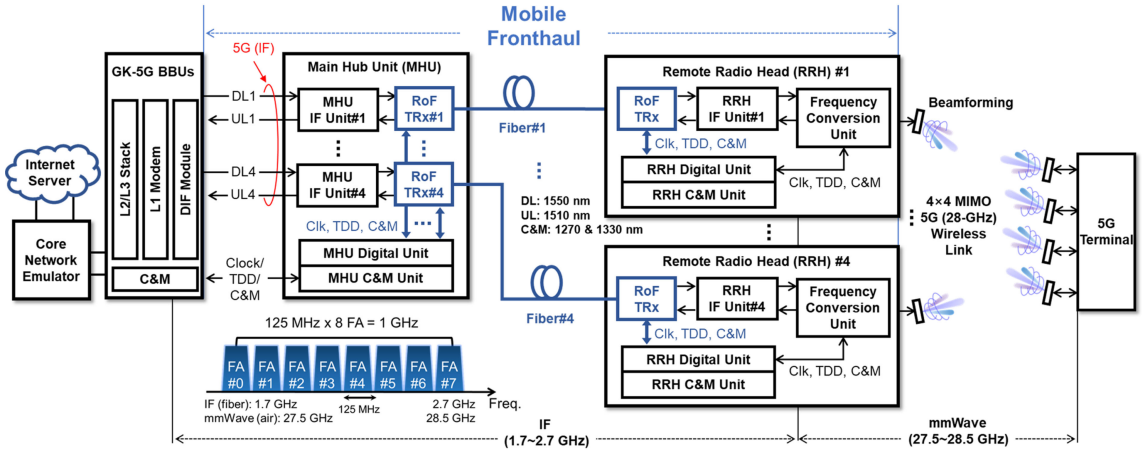

Figure 2.1: Configuration of IFoF-based mobile fronthaul with developed 5G base station.[32]

able insights into the capabilities and limitations of RoF implementations within these frequency bands, thereby contributing to the advancement of wireless communication technologies.

The study presented in [32] focuses on IFoF technology for 28 GHz RAN in the context of 5G. An innovative 5G trial service employing the developed IFoF-based distributed antenna system, supporting a 4×4 MIMO configuration, is illustrated in Figure 2.1. System theoretical throughputs of 2.5 Gbit s^{-1} for downlink and 10 Gbit s^{-1} with MIMO for uplink transmissions were presumed.

The 5G base station platform interfaced with an internet server via a core network emulator, handling a total 5G signal bandwidth of 1 GHz and an IF band ranging from 1.7 GHz to 2.7 GHz. From the BBUs, four electrical 5G signals in the IF band were transmitted to the multi-homing unit for each IF unit, utilizing 1 km of SMF and an optical power of 6 dBm. The system also included a 100 MHz clock, time division duplexing (TDD) sync signal, and control & management (C&M) signal from the BBUs, carrying control information for beamforming at the RRH's antenna. The detected electrical 5G IF signal was then frequency up-converted to the 28 GHz in mmW band for wireless transmission through an array antenna. Implementing a 4×4 MIMO configuration due to four wireless links (four Tx and four Rx antennas), beamforming achieved a gain of 18 dB at the RRH using 64 element antennas (8×8).

Phase noise characteristics (Figure 2.2a) were assessed by measuring the single-sideband (SSB) phase noise of the mmW carrier signal at 25.7 GHz, achieving phase noise levels of -70 dB Hz^{-1} at 1 kHz and -95 dB Hz^{-1} at 100 kHz at the RRH.

In Figure 2.2b, the transmission performances of four RoF links in a 5G signal were investigated. After wireless transmission over 2 m, the EVM of the 28 GHz 5G signal

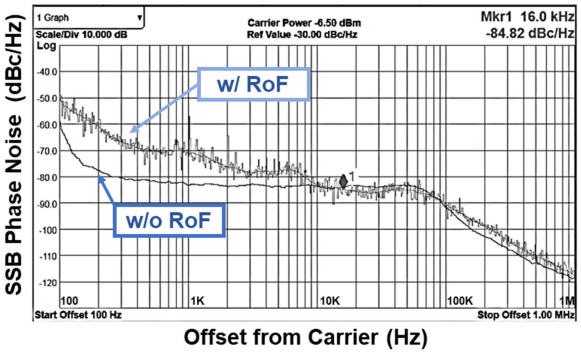

(a) Phase noise of upconverted RoF

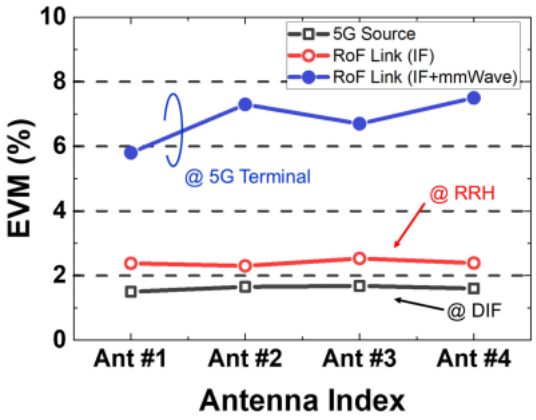

(b) EVM performance of 5G source, IF output and upconverted RF

Figure 2.2: Performance of proposed IFoF configuration. [32]

was measured at the 5G terminal. The EVM degradation was within 5.6 %, slightly larger than the RoF link performance degradation due to signal amplification for high output power (>200 mW) and frequency up-down conversions at the antenna. The EVM remained below 8 %, meeting the limit for 5G with 64-QAM as specified in [33].

Four RRHs were set up outdoors as independent cells, linked to the 5G BBU pool via RoF connections. While moving the 5G terminal at speeds up to 60 km h^{-1}, downlink throughput was measured in real-time, achieving a maximum data rate of 5.125 Gbit s^{-1} and maintaining 5 Gbit s^{-1} downlink throughput with seamless cell-to-cell handover. In a static scenario, the peak data rate for downlink transmission reached 9.042 Gbit s^{-1}.

In the study conducted by [34], a mmW based 5G MIMO indoor network is explored. The presented setup employs IFoF, with an IF of 2 GHz and mmW at 28 GHz, utilizing a signal bandwidth of 100 MHz. They characterized the IFoF transmission link, which has a cascade structure, by measuring its EVM level to be 5 % or less, with total optical link losses of 10.2 dB for the first and 13.5 dB for the split second RRH. The distance between RRHs was 2 km of SMF, and the wireless distance was fixed at 2 m. Additionally, the study investigates the use of an avalanche photodiode (APD) to further enhance the optical power budget.

For all cases, the Downlink (DL) throughput varied from 700 Mbit s^{-1} to 950 Mbit s^{-1}, with an average value of approximately 830 Mbit s^{-1}. Similarly, the Uplink (UL) throughput ranged from 100 Mbit s^{-1} to 140 Mbit s^{-1} over time, with an average value of about 120 Mbit s^{-1}. The observed difference in throughput between DL and UL is attributed to the TDD ratio.

The bandwidth of the utilized APD was approximately 3.3 GHz, which induced extra penalties to the higher frequency channels (i.e., 3.6 GHz to 4.4 GHz). Therefore, com-

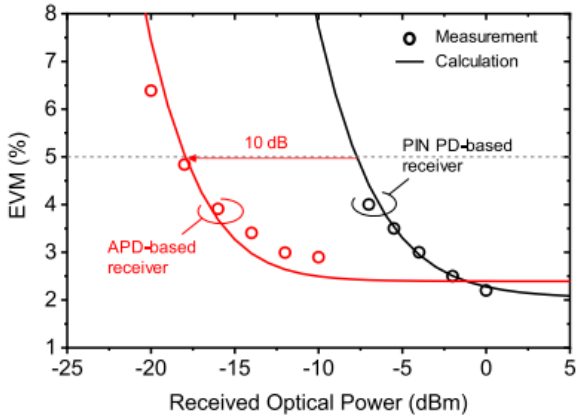

Figure 2.3: EVM as function of input power for two different photodiodes (APD vs. PIN).[34]

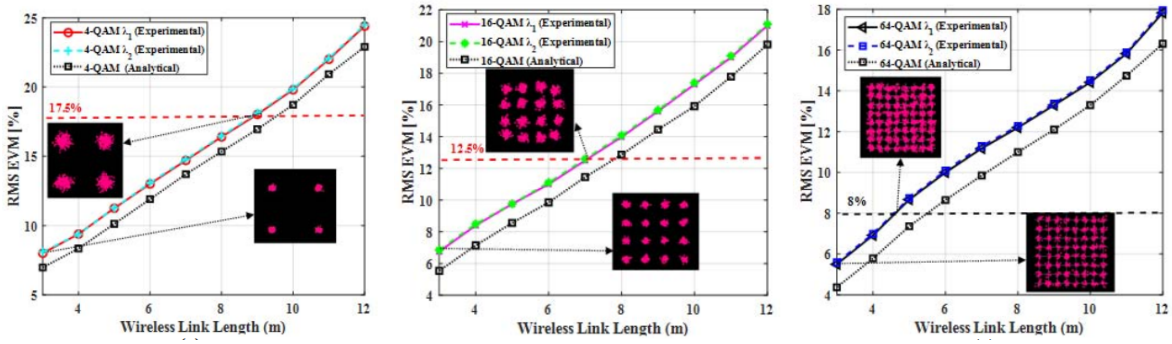

(a) QPSK (b) 16-QAM (c) 64-QAM

Figure 2.4: Measured RMS EVM versus wireless link length at λ_1 and λ_2 for WDM-RoF. [35]

parisons were performed at relatively low frequencies, such as 2 GHz, to evaluate the relative power budget improvement provided by the APD. The APD, offering avalanche gain to the electrical signal, achieved an additional optical link budget of 10 dB as shown in Figure 2.3.

In their recent publication [35], advancements in RoF-based fronthaul for 5G mobile networks are detailed. They notably demonstrate the spectral efficiency of the M-QAM technique within a WDM hybrid wireless RoF network. This is achieved using a DML at a symbol rate of 250 MBaud across two optical wavelengths. The WDM setup incorporates an arrayed waveguide grating for path configuration to outputs and dynamic resource allocation for data transmission. An instance of their approach includes modulating an RF signal to a DML in response to a low traffic demand on a RRH, utilizing time-division multiplexing.

Figure 2.4 in their study illustrates the measured RMS EVM across different lengths of wireless links for 4-QAM, 16-QAM, and 64-QAM at wavelengths λ_1 and λ_2. These measurements are for hybrid fiber-wireless WDM-RoF at data rates of 0.5 Gbit s^{-1}, 1 Gbit s^{-1}

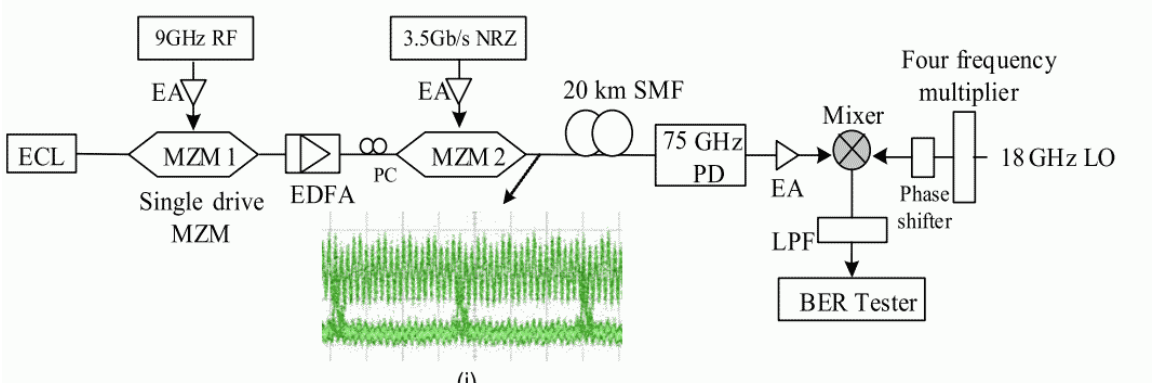

Figure 2.5: Experimental setup for RoF system based on 8x frequency multiplication optical mmW generation.[37]

and 1.5 Gbit s^{-1}, aligning with the 3GPP standards for 5G [33]. However, the article does not specify the RF frequencies utilized in these experiments.

In publication [36], an experimental demonstration of a K-band (18 GHz to 27 GHz) fiber-wireless integration transmission system is presented. The system is capable of transmitting up to 4 GBaud (32 Gbit s^{-1}) polarization division multiplexing (PDM)-16-QAM RF signal at 23 GHz. This signal can be transmitted over 100 km SMF and further extended over a >1 km long wireless RF link with a 2×2 MIMO setup, achieving a BER below the hard decision-forward error correction threshold of 3.8×10^{-3}. The setup incorporates an optical In-phase/Quadrature (I/Q) modulator with a 32 GHz 3 dB optical bandwidth and utilizes coherent optical detection for signal processing.

2.2 RoF in FR2-2 band

In this section, we provide a summary of research efforts that have explored transmissions within the FR2-2 band.

In [38], a large-capacity, high-spectral-efficiency fiber-wireless integration system within the V-band (50 GHz to 75 GHz) is experimentally demonstrated. The system supports up to a 10 GBaud (120 Gbit s^{-1}) PDM-64-QAM mmW signal at 57.2 GHz. This 10 GBaud, 57.2 GHz PDM-64-QAM vector millimeter-wave signal can be transmitted over a 60 km SMF and a 1 m wireless RF link while maintaining a BER below the soft decision-forward error correction threshold. The generation of a 57.2 GHz PDM-64-QAM wireless mmW signal is achieved through heterodyne beating of two free-running external cavity lasers, followed by transmission over a 2×2 MIMO wireless RF link. An optical I/Q modulator, with a 32 GHz 3 dB optical bandwidth, is utilized for optical 64-QAM modulation. The study illustrates that a 10 GBaud, 57.2 GHz PDM-64-QAM vector millimeter-wave signal can be generated with a BER under the hard decision-forward error correction threshold

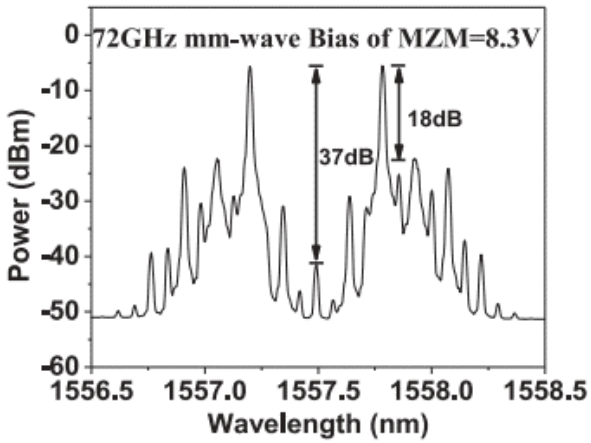

Figure 2.6: Output optical spectrums of the single-drive MZM. [37]

of 3.8×10^{-3}. The downside is that heterodyne mixing requires a large setup complexity, but it has inherited immunity to CD.

In the study by [37], an experiment with eight times frequency multiplication using a MZM achieved an output frequency of 72 GHz (the setup is depicted in Figure 2.5). By carefully selecting the excitation signal and setting the DC bias point for optimal eight times multiplication and double sideband-suppressed carrier (DSB-SC), the process was accomplished without optical filtering; the suppression of unwanted components was controlled through bias settings. Deviations from theoretical bias calculations necessitated experimental adjustments, resulting in 18 dB suppression of residual harmonics, as shown in Figure 2.6. Due to significant attenuation in MZM1, which is set to its minimum bias for DSB-SC generation, an EDFA was necessitated between MZM1 and MZM2. The latter is data modulator.

The transmission utilized a non-return-to-zero on-off keying (NRZ OOK) signal at a bitrate of 3.5 Gbit s^{-1}. While effective for demonstration purposes, On-Off Keying is not suitable for radio transmissions due to its broad and spectrally inefficient nature [39]. This experiment was conducted over 20 km of SMF, achieving a BER of 10×10^{-9}.

In the study presented by [40], the design and simulation demonstrate the transmission of a quadrature phase shift keying (QPSK) signal utilizing optical stacking and mixing. The paper introduces an innovative approach for generating a QPSK vector mmW signal at odd multiples of the RF signal, employing a phase modulator and a wavelength selective switch. Notably, phase precoding at the transmitter is deemed unnecessary for QPSK RF vector signal generation. The transmission was simulated over a 20 km SMF.

The transmission signal achieved a rate of 4 Gbit s^{-1}, with a simulated BER of 10×10^{-6}. Output signals at frequencies of 30 GHz, 50 GHz and 70 GHz were simulated. Given the requirement for precoding for the input signal with notable amplitude modulation, the proposed scheme is not deemed suitable for high-order quadrature amplitude modulation

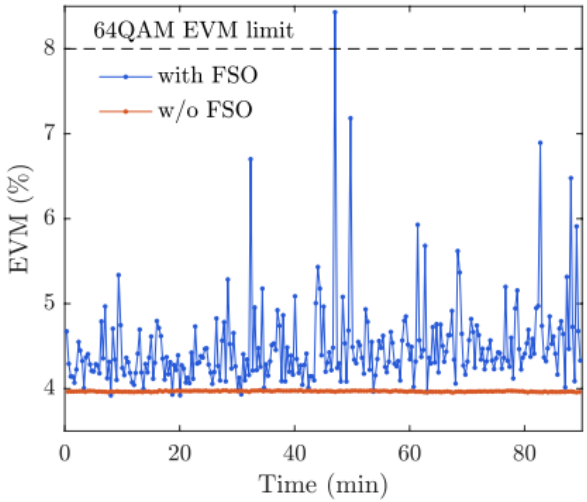

Figure 2.7: Measured EVM versus time for the 64-QAM, 100 MHz 5G signal.[41]

(QAM) and orthogonal frequency-division multiplexing (OFDM) modulation transmissions.

2.3 RoFSO and the combination of RoFSO and RoF experiments

Lastly, this section presents a overview of research studies focused on RoFSO or the integration of RoFSO with RoF.

In the study presented by [41], an integrated testbed is utilized to demonstrate the transport of 100 MHz LTE and 5G DL signals using low-latency and bandwidth-efficient A-RoF across an 8 km SMF. This system facilitates the simultaneous operation within the same fronthaul infrastructure and incorporates a hybrid fiber-wireless scenario, which includes a FSO fronthaul extension of 55 m.

The LTE networks in question are set up to function with a 5 MHz bandwidth, achieving maximum throughputs of 8 Mbit s^{-1} for UL and 16 Mbit s^{-1} for DL. The 5G signal is a 100 MHz bandwidth 64-QAM signal operating in the 3.5 GHz band (FR1 band). It is crucial to note that in this study A-RoF technology is exclusively used for 5G transmission, whereas LTE transmission employs D-RoF.

CWDM technology is leveraged to ensure the seamless coexistence of these radio systems over a single optical link. The primary evaluation criterion was the time variation of the EVM. The minimal FSO loss was recorded to be approximately 2.5 dB, with fluctuations to about 2 dB due to turbulence effects.

To assess the resilience of the 5G service against power fluctuations in the FSO link, EVM measurements taken over a duration of 1.5 h are presented in Figure 2.7. In the

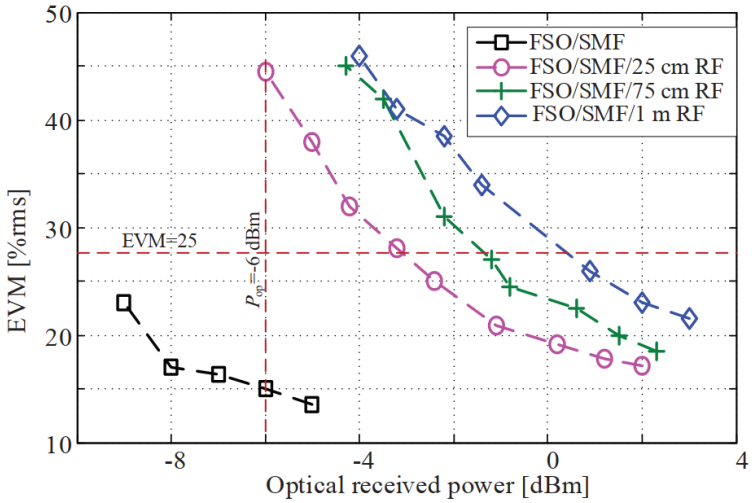

Figure 2.8: Performance of the 5G signal transmission in terms of EVM vs. optical received power for different lengths of the RF wireless link.[42]

absence of FSO, the system exhibited a stable EVM performance of 3.9 %. With the FSO extension in use, significant variations in the measured EVM were observed over time. Nevertheless, the EVM remained below 5 % in most cases, exceeding the specified limit of 8 % for a 64-QAM signal as outlined in [33].

In the study, [42] explores the utilization of a frequency comb source for generating WDM. The study encompasses the use of SMF, FSO, and RF wireless links, specifically focusing on a RF wireless link operating at a carrier frequency of 28 GHz.

This research delves into the distribution and transmission of 5G signals over hybrid optical/wireless links. A comb source, constructed using a single laser diode, generates five subcarriers. Each subcarrier serves as a carrier for a distinct 5G signal. A 8 Gbit s^{-1} QPSK data signal is modulated onto each subcarrier and transmitted across three different transmission mediums. The signals traverse a 10 km SMF and a 6.5 m FSO channel. The wireless channel employs two horn antennas operating within the 26 GHz to 40 GHz band, boasting a gain of 25 dBi.

Figure 2.8 presents the performance of the 5G signal, specifically in terms of EVM, as it is transmitted over SMF/FSO links and across three wireless distances. It is noted, however, that the signal used does not align with the 3GPP standards for 5G [33] because they used plain QPSK, not modulated on subcarriers of OFDM.

In the study by [43], the focus is on a pure FSO link and its susceptibility to environmental factors, specifically the impact of dust on transmission. The research encompasses an all-optical FSO link transporting a 16 Gbit s^{-1} 16-QAM 5G signal across the frequency range of 21 GHz to 29 GHz. The length of the FSO link extended to 2.7 m.

In [44], the study explores the performance of Radio over RoFSO links under the influence of atmospheric fading caused by fog and turbulence. The research utilizes signals

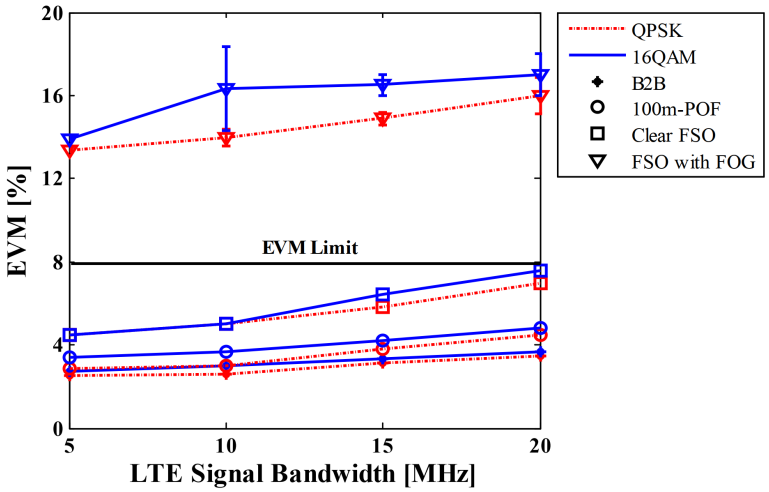

Figure 2.9: Performance of the 5G signal transmission in terms of EVM vs. optical received power for different lengths of the RF wireless link.[42]

at 800 MHz across bandwidths of 5 MHz, 10 MHz, 15 MHz and 20 MHz, with the FSO beam traversing an 11 m long free space channel. To simulate turbulence within an indoor atmospheric chamber, hot air is injected, and temperature measurements are taken at 10 points along the chamber. The resulting measured value of σ_R^2 is 1.7, indicating a regime of moderate turbulence. Their measured results of EVM are shown in Figure 2.9 The findings suggest a need for expanded testing of turbulence effects on mmW bands.

Chapter 3

Objectives of the Thesis

Novel system design for RoF and RoFSO systems and their combinations for seamless mmW transmission in advanced mobile networks.

- Advancement towards utilizing Frequency Range2-1 (FR2-1) bands (24 250 MHz to 52 600 MHz) in 5G NR networks, aiming for FR2-2 bands (52 600 MHz to 71 000 MHz).
- Tests of system configurations to simplify the RF parts of the system and using different optical approaches to optimize overall performance.
- The employment of FSO to the analog mmW networks as an alternative to fiber connection with the determination of the influence of atmospheric turbulence on the transmitted signal.

Chapter 4

Achieved results

4.1 Optically phased antenna array

To augment the throughput in fifth-generation data networks, expanding the frequency bandwidth utilized is essential. However, in frequencies below 6 GHz, constraints are imposed by national regulatory bodies and the necessity to share the spectrum with other services. As a result, migration to millimeter-wave bands is underway, particularly in Europe to the n258 (24.25 GHz to 27.5 GHz) and n259 (39.5 GHz to 43.5 GHz) frequency bands. Although these bands offer substantial bandwidth, they also introduce significant free-space attenuation during transmission. This challenge necessitates the use of high-gain antennas, which, due to their narrow beam widths, require precise beam steering. Both high gain and beam steering functionalities can be effectively achieved using phased array antennas. A significant advantage of using antenna arrays is the feasibility of equipping each antenna element with its dedicated power amplifier for transmission and a low-noise amplifier for reception. This configuration yields a substantial increase in the overall transmit power output. Additionally, it enhances the reliability of the entire system. In a larger antenna array, the failure of a single element has a negligible impact on the system's performance, thereby ensuring more robust and consistent operation.

A phased array antenna comprises a series of elementary antennas and a feed network. This network is responsible for providing the necessary phase shifts and signal amplitudes to each antenna element. The configuration of the antenna array feed network may also incorporate components such as power amplifiers and low noise amplifiers. Importantly, the implementation of this feed network is not restricted to the electrical domain; it can also be realized optically.

In the subsequent sections, two optical domain approaches for phasing an antenna array will be presented. The first approach utilizes optical True Time Delays (TTD), while the second employs varying time delays for different wavelengths, achieved through

CD in optical fibers.

4.1.1 Introduction

The radiation pattern of the antenna array is expressed by equation:

$$F(\theta,\phi) = f(\theta,\phi)\sum_{n=1}^{N} a_n \exp(j\varphi_n) \times \exp[jk(n-1)d\sin\theta] \tag{4.1}$$

where $f(\theta,\phi)$ is the radiation pattern of single element antenna, a_n is excitation amplitude, φ_n is excitation phase, d is distance between element antenna, $k = 2\pi/\lambda$ is wave number in free space and λ is wavelength in free space.[45]

Assume that the observation point is far from array, so that phases from all element antenna are identical at direction $\theta = \theta_0$, excitation phase of the nth element antenna φ_n is:

$$\varphi_n = -nu_0 \tag{4.2}$$

$$u_0 = kd\sin\theta_0 \tag{4.3}$$

The equations 4.2 and 4.3 are used to calculate the required signal phases at the antenna elements for peak radiation in a given direction θ_0. In this case, the radiation pattern of an antenna array is expressed by

$$F(u) = f(\theta,\phi)\sum_{n=1}^{N} a_n \exp(jnu) \tag{4.4}$$

u is used instead of θ

$$u = kd(\sin\theta - \sin\theta_0) \tag{4.5}$$

with this we use only u for determination of radiation pattern.

To find the desired time delays, we modify the equations 4.2 and 4.3 to

$$\Delta t = \frac{nkd\sin\theta_0}{2\pi} \tag{4.6}$$

4.1.2 Optical beamforming based on variable delay lines

In this experiment, we investigated beamforming using developed a three-element linear antenna array using Variable Optical Delay Liness (VDLs) capable of adjusting the delay between 0 ps to 130 ps. The antenna array, designed for the 24 GHz to 28 GHz band, comprises planar dipole antennas modeled using CST Studio Suite. Figure 4.1 showcases

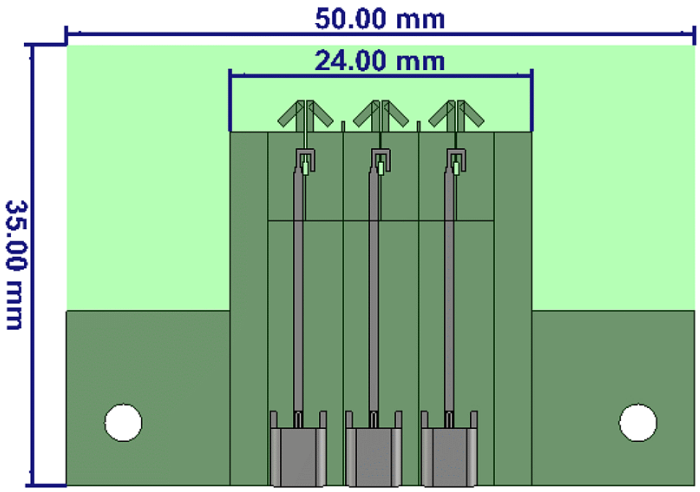

Figure 4.1: Phased antenna array.[46]

a model of these antennas. They were fabricated on Isola Astra MT77 substrate, with a thickness of 254 µm and a relative permittivity ϵ_r of 3. Each antenna element offers a gain of 5 dBi and operates within a bandwidth of 23.5 GHz to 39.5 GHz. The narrower bandwidth of the entire array results from the spacing between the elements. Spacing between the elements is $d = 6$ mm.

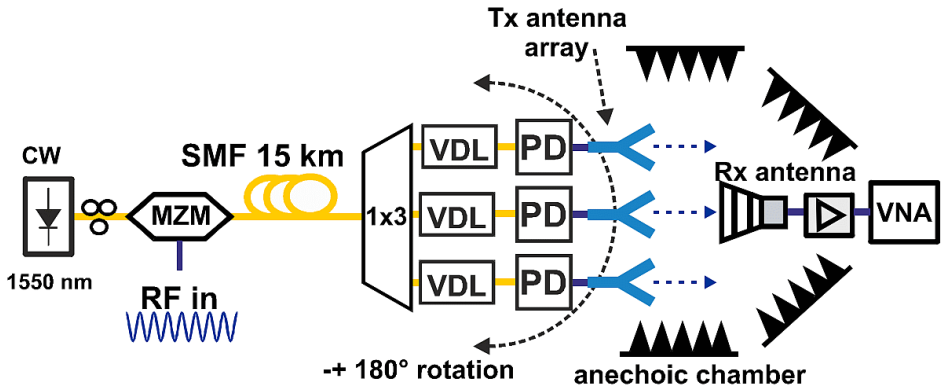

Figure 4.2: Optical beamforming setup.[46]

Figure 4.2 illustrates the complete measurement setup. The transmitting section includes a continuous wave (CW) laser (ID Photonic CoBrite-DX4) operating at a wavelength of 1550 nm and an optical power of 16 dBm. This is followed by a polarization controller and a MZM (Fujitsu FTM7938EX/201) biased at the quadrature point. A signal from a Vector Network Analyzer (VNA, R&S ZVA67) is feed into the MZM.

The modulator's output feeds into a 15 km long SMF, simulating the optical infrastructure leading to a transmit antenna array. On the antenna side, the optical signal is divided for the array elements using a 1:3 optical power splitter. Each branch includes a VDL to provide the required time-delayed signal for each antenna element. Following

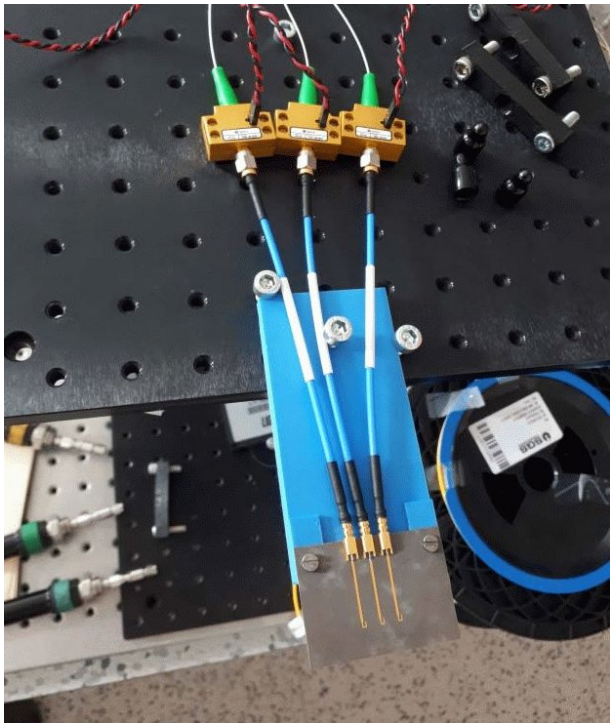

Figure 4.3: Antenna terminal in optical TTD beamforming.[46]

the VDLs are optical detection diodes (PD, Optilab - PD40) that convert the signal back to the electrical domain. The optical detectors are connected to an antenna array via 100 mm long phase-matched coaxial cables.

The receiving part of the setup is shown in the Figure 4.3. Radiation patterns of the antenna array were measured in an anechoic chamber using a VNA with a DRH40 horn antenna, positioned in far-field 3 m away, as the receiver.

Radiation diagrams were acquired at 26 GHz for three steered beams at angles of 0° and ±22.5°. A beam steering of ±22.5° corresponds to a phase difference of 80° between the antenna array elements, necessitating a VDL setting to 7.7 ps for the delay.

Figure 4.4 compares the simulated and measured radiation patterns of the antenna array for beam steer of 0° and ±22.5°. There is a broad concordance between the simulations and measurements, with lesser agreement in back radiation for angles greater than 90°, attributable to the absence of coaxial cables and optical detectors in the simulation model.

4.1.3 Optical beamforming based on chromatic dispersion of optical fiber

In the next stage, I designed and demonstrate a RoF link featuring an antenna array with beam steering capabilities. The system's parameters were rigorously verified, and we successfully showcased the ability to optically steer the antenna beam. Furthermore, the

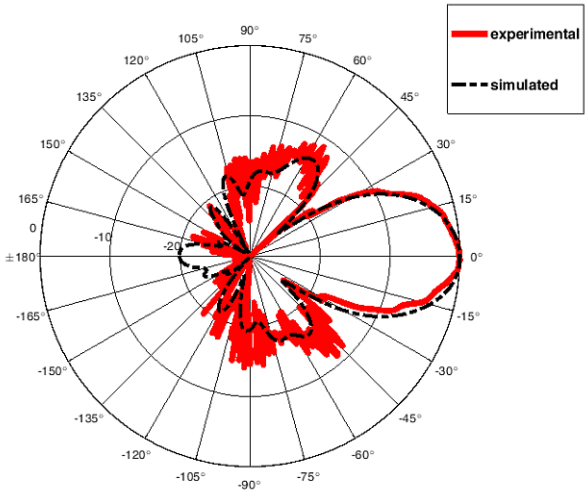

(a) Beam steer of 0°

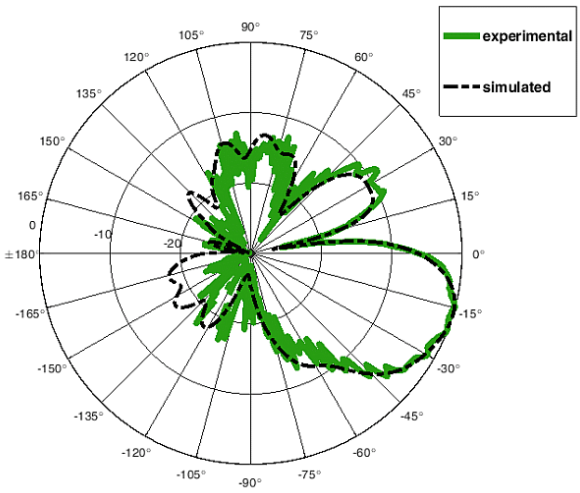

(b) Beam steer of $-22.5°$

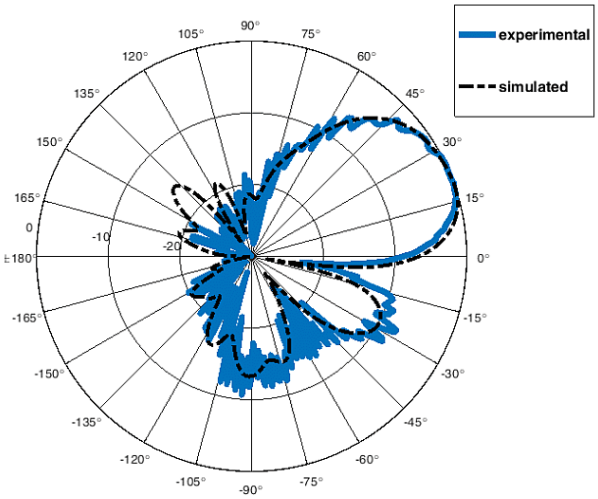

(c) Beam steer of 22.5°

Figure 4.4: Phased antenna array measurements.[46]

system's functionality was validated through LTE data transmission using a test model 3.1 with 64-QAM and 20 MHz bandwidth signal. To the best of our knowledge, this represents the first instance of experimental verification involving data transmission in such a setup.

For the purpose of verification of optically steered antenna beam, we utilized the same three-element antenna array (as shown in Figure 4.1) that was employed in the beamforming experiment using VDL (as detailed in Section 4.1.2).

The experiment focused on achieving a beam steering angle of $\theta_0 = 25°$, with the necessary signal delays calculated for a signal frequency of 25 GHz. For this degree of beam rotation, a phase shift of $\varphi_n = 80°$ is required between the antenna elements. This corresponds to delays of $t_1 = 0$ ps, $t_2 = 8.45$ ps, and $t_3 = 16.9$ ps for each antenna element, respectively.

To achieve such precise delays between elements, lasers with tunable wavelengths are employed. The required difference in wavelengths between the lasers is given by the following modified equation from [47]:

$$\Delta\lambda = \frac{\varphi_n}{LDf_{RF}} \tag{4.7}$$

where φ_n is desired phase shift in rad, L is the length of SMF used, D is the CD coefficient and f_{RF} is RF carrier frequency.

n	φ	λ_{1550}	$\lambda_{1534.5}$	λ_{1571}
1	0°	1550.000 nm	1534.500 nm	1571.000 nm
2	80°	1550.318 nm	1534.841 nm	1571.291 nm
3	160°	1550.636 nm	1535.183 nm	1571.583 nm

Table 4.1: Ideal beam forming parameters.

Table 4.1 presents ideal sample wavelength values for individual lasers, calculated for a beam steering angle of 25°. These calculations were based on an $f_{\mathrm{RF}} = 25$ GHz and an SMF length of 10.2 km. The CD values for the SMF (G.652 type) at wavelengths of 1534.5 nm, 1550.0 nm and 1571.0 nm are 16.019 ps nm^{-1} km^{-1}, 17.205 ps nm^{-1} km^{-1} and 18.763 ps nm^{-1} km^{-1}, respectively. The selection of these wavelengths aligns with the standards set by the Coarse Wavelength Division Multiplexing (CWDM), enabling the usage of a CWDM multiplexer. This component merges signals from the laser source and subsequently separates the modulated signals at the receiver end.

However, using lasers with wavelengths this as close as in Table 4.1 to each other is impractical, as it would hinder their separation in the system. Therefore, greater separation between laser wavelengths was necessary, so we used CWDM grid wavelengths to utilize CWDM multiplexer. The wavelengths ultimately used in the circuit were approximately

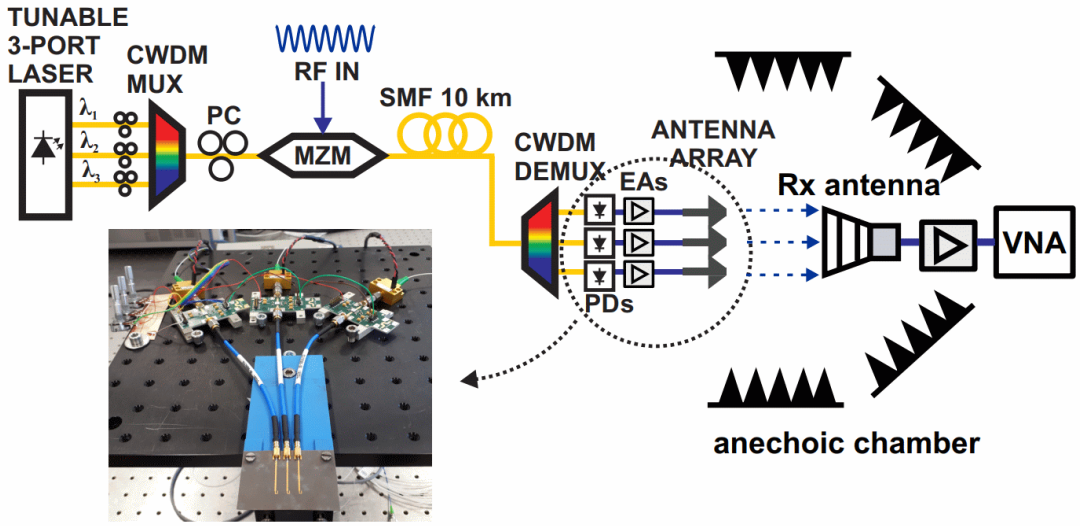

Figure 4.5: Optical beamforming setup useing CD.[48]

1534.5 nm, 1550.0 nm and 1571.0 nm, with fine-tuning accomplished by connecting the detection diodes to the VNA. Precise wavelength adjustments were made to 1534.695 nm, 1550.031 nm and 1571.178 nm using the VNA (R&S ZVA67), which also compensated for varying fiber lengths from the CWDM divider. The combined effect of these two factors restricted the beamforming bandwidth for a single steering setting to around 500 MHz bandwidth.

Figure 4.5 illustrates the complete experimental setup. A 3-port CW laser (ID Photonic CoBrite-DX4), with adjustable wavelength outputs, was employed. The output power of all lasers was set to 16 dBm. A CWDM multiplexer, connected via polarization controllers, aggregated all optical signals. This was followed by another polarization controller and a MZM (Optilab IML-1550-50-PM), biased at the quadrature point with a voltage of 0.8 V. The RF signal from the VNA or modulator was input into the MZM, ensuring that all optical carriers were modulated with the same signal.

Subsequently, a 10.2 km SMF, simulating the optical infrastructure, provided the necessary CD for adequate phase shift between each optical subcarrier. Longer SMF lengths are not advisable due to potential frequency-selective power dips in the RF signal.

On the receiver side, the SMF signal was divided into three paths using CWDM, based on their wavelengths, and fed directly to the detection diodes (Optilab PD40), converting the signal back to the electrical domain. These were followed by three identical medium power amplifiers (Analog Devices HMC1131) with a gain of 22 dB and a P1dB of 23 dBm. The amplified signals were then fed to the elements of the antenna array.

Radiation pattern and data transmission measurements were conducted in an anechoic chamber. Radiation pattern measurements utilized a VNA (R&S ZVA40), a DRH40 measurement antenna, and a Miteq AMF-4F-260400-40-10p low noise amplifier. Data

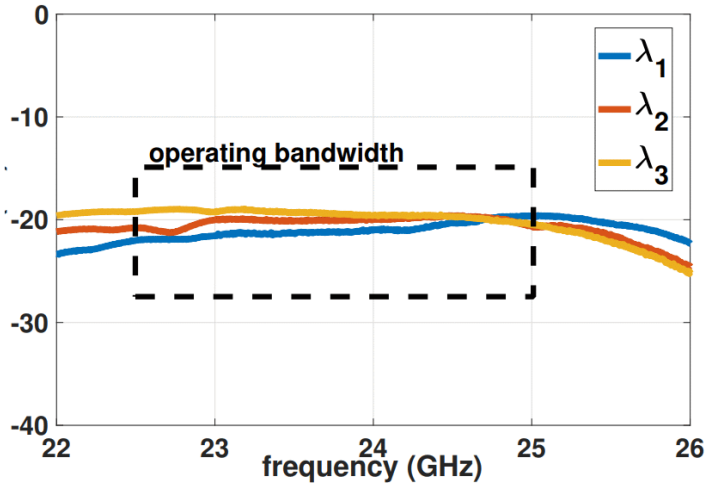

Figure 4.6: S_{21} for each antenna array element.[48]

transmission measurements were performed with a signal analyzer R&S FSW26, and the signal was generated at baseband using a vector signal generator R&S SMW200A, then mixed into the 25 GHz band.

Upon setting the system to the desired phase shifts through wavelength adjustments of the lasers, the transmission characteristics (S_{21}) in the 22 GHz to 26 GHz band were measured. Figure 4.6 illustrates these characteristics, showing that each branch's transmission profile remains flat, with variations within 1 dB.

Subsequently, the steering of the radiation pattern was verified in an anechoic chamber, using measurements from the VNA and the NSI-MI system. The transmitting side of system, placed on a turntable, was positioned 3 m away for radiation pattern measurements at 24 GHz, 26 GHz and 28 GHz over azimuths of ±180°. Antenna beams steering were verified at angles of 0°, and ±25°. There was good agreement with the CST Studio Suite simulation for the 26 GHz frequency.

LTE data signal transmission was then verified using the E-TM 3.1 test model with a 20 MHz bandwidth. This model is utilized for measuring the total power dynamic range, which maximizes the difference between the maximum and minimum power of an OFDM symbol, employing 64-QAM modulation [49]. The measurement was performed at 25 GHz, with the Local Oscillator of the modulator (R&S SMF100A) set to this frequency. We reduced the distance to 1.5 m and conducted measurements across azimuths of ±60°. We performed tests for two antenna beam steers: 0° and 25°.

According to TS 36.141 [49], the EVM limit for 64-QAM must be within 9 %. As shown in Figure 4.7, this limit is achieved over a relatively wide azimuth range of approximately 80°. Defining beamwidth as a −3 dB decrease, the beamwidth is 25° for an unsteered beam and 40° beamwidth for a 25° steered beam. The minimum measured EVM for both settings is 5.6 %. The maximum received power is −38.5 dBm for the unsteered beam and

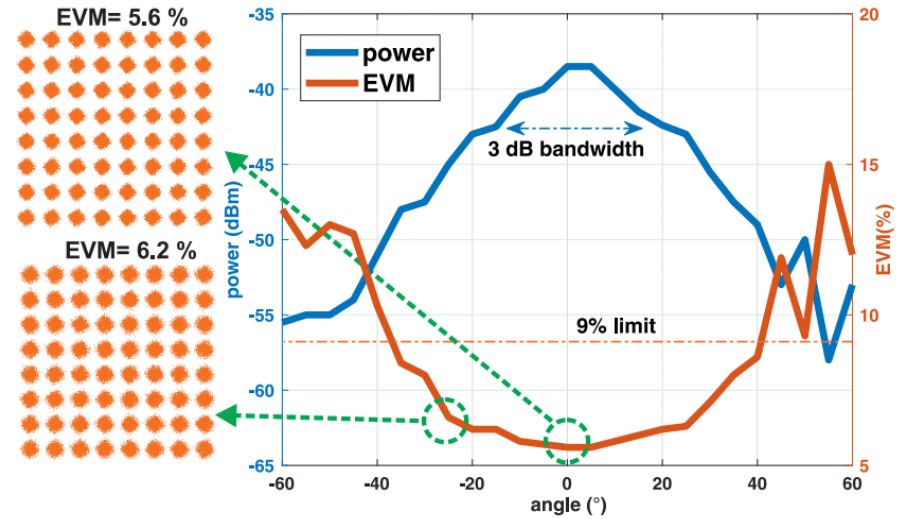

(a) Beam steer of 0°

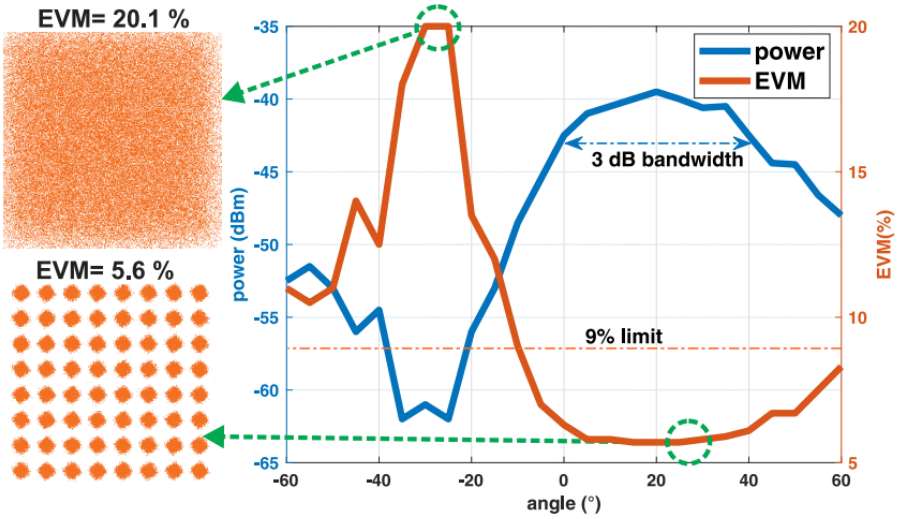

(b) Beam steer of 25°

Figure 4.7: EVM and received power of antenna array.[48]

−40.0 dBm for the steered beam. This difference is due to the radiation characteristics of the individual elements of the antenna array, see equation 4.1, where the radiation pattern of one element is multiplied by the antenna array factor. Thus, a decrease in gain in a particular direction of an antenna element will be manifested as a decrease in gain of the entire antenna array. The constellation diagram of the test signal is also depicted in the Figure 4.7.

Further analysis examined the EVM of the modulated signal relative to LTE signal bandwidth. Using E-TM 3.1 with different bandwidths, namely 1.4 MHz, 3 MHz, 5 MHz, 10 MHz, 15 MHz and 20 MHz, were generated. This confirmed that the antenna radiation beam does not deviate for various bandwidth-modulated signal frequencies. The minimum EVM was 5.1 % for 1.4 MHz and 5.7 % for 20 MHz, a difference caused by varying SNR

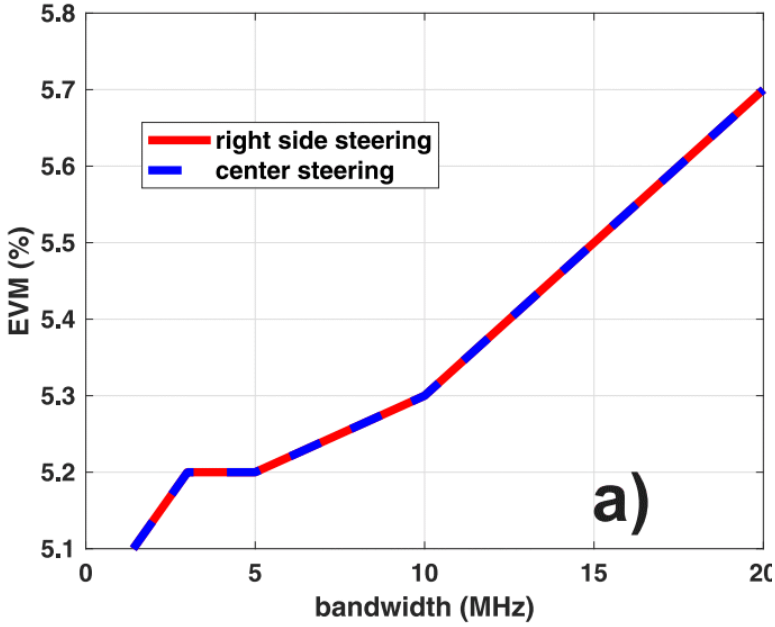

Figure 4.8: Measured EVM vs. OFDM bandwidth.[48]

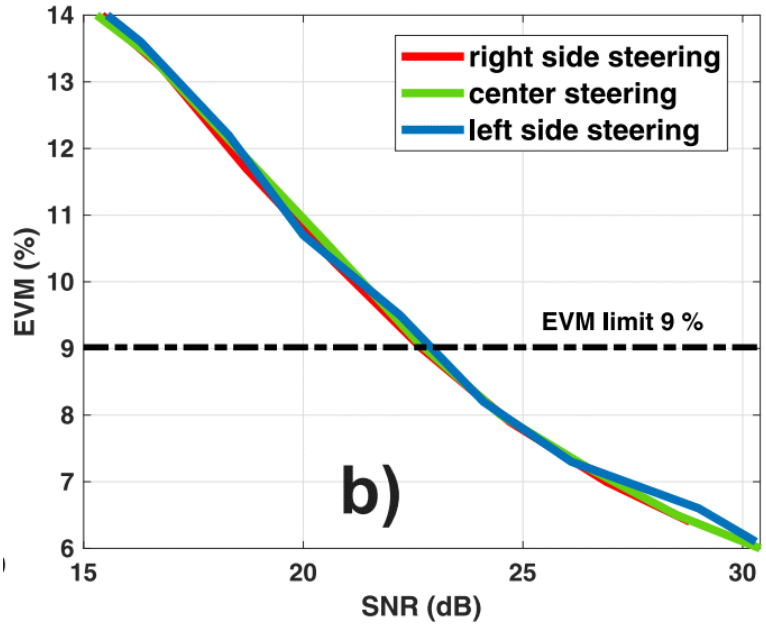

Figure 4.9: Measured EVM vs. received SNR.[48]

levels due to integrated system background noise of −146 dBm/Hz. Figure 4.8 provides a detailed view of this characteristic.

Finally, the system's robustness to optical path attenuation was analyzed. Figure 4.9 plots the EVM's dependency on output SNR. The SNR was adjusted using an optical attenuator (DA-100-SC-1300/1550-9/125-S-40), inserted before the CWDM in the receiving section. Optical attenuation ranged from 0 dB to 9 dB, ideally translating to a double RF attenuation of 0 dB to 18 dB. This added attenuation shows that the system still

offers a sufficient margin for additional loss in the optical component, for instance, in FSO applications.

4.1.4 Discussion

In Chapter 4.1.2, we introduced and successfully tested a system designed for beam steering in a three-element antenna array for RoF at 25 GHz band. The findings from these tests have been documented in [46]. This system demonstrated the capability to steer the radiation beam with a precision of one degree.

The design of the system allows for easy scalability to larger linear arrays or even planar antenna arrays. The primary requirement for scaling up is the incorporation of a larger optical power divider and a proportional increase in the number of optical detection diodes. However, when expanding the system, it is crucial to consider the power budget, especially since any losses incurred in the optical domain effectively double in the electrical domain. To mitigate this issue, an EDFA can be employed to compensate for the loss.

Chapter 4.1.3 introduces the concept of steering the beam of an antenna array using CD, with the experimental findings published in [48]. This system offers a significant advantage over the approach detailed in 4.1.2 due to its simple electronic control mechanism, which adjusts the beam by altering the laser's wavelength. Unlike previously published papers, this experiment includes a test on a real data signal, achieving a maximum bit rate of 75 $\mathrm{Mbit\,s^{-1}}$ for 64-Quadrature Amplitude Modulation (QAM) OFDM.

We propose a modification to this concept, suggesting the use of Dense Wavelength Division Multiplexing (DWDM) in place of CWDM. DWDM offers optical channel spacings as narrow as 0.8 nm (corresponding to a 100 GHz step), enabling the tuning of laser wavelengths closer together. This would potentially increase the usable bandwidth of the resulting delay set for each antenna array element.

Furthermore, incorporating an EDFA at the transmitting section, before the DWDM divider, could amplify the signal post optical section. This enhancement is likely to improve the resulting EVM of the signal. Additionally, DWDM could function as a bandpass filter, mitigating unwanted broadband noise, similar to the approach in [50]. This concept opens avenues for further research and development.

4.2 Direct modulated laser for fifth generation systems

In this chapter, we present a novel proof of concept targeting the 5G systems of RoF systems. Our approach utilized a DML to transmit five aggregated 20 MHz OFDM mod-

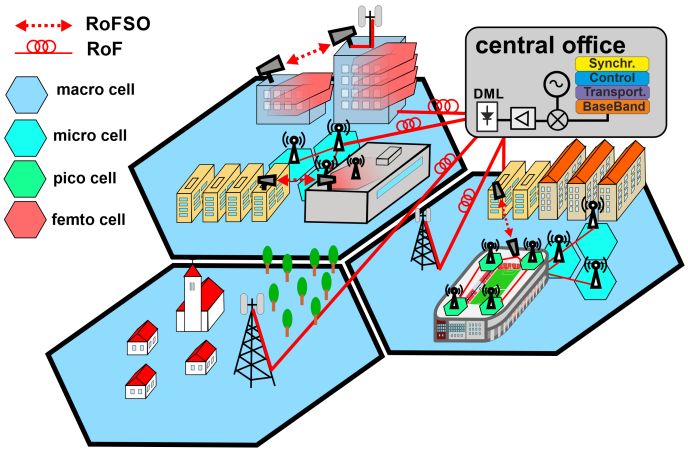

Figure 4.10: RoF and RoFSO deployment for connection of micro-, pico-, and femto-cells in 5G architecture. [51]

ulated signals. These signals collectively spanned a bandwidth of 100 MHz, with each subcarrier being modulated using 64-QAM. A key aspect of our investigation focused on the coupling behavior when interfaced with SMF, FSO, and wireless link like in Figure 4.10.

The primary motivation for this study stemmed from the need to explore simpler and more cost-effective alternatives to externally modulated lasers (EML), which, despite offering superior transmission parameters, are more complex and expensive, particularly for large-scale implementations. At the inception of our experiment, to the best of our knowledge, there had been no prior experiments integrating DML with SMF and FSO in this context.

The core challenge of this experiment was the optimization of a DML for operation in the 5G frequency range, specifically targeting frequencies between 20 GHz to 30 GHz as per [52]. The experimental setup was conducted in the 24 GHz to 26 GHz band. This arrangement enabled the transmission of five OFDM signals, potentially achieving transmission speeds of up to 1 Gbit s^{-1} within a 100 MHz frequency band. Additionally, we examined the impact of atmospheric turbulence in FSO on the transmission characteristics.

4.2.1 Experimental setup

Figure 4.11 presents the block diagram of the entire experimental setup. Each OFDM signal, comprising a Long Term Evolution Advanced (LTE-A) test model 3.1 with 64-QAM with 20 MHz bandwidth, was specifically chosen to evaluate the total dynamic range of the transmission chain [49]. These signals were initially generated at baseband

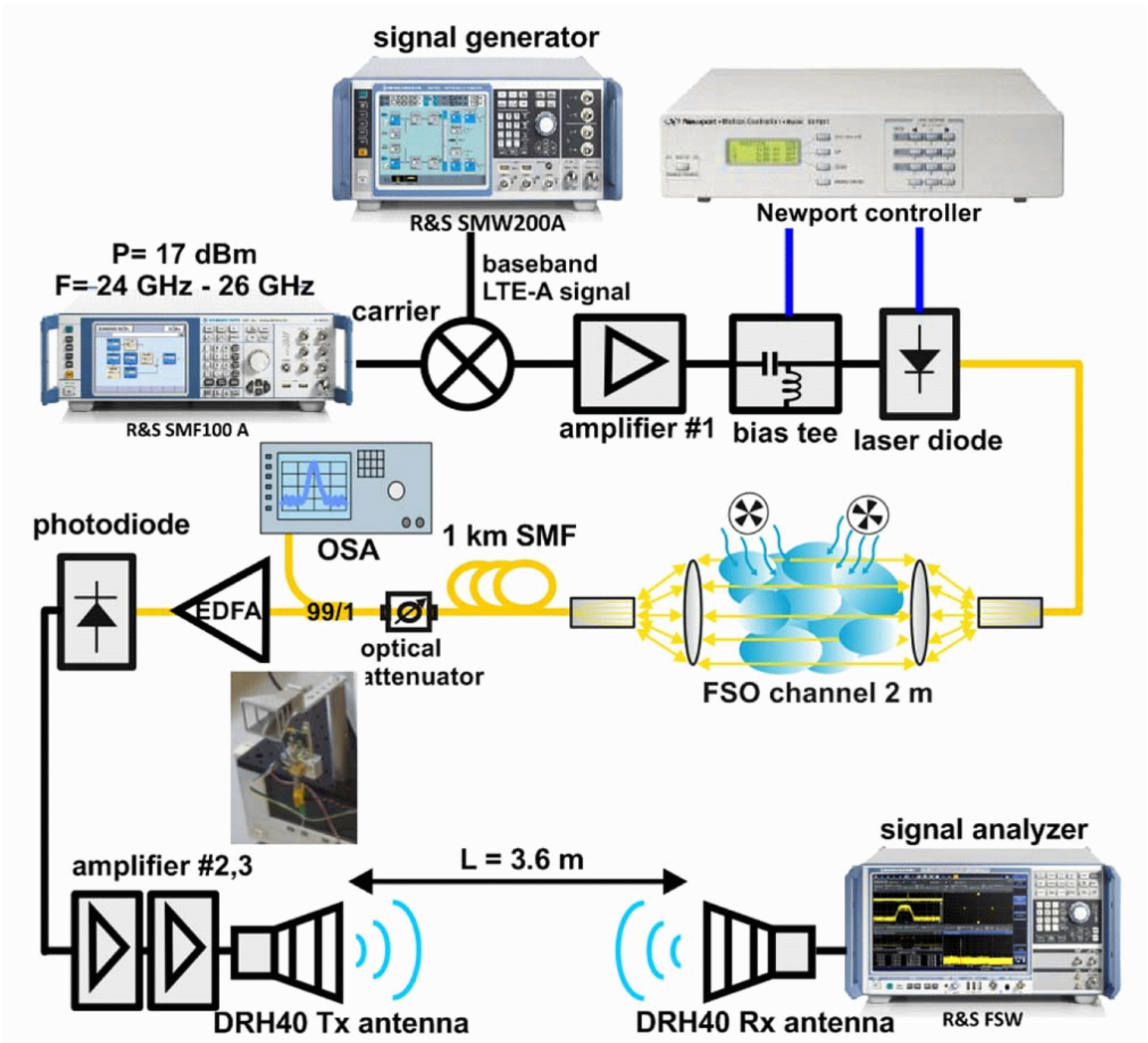

Figure 4.11: Experimental setup with DML. [51]

using an R&S SMW200A vector generator. Subsequently, they were up-converted to the 24 GHz to 26 GHz frequency band, utilizing mixer (Analog Devices HMC1041) and a local oscillator produced by the R&S SMF100A. Post-mixing, the signals required amplification, accomplished through a amplifier (Wisewave AGP-33142325-01), achieving an output RF power of 12 dBm.

The operation of the DML necessitated a bias in the RF signal, which was provided by a bias-tee. Both the Thermoelectric Cooler (TEC) within the DML and the bias to the DML were regulated using a Newport 8000 Modular Controller.

The laser's output optical power was measured at 4.8 dBm, with a wavelength of 1549 nm. This optical signal was then introduced into the FSO line, comprising gradient-index (GRIN) and plano-convex lenses. The FSO link, spanning a length of 2 m, was situated within a chamber designed to mimic turbulence.

The optical signal was subsequently introduced into a 1 km long SMF. To emulate additional losses typically encountered in optical assemblies, an variable optical attenuator was integrated at the fiber's output. Following the attenuator, a 1 % coupler was installed to facilitate signal monitoring. The optical spectrum of the signal was continuously observed using an optical spectrum analyzer connected to this coupler. Prior to detection, signal amplification was achieved through a EDFA (Keopsys KPS-BT2-C-10-LN-SA) with a gain of 15 dB, resulting in an optical power of 5 dBm at the EDFA's output. For the detection of the optical signal, an PIN diode (Optilab PD-40), which is rated for frequencies up to 40 GHz, was employed.

The detected signal undergoes amplification through a sequential arrangement of two amplifiers. Initially, it passes through a low-noise amplifier (Miteq AMF-4F-260400-40-10p), which provides a gain of 24 dB and has a noise figure of 3.3 dB. Subsequently, the signal is further amplified by an medium power amplifier (Analog Devices HMC1131), offering an additional gain of 22 dB and featuring P1dB of 23 dBm. This two-stage amplification cascade effectively generates an output RF power of 4 dBm, which is then relayed to the wireless link. The link itself is composed of a pair of double-ridged horns (RFspin DRH40), each contributing a gain of 14 dBi within this frequency band. At 24 GHz, the total loss of the wireless link, inclusive of the antenna gains, is 43.2 dB.

For the purpose of measuring the frequency response of the entire assembly, we employed the R&S ZVA67 VNA. Although not depicted in Figure 4.11, this VNA was integrated into the setup at two critical points: firstly, it was inserted at the input, preceding the first amplifier, and secondly, it was connected at the output, directly to the receiving antenna DRH 40.

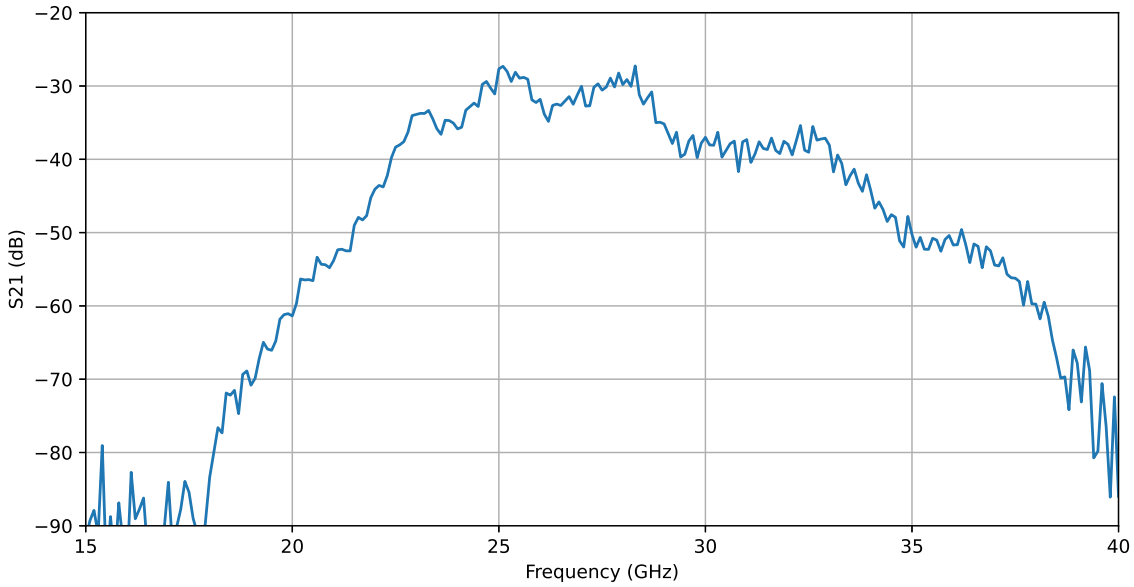

Figure 4.12: Transfer of the entire system. [51]

4.2.2 Experimental results

The transmission characteristics of the entire system were quantified using a VNA and are depicted in Figure 4.12. Within the targeted 24 GHz to 26 GHz band, the transmission level was observed to be approximately −30 dB. A significant source of noise within the system is attributed to the ASE originating from the EDFA positioned ahead of the photodiode. The observed non-uniformity in the S_{21} transmission characteristic can be explained by various factors: at lower frequencies, it is primarily influenced by the frequency response of the amplifiers, while at higher frequencies, it is predominantly due to the transmission characteristics of the DML. Additionally, the overall ripple observed in the S_{21} measurement is a consequence of multipath propagation within the wireless transmission channel.

Measurements of the EVM versus SNR were conducted using the LTE-A test model 3.1 at carrier frequencies of 24 GHz, 25 GHz and 26 GHz. These measurements were performed without any turbulence and are illustrated in Figure 4.13a. Concurrently, the maximum permissible EVM limit of 9 %, as specified in [53], is also depicted. Notably, the optimal performance was achieved at 24 GHz. This is intriguing because, as indicated by the transmission characteristics in Figure 4.12, 25 GHz shows the best transmission S_{21}, while the transmission at 24 GHz and 26 GHz is relatively comparable. This discrepancy can be attributed to the DML being specifically optimized for the 24 GHz band.

At a frequency of 26 GHz, an increased SNR penalty of 8 dB was observed to achieve the same EVM level as at 24 GHz. Nonetheless, as depicted in Figure 4.13a, it remained feasible to sustain an adequate SNR margin of 20 dB to accommodate additional optical

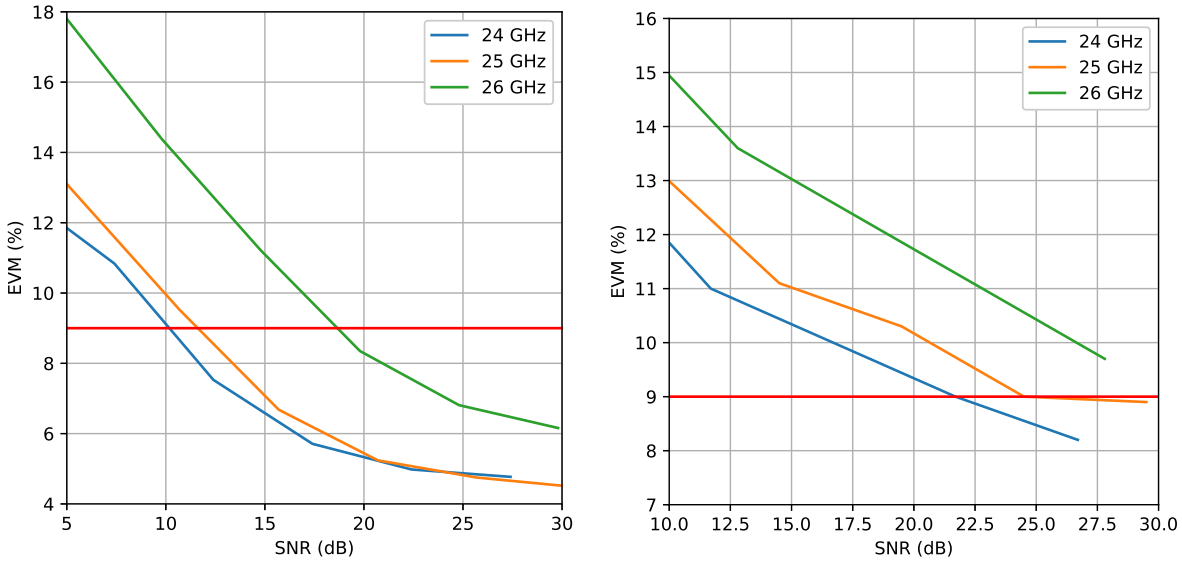

(a) No turbulence (b) Strong turbulence

Figure 4.13: Measured EVM for various SNR.[51]

losses while still maintaining to the 9 % EVM threshold.

FSO distances	Turbulence (C_n^2)
2 m	$2.4 \times 10^{-10}\,\mathrm{m}^{-2/3}$
100 m	$1.8 \times 10^{-13}\,\mathrm{m}^{-2/3}$
500 m	$9.5 \times 10^{-15}\,\mathrm{m}^{-2/3}$
1000 m	$2.7 \times 10^{-15}\,\mathrm{m}^{-2/3}$

Table 4.2: Recalculated turbulances for diferent FSO distances.

Subsequent experiments were focused on characterizing the system with turbulence in the FSO link. Turbulence was induced using hot-air heaters, and the refractive index structure parameter (C_n^2) was deduced from the measured temperature differentials [citation needed for methodology]. In our chamber, we generated very strong turbulence levels ($C_n^2 = 2.4 \times 10^{-10}\,\mathrm{m}^{-2/3}$) over a two-meter FSO link. These turbulence levels were recalculated using Rytov's variance (Eq. 1.5) to distances of 100 m, 500 m and 1000 m, in accordance with the methodology outlined in Andrews (2005) [citation], to yield more applicable insights for real-world FSO deployments. The extrapolated data are compiled in table 4.2. For the purpose of further discussions, the data corresponding to a 100 m distance will be predominantly considered.

Figure 4.13b illustrates the system's EVM under the influence of strong turbulence, measured at $1.8 \times 10^{-13}\,\mathrm{m}^{-2/3}$, as a function of the SNR at the output antenna. For carrier frequencies of 24 GHz and 25 GHz, the system is able to achieve the 9 % EVM threshold, albeit at relatively high SNRs of 22 dB and 25 dB, respectively. In contrast,

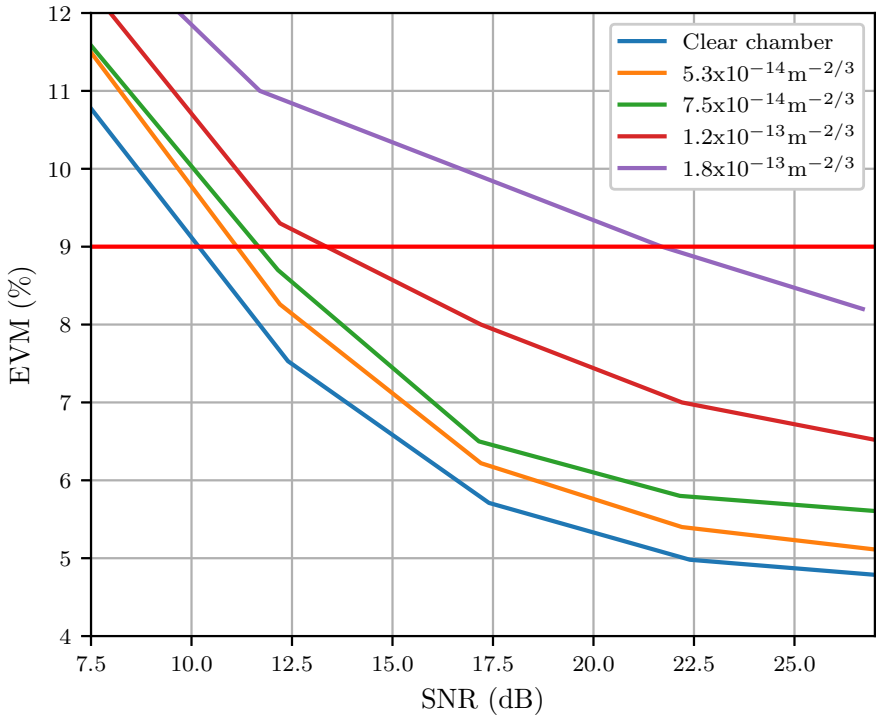

Figure 4.14: Measured EVM vs SNR for various turbulances at 24 GHz with 100 m FSO.[51]

the performance at 26 GHz does not meet the 9 % EVM limit.

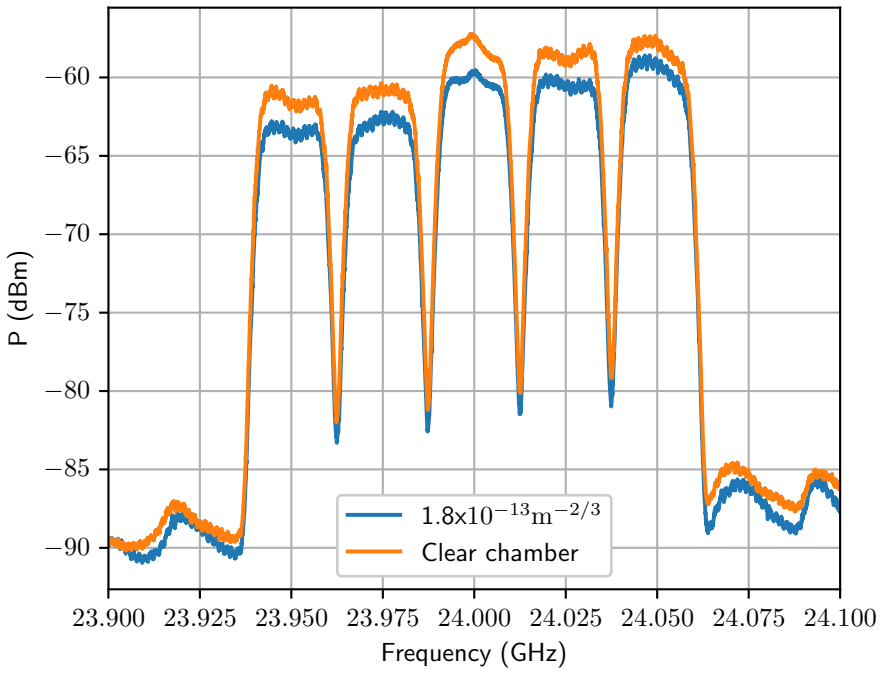

Figure 4.15: Spectrum of recieved RF signal with and without turbulances.[51]

Figure 4.14 presents the system's response at 24 GHz across varying degrees of turbulence. With the notable exception of the extremely strong turbulence ($C_n^2 = 1.8 \times$

$10^{-13}\,\mathrm{m}^{-2/3}$), the link characteristics remain fairly consistent, and the 9 % EVM limit is achievable within a 3 dB SNR margin. These observations suggest that the FSO link, when transmitting an LTE-A signal, demonstrates considerable robustness to turbulence.

In our final analysis, we examine the impact of FSO turbulence on the RF spectrum of the signal. Observations from Figure 4.15 indicate that while the turbulence has a minimal effect on the signal's long mean amplitude, it significantly impairs the EVM, deteriorating it from 3 % to 8 %. This substantial degradation in EVM is attributed to the rapid time variation in the amplitude of the received signal caused by turbulence.

4.2.3 Discussion

We posit that the performance of both RoF and Radio over RoFSO in terms of EVM can be further optimized by integrating additional optical bandpass filters. These filters would serve to attenuate out-of-band noise, notably that originating from the EDFA. Such noise currently contributes to the aggregate detected noise at the photo diode. By employing these filters, it becomes feasible to increase the gain from the EDFA while incurring a lower noise penalty, as the EDFA's noise figure would be effectively reduced in this specific configuration.

Fast fading effects can be mitigated by adopting OFDM with significantly reduced symbol rates on the subcarriers. However, this approach introduces a considerable latency in data transmission. Additionally, it's important to note that LTE-A standards do not accommodate such low symbol rates. Consequently, this method may be more suited for alternative service types that can tolerate increased transmission delays, rather than for typical LTE-A applications.

The system we have developed demonstrates robust operation in high-turbulence FSO environments. Notably, it maintains a SNR margin of 20 dB. This margin can be advantageously utilized to extend either the SMF link or the FSO link, provided that the turbulence in the latter scenario is comparatively lower.

Consequently, the utilization of DML emerges as a highly promising technology for facilitating connectivity within the CRAN framework, especially between the BBU pool and the Remote Radio Heads. This technology is particularly advantageous for establishing two-way links. The simplification of optical interconnections on the RRH side, enabled by DML, significantly supports their widespread deployment, an essential factor in the evolving landscape of wireless network infrastructure. Conceptually, this simplification is shown in Figure 4.10.

This demonstrates significant potential for 5G network architectures, indicating the feasibility of achieving data transmission speeds of up to $1\,\mathrm{Gbit\,s^{-1}}$.

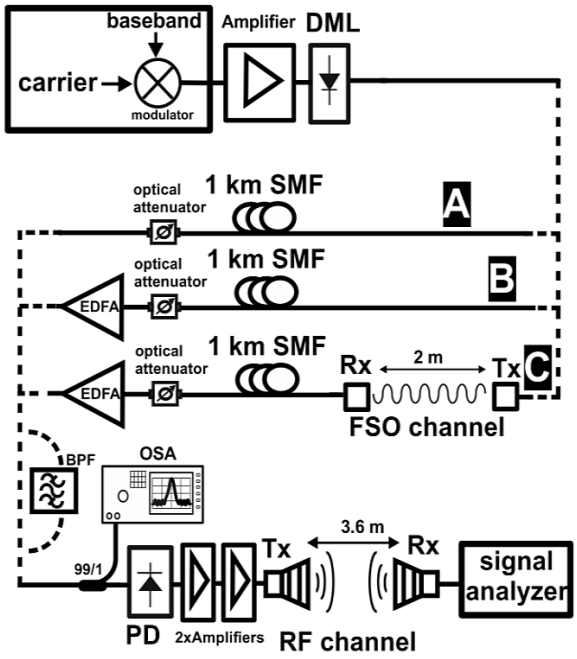

Figure 4.16: Proposed experimental setup [50]

4.3 Further investigation of directly modulated lasers for 5G networks

In our ongoing research, we have explored the application of directly modulated lasers for use in 5G networks. Specifically, in Chapter 4.2, we conducted an experimental test to assess the viability of employing such lasers in a particular scenario. The initial results were promising, leading us to further refine and expand our experimental investigations.

In the next experimental setup, we modified the original system described in Chapter 4.2 by integrating an optical bandpass filter. This modification was based on the discussions and theoretical underpinnings presented in Chapter 4.2.3, aiming to enhance system performance and reliability.

4.3.1 Experimental setup

In this experimental phase, detailed in Chapter 4.2, we retained a similar setup with a key modification: the optical path was branched into three distinct configurations for comprehensive analysis.

Path A comprises a 1 km SMF coupled with an optical attenuator. Path B extends Path A by including an EDFA. Path C is the most complex, integrating a 2 m FSO link with an 1 km SMF, an optical attenuator, and an EDFA. The modifications of experimental block diagram is depicted in Figure 4.16.

A critical aspect of the study was the investigation of the bandpass filter's role in the

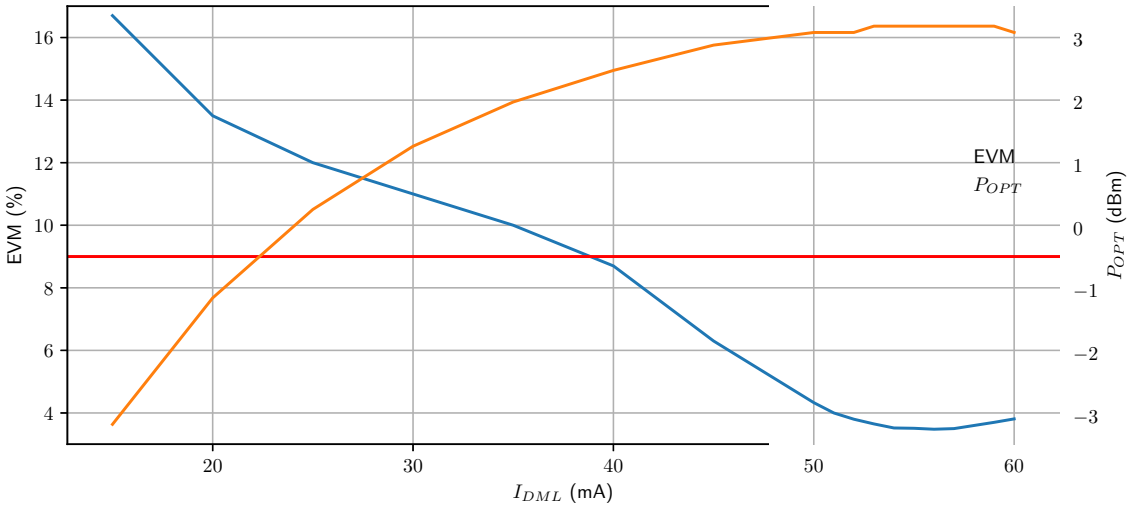

Figure 4.17: EVM as a function of the bias current of DML [50]

optical path, particularly following the EDFA. This filter is presumed to be a principal mitigator of broadband ASE noise originating from the EDFA. The central wavelength of this filter is 1549.23 nm and insertion loss is 4 dB.

The remaining components of the setup were unchanged from those described in Chapter 4.2.1, ensuring consistency in the experimental conditions. We used same E-UTRA test model TM 3.1.

4.3.2 Experimental results

To improve the performance parameters of both the RoF and RoFSO links, we focused on optimizing the bias current supplied to the laser. The optimization tests were conducted at a carrier frequency of 24 GHz, using a modulated signal with a bandwidth of 100 MHz. We specifically assessed the EVM of one transmitted OFDM LTE signal. These evaluations were carried out in the configuration that was anticipated to yield the most significant improvement, namely path C (Figure 4.16). This path was selected due to its highest insertion loss.

The DML optimization of this measurement is presented in fig 4.17. The optimal operating point for the DML was identified at a bias current of $I_{OPT} = 53$ mA, where the lowest EVM recorded was 4.9 %. This bias current setting of 53 mA was consistently employed for all subsequent measurements. Figure 4.17 also show output laser power for given current I_{OPT}.

In light of the industry's prevalent use of a more than bandwidth of 20 MHz, we conducted two sets of measurements: one using a transmitted signal bandwidth of 20 MHz and the other with a 100 MHz bandwidth, equivalent to five times the 20 MHz LTE OFDM signal. These measurements were carried out using the setup in path A of Figure 4.16.

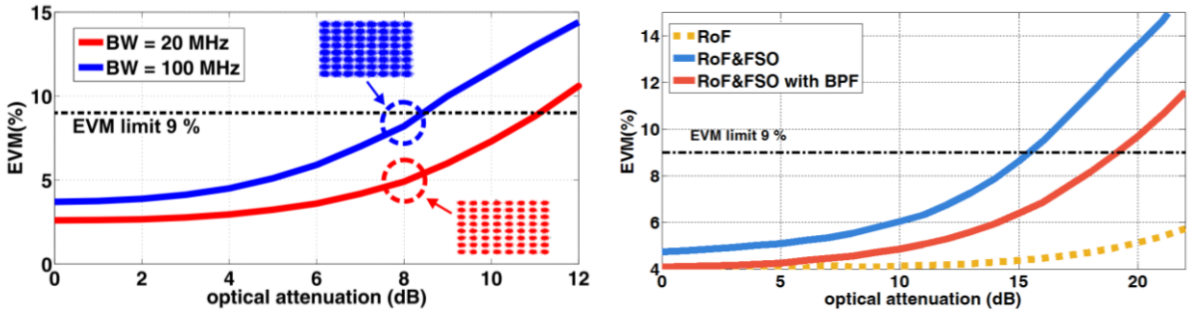

(a) EVM measured for path A (b) EVM measured for path B and C

Figure 4.18: The measured EVM vs the optical attenuation.[50]

We varied the insertion loss in the optical path by adjusting an optical attenuator. Figure 4.18a displays the resulting correlation between the EVM and the optical attenuator settings. Additionally, the Figure includes the EVM limit of 9 %, as stipulated by [53].

Across the entire range of optical attenuation, the overall EVM for the 100 MHz bandwidth was inferior compared to the 20 MHz bandwidth. Specifically, it was 1.2 % worse at 0 dB of attenuation, and the 20 MHz signal bandwidth could withstand at least 2.5 dB more insertion loss than the 100 MHz bandwidth.

Incorporating the EDFA before the detection diode substantially enhanced the system's resilience to optical insertion loss, as depicted in fig 4.18b. This Figure compares the configurations of path B, path C without an optical bandpass filter, and path C with an optical bandpass filter included before the detection diode.

For the pure RoF setup (path B), the EVM limit was not reachable under any optical insertion loss of our attenuator. With the addition of the FSO link (path C), the EVM worsened due to increased insertion loss. The threshold EVM value was reached at an additional attenuation of 15.5 dB with the optical attenuator. Introducing the optical bandpass filter into the path improved the overall EVM. At low insertion losses up to 5 dB, the path with FSO mirrored the performance of path B without FSO. However, at higher insertion losses, the system began to degrade; the EVM limit was reached at an insertion loss of 18.5 dB, which is still 3 dB better than the setup without the filter.

Lastly, we conducted a comparative analysis of the optical spectrum of the transmitted signal. Figure 4.19 presents the spectrum of the signal originating from the DML, as well as the signal after traversing the FSO link (path C), and following amplification by the EDFA. It is evident from the Figure that the EDFA is set to compensate the attenuation along the entire optical path, achieving an output power of 9.3 dBm. A significant contribution of ASE noise from the EDFA is also observable. Consequently, the insertion of a filter into the system, which effectively eliminates this noise, results in a marked improvement in overall system performance.

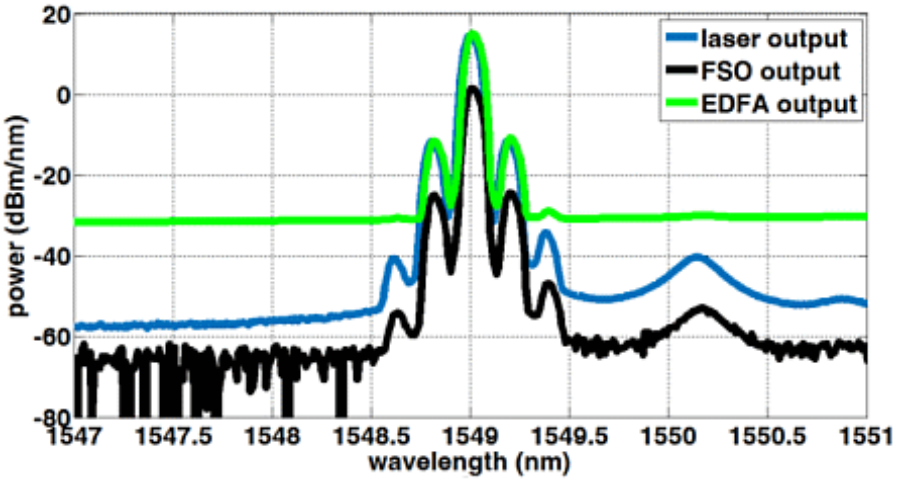

Figure 4.19: Measured optical spectrum at different positions in system.[50]

4.3.3 Discussion

This investigation published in [50] served as a complement and extension to the findings reported in chapter 4.2. A significant aspect of this subsequent experiment involved testing the implementation of an optical bandpass filter post-EDFA, a concept initially proposed in section 4.2.3. The experimental results validated our hypothesis: filtering out the ASE noise from the EDFA leads to a substantial enhancement in the transmission characteristics of both RoF and RoFSO links. This improvement was particularly pronounced in the RoF system, which does not suffer from the additional attenuation characteristic of FSO links. For the FSO link, the integration of the filter resulted in a lower initial EVM and increased resilience to insertion loss in the optical path.

4.4 M-QAM transmission over hybrid microwave photonic links at the K-band

This chapter introduces the experimental demonstration of a hybrid optical network that employs photonic doubling for the generation of a 25 GHz mmW, in alignment with the frequency band recommendations for the 5G networks. The experimental setup included a SMF path, a FSO link, and a wireless link. Our investigation focused on the impact of various factors affecting the optical channel on the transmitted signal. These factors included CD, atmospheric turbulence, and fading due to multipath propagation. In the first experimental configuration, a 64-QAM signal with bandwidths of 5 MHz, 20 MHz and 50 MHz was transmitted over a 5 km SMF and a 2 m FSO link in a chamber designed to simulate atmospheric turbulence, followed by a 3 m wireless link. The findings indicated that the 64-QAM signal, particularly at larger bandwidths, is significantly impacted by

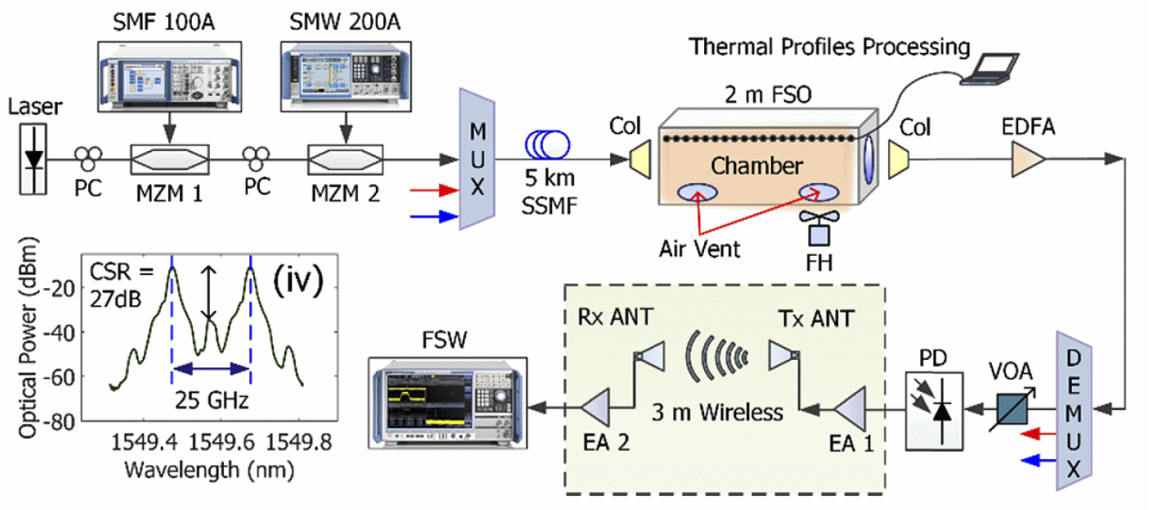

Figure 4.20: Setup A experimental configuration with short 3 m FSO.[54]

atmospheric turbulence.

In the second configuration, a 4/16/64-QAM signal with a bandwidth 50 km was transmitted over an SMF and a 40 m FSO link, coupled with a wireless link. The EVM of the transmitted signal was observed to be well below the threshold values for the signal, implying high-quality transmission. The estimated BER was found to be lower than the limit of a typical self-correcting hard-decision code, indicating a robust transmission performance.

Both experimental setups employed externally modulated laser, utilizing a 25 GHz carrier frequency. This frequency was generated through frequency multiplication, with an optical carrier suppression scheme, implemented using an optical modulator.[26], [27]

4.4.1 Experimental setup A

Setup A, designed to assess the impact of turbulence and system linearity, is depicted in Figure 4.20. The transmission side incorporates an laser (ID Photonics CoBrite-DX4) as the optical signal source. The laser signal is first routed through a polarization controller and then modulated by a MZM 1. MZM 1 modulates the signal using a LO with a frequency of 12.5 GHz and power of 18 dBm from a signal generator (Rohde & Schwarz SMF 100A). MZM 1 is biased at the minimum transmission operating point, producing an output spectrum with two 25 GHz sidebands and a suppressed optical carrier, achieving a carrier suppression of 27 dB at a bias voltage of 3.4 V. We set the input power to 18 dBm to achieve optimal transmission performance. This setting was determined after conducting a power sweep, the results of which are presented in Figure 4.21a.

Subsequently, a MZM 2 receives a 64-QAM modulated signal at an intermediate frequency of 200 MHz and power of 4 dBm, generated by a vector signal generator (Rohde

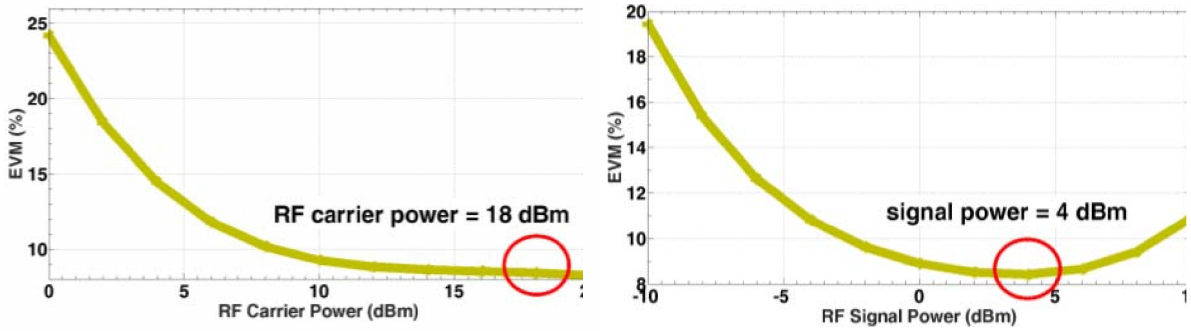

(a) EVM vs RF power of MZM 1 (b) EVM vs RF power of MZM 2

Figure 4.21: Power optimization of RF power to MZMs. [5]

& Schwarz SMW 200A). We selected an input power level of 4 dBm following a series of tests across a power range from −10 dBm to 10 dBm. This particular power level was chosen as it yielded the lowest EVM, as evidenced in Figure 4.21b.

The modulated signal then passes through a Wavelength Division Multiplexing (WDM) multiplexer and travels over a 5 km long SMF. In the FSO link chamber, optical collimators (Thorlabs F810APC-1550) are employed. The chamber for simulating atmospheric turbulence utilizes two hot-air heaters as turbulence generators, measuring 2 m × 0.4 m × 0.4 m. Temperature sensors placed at 10 cm intervals along the chamber's length facilitate turbulence level measurement. These temperature differentials are used to calculate the refractive index parameter C_n^2 according to equations 1.3 and 1.4.

The average C_n^2 values without and with turbulence are $2.4 \times 10^{-14}\,\mathrm{m}^{-2/3}$ and $3.2 \times 10^{-11}\,\mathrm{m}^{-2/3}$ respectively. These C_n^2 values for the chamber are convertible to distances typical in FSO applications. For the high turbulence value of $3.2 \times 10^{-11}\,\mathrm{m}^{-2/3}$, this equates to $1.3 \times 10^{-15}\,\mathrm{m}^{-2/3}$ for a 500 m distance and $3.6 \times 10^{-16}\,\mathrm{m}^{-2/3}$ for 1000 m, as per equation 1.5.

Post FSO link, the signal goes through a short SMF segment to an EDFA (Keopsys KPSBT2-C-10-LN-SA), amplifying signal to an output optical power of 3 dBm. A WDM demultiplexer follows, and the signal is finally received by a PIN detection diode (Optilab PD-40). The optical signal is further amplified by an EA 1 amplifier (Miteq AMF-4F-260400-40-10p) with a gain of 24 dB and a noise figure of 3.3 dB.

The setup concludes with a 3 m long wireless link utilizing double-ridged waveguide horn antennas, each with a gain of 14 dBi at 25 GHz. An EA 2 amplifier (HMC1131) with a gain of 22 dB enhances the signal at the receiving antenna, which is then analyzed by a Rohde & Schwarz FSW signal analyzer.

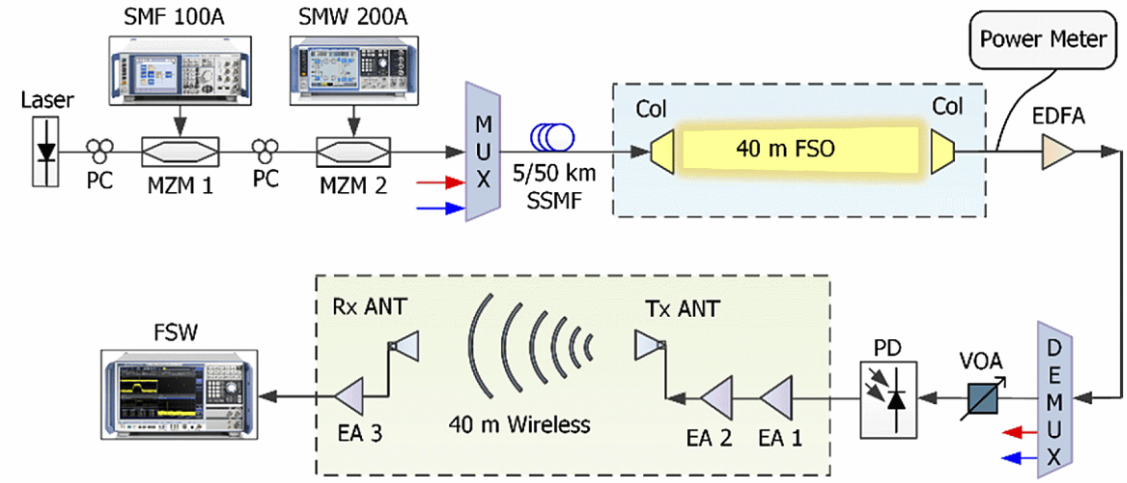

Figure 4.22: Setup B experimental configuration with 40 m FSO and 40 m wireless link.[54]

4.4.2 Experimental setup B

The second series of experiments was conducted using Setup B, located in the corridor of the Faculty of Electrical Engineering. As depicted in Figure 4.22, the FSO and RF link spanned a distance of 40 m in this corridor. Differing from Setup A, these experiments utilized varying modulation formats (4/16/64-QAM) while maintaining a consistent bandwidth of 20 MHz. The SMF lengths were set at 5 km and 50 km.

The output optical power of the FSO link was continuously monitored using a power meter connected to a 1 % tap from the optical link. This power measurement was crucial for verifying the correct alignment of the FSO link. At a distance of 40 m, the FSO link exhibited an attenuation of 12 dB. The EDFA output power was regulated to 7 dBm.

In this setup, the EA 2 amplifiers were repositioned to follow the EA 1 amplifier. Subsequently, an additional EA 3 amplifier (Miteq AMF-4F-260400-40-10p) was connected to the output of the receiving antenna.

The remainder of the setup was identical to that used in the previous experiments.

4.4.3 Experimental results of setup A and discussion

Figure 4.23 illustrates the relationship between the EVM and the received RF power for a 64-QAM signal with bandwidths of 5 MHz, 20 MHz and 50 MHz, as transmitted by Setup A. Additionally, the Figure includes the 8 % EVM threshold for 64-QAM, as specified in [53]. By implementing an optical tunable attenuator prior to the detection diode, we varied the optical power at the diode, thereby altering the RF received power, which is represented on the X-axis.

The results indicate that the 5 MHz and 20 MHz bandwidth signals consistently remain below the 8 % EVM threshold, unaffected by perturbations. Conversely, the 50 MHz

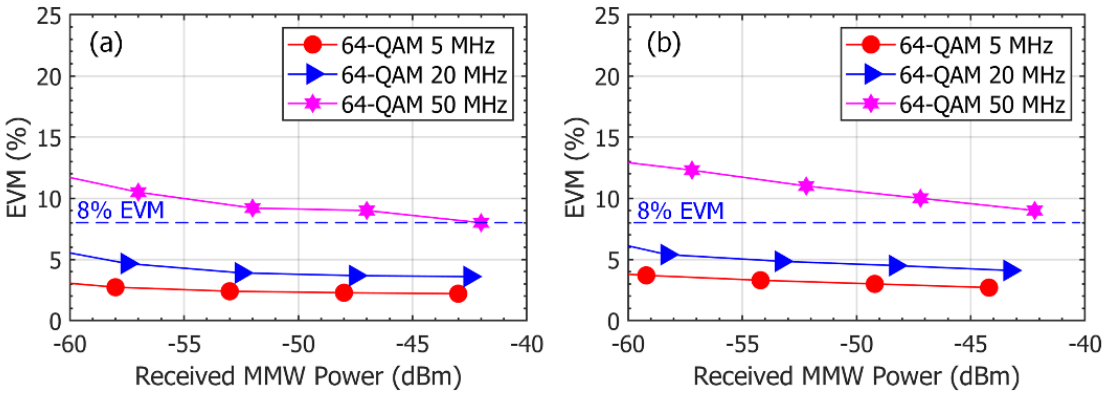

Figure 4.23: EVM vs. receiver RF power of setup A. Left without turbulences, right with turbulences.[54]

bandwidth signal surpasses this limit at all received power levels. This phenomenon is attributed primarily to two factors. Firstly, there is a decrease in SNR due to the inclusion of a broader noise bandwidth. Secondly, the coherent detector in the receiver exhibits reduced integration time, leading to noticeable power drops during rapid signal fluctuations, as discussed in [39].

	Without Turbulence		With Turbulence	
64-QAM bandwidth [MHz]	EVM [%]	BER [-]	EVM [%]	BER [-]
5	2.2	$<1 \times 10^{-12}$	2.7	$<1 \times 10^{-12}$
20	3.6	3.9×10^{-10}	4.1	2.9×10^{-8}
50	8.0	1.9×10^{-3}	9.1	9.0×10^{-2}

Table 4.3: Measured EVM and calculated BER of setup A.[54]

$$\mathsf{BER}_{M-QAM} = \frac{2}{\log_2(M)}\left(1 - \frac{1}{\sqrt{M}}\right)\mathsf{erfc}\left(\sqrt{\frac{3}{2(M-1)}\frac{1}{\mathsf{EVM}^2}}\right) \tag{4.8}$$

Table 4.3 summarizes these experimental findings. Concurrently, the Bit Error Rate (BER) was computed for the maximum received RF power. Given that the turbulence was only moderate, its impact on EVM is relatively minimal. Utilizing eq. 4.8, we converted the EVM values into their corresponding BER estimates. In eq. 4.8 erfc is complementary error function defined as:

$$\mathsf{erfc}\,(z) = 1 - \frac{2}{\sqrt{\pi}}\int_0^z e^{-t^2}\,dt \tag{4.9}$$

And M is number of symbols in modulation.

A critical factor in determining the viability of the overall system for deployment is its linearity and dynamic range. We assessed linearity by measuring the second and third products of nonlinear distortion. Typically, these distortion products are quantified by the

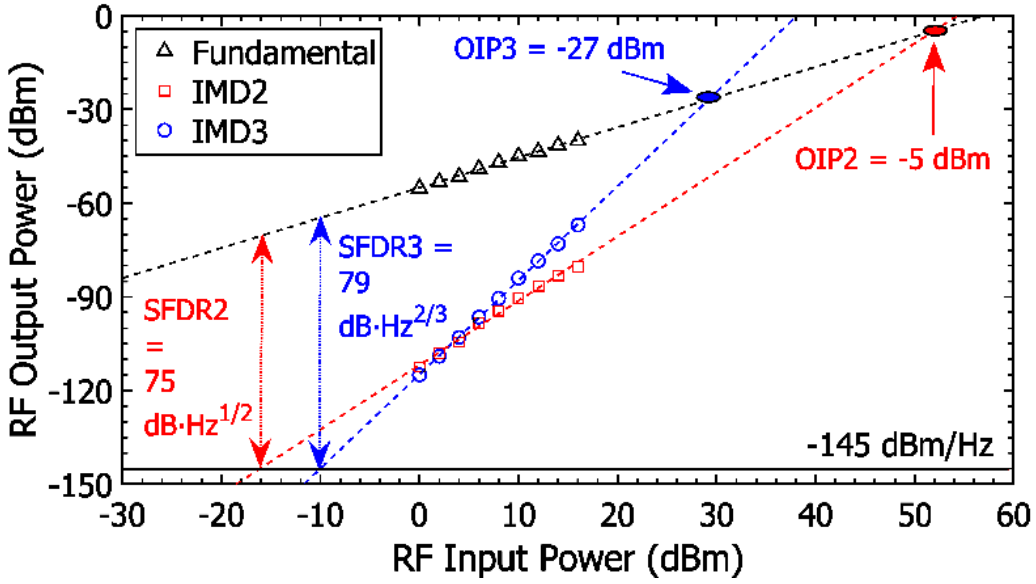

Figure 4.24: SFDR and spurious-free dynamic range of setup A.[54]

third-order intercept point (IP3) and the second-order intercept point (IP2). Additionally, it is common to specify whether these intercept points are defined in terms of input (I) or output (O).

The linearity measurements were conducted using a 25 GHz carrier, which was generated by doubling the 12.5 GHz LO frequency. Intermediate Frequency (IF) tones were set at 200 MHz and 201 MHz. The experimental setup for these measurements remained consistent with that depicted in Figure 4.20.

Figure 4.24 displays the measured values of harmonic distortion products alongside the calculated parameters for Output Third-Order Intercept Point (OIP3) and Output Second-Order Intercept Point (OIP2). Additionally, it shows the measured background noise level at -145 dBm/Hz and the calculated dynamic ranges where these distortion products fall below the noise level, known as the SFDR.

The calculated SFDR values are 75 $\mathrm{dBHz}^{2/3}$ for SFDR2 and 79 $\mathrm{dBHz}^{2/3}$ for SFDR3. In the context of wideband signal transmission, our primary focus is on the third-order distortion products and, consequently, the SFDR3. This is due to the third-order products falling back into the band of the modulated signal, making them more critical for system performance.

4.4.4 Experimental results of setup B and discussion

Setup B, as depicted in Figure 4.22, was evaluated in two configurations with 5 km and 50 km SMF lengths. The measurements utilized OFDM signals with 4/16/64-QAM modulation on subcarriers, following the guidelines of [53]. Specifically, test models TM3.3,

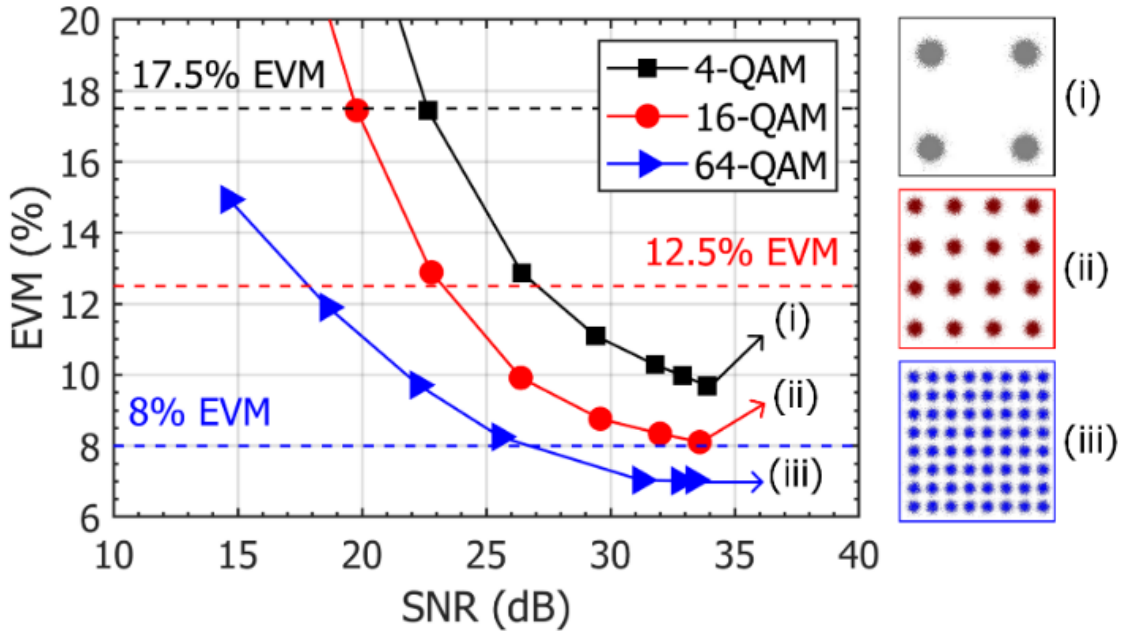

Figure 4.25: EVM vs. SNR on the signal analyzer of setup B.[54]

TM3.2, and TM3.1 were employed. Both the SNR at the RF output and the EVM of the received signal were measured. The SNR adjustments were facilitated by an variable optical attenuator placed before the detection diode.

The resulting measurement trends are presented in Figure 4.25, along with their respective limits (8 %, 12.5 % and 17.5 %) as specified in [53]. The lowest recorded EVM values for 4/16/64-QAM were 9.6 %, 8.1 % and 7 %, respectively. These results may appear counterintuitive; typically, a reduction in the number of states in the constellation would lead to a decrease in EVM due to increased distances between individual symbols.

As for the BER values, they were measured at 1×10^{-12}, 1.3×10^{-8} and 5.3×10^{-4}, which are within the limits for Hard-Decision Forward Error Correction (HD-FEC). Therefore, the output from a decoder for this setup would be error-free.

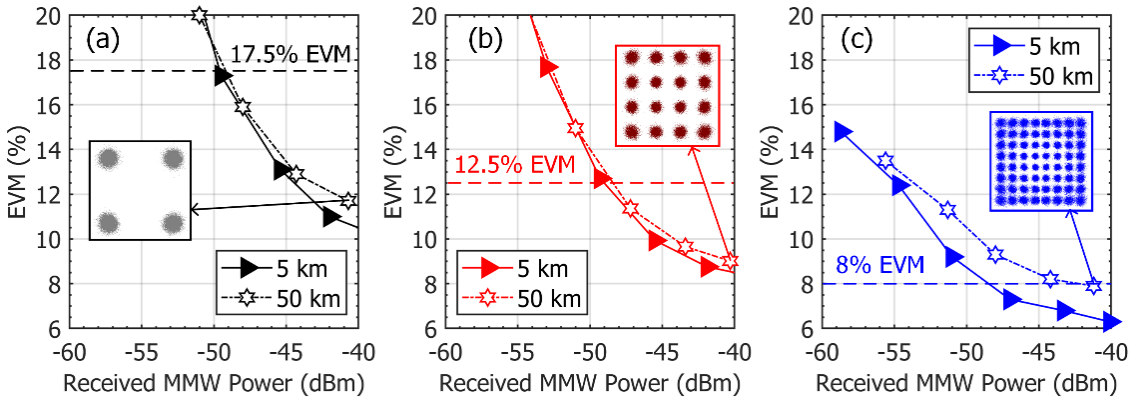

Figure 4.26: EVM vs. receiver RF power of setup B.[54]

M-QAM	EVM (%)	BER [-]
QPSK	11.7	1×10^{-12}
16-QAM	9.0	2.5×10^{-7}
64-QAM	7.9	1.7×10^{-3}

Table 4.4: Measured EVM and calculated BER of setup B.[54]

Figure 4.26 illustrates the variation of the EVM with respect to the received power for SMF lengths of 5 km and 50 km. The 50 km distance represents the maximum length considered viable for deploying such systems in rural areas. The feasibility of using this length primarily stems from the resilience of Optical Carrier Suppression (OCS) modulation against CD in the fiber. As depicted in Figure 4.26, the performance disparity between the 5 km and 50 km lengths is notably minimal.

In all tested scenarios, HD-FEC is applicable and effective, as the resultant BERs consistently remain below the threshold of 3.8×10^{-3}. Comprehensive results for the 50 km SMF configuration are detailed in Table 4.4.

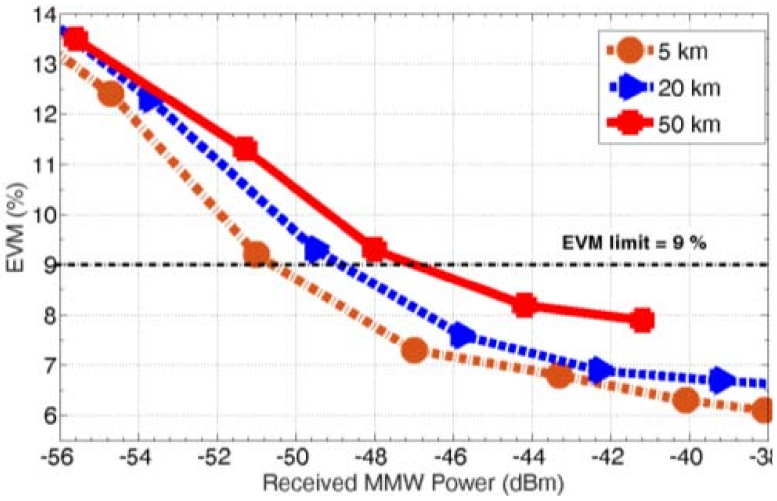

Figure 4.27: EVM if relation to the recieved RF power.[5]

In our experiments, we utilized DSB-SC signal generation, known for its robustness to CD. To assess the impact of fiber length on transmission, we conducted tests with different lengths of SMF. The test employed the TM-3.1 model with 64-QAM on subcarrier of OFDM at 25 GHz, using SMFs of 5 km, 20 km and 50 km. Figure 4.27 displays the resulting waveforms in relation to the received RF power. Notably, the difference in EVM between the 5 km and 50 km lengths is a mere 3 dB for an EVM limit of 9 %, largely attributed to the attenuation compensation by the EDFA.

From these results, it is evident that the length of the SMF does not significantly affect the outcome, within the tested range. However, it should be noted that a length of 50 km represents approximately the maximum feasible transmission delay for a 5G network.

4.4.5 Conclusion

The results of our study, as detailed in [5], [54], encompassed the design and experimental validation of RoF and RoFSO systems operating in the K-band at 25 GHz. These systems were evaluated in two distinct configurations. Our experiments demonstrated the impact of atmospheric turbulence on the RoFSO link, particularly for bandwidths of 5 MHz, 20 MHz and 50 MHz. Additionally, we quantified the nonlinear distortion and the Spurious-Free Dynamic Range inherent in such a link.

A potential enhancement to mitigate the nonlinear characteristics of the system could involve adopting coherent detection. However, this approach would entail a trade-off, resulting in increased complexity on the receiver side of the system.[55]

4.5 Comparative experimental analysis of three RoF generation methods at 25 GHz

This section presents an experimental analysis comparing three types of lasers used in RoF transmission: a DML as discussed in section 1.4.1, and two indirectly modulated lasers –an EAM and a MZM, detailed in section 1.4.2. The primary aim of this document is to explore the implementation and characterization of a RoF transmitter suitable for 5G networks, focusing on broadband signal transmission in free space.

The experimental procedure involves indoor tests to compare the transmission characteristics of these different modulators. We adjusted settings to optimize transmission quality and conducted two types of evaluations: first, assessing pure transmission using a VNA, and second, measuring test model LTE signal performance and analyzing the resultant EVM.

Additionally, the outdoor experiment encompasses the verification of these transmission characteristics in a practical setting. This involves utilizing the optical infrastructure at the Faculty of Electrical Engineering and conducting RF transmission tests over a distance of 50 m.

4.5.1 Experimental setup

Initially, laboratory measurements were conducted as per the setup shown in Figure 4.28. We generated the test signal in baseband using a vector signal generator (R&S SMW200A) and upconverted it to the 22.5 GHz to 26.5 GHz band using a mixer and an LO generator (R&S SMF100A). For all measurements, we used the LTE TM-3.2 [33] signal with a 20 MHz bandwidth. This signal, consisting of OFDM modulation with 16-QAM on

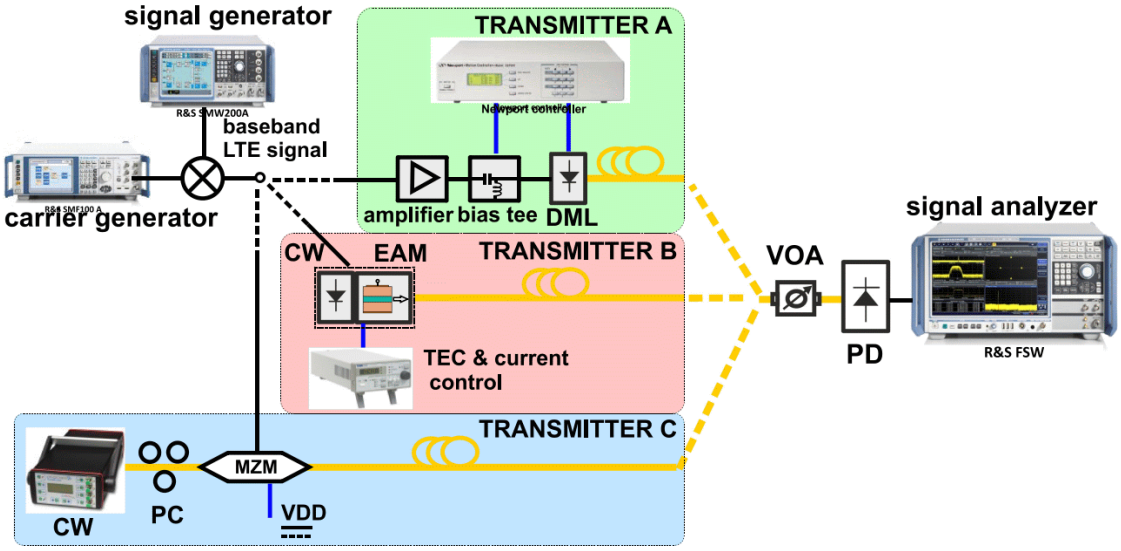

Figure 4.28: Indoor test setup for performance comparison between different modulation sources.[56]

subcarriers, is well-suited for assessing the dynamic range of the transmission chain [49]. The mean power of the upconverted output signal was −10 dBm.

Transmitter	Employed scheme	Modulation bandwidth −3 dB [GHz]	Optical output power [dBm]	Side-mode suppression ratio [dB]	Static extinction ratio [dB]
Transmitter A	DML	≥35	≥1.6	≥50	≥30
Transmitter B	EAM	≥32	6.7	≥35	≥15
Transmitter C	MZM	≥25	6.6	≥40	≥20

Table 4.5: Transmitter comparation. [56]

Transmitter A employed a monolithically-integrated passive feedback DML (HHI Berlin, identical to the one used in chapter 4.2). The setup required external bias-t, a bias controller, and temperature stabilization controller, all provided by a Newport 8000 Modular Controller. The bias current and TEC temperature were set to 59 mA and 35 °C, respectively, with an output optical power of 1.6 dBm. DML was driven by amplifier (Wisewave AGP-33142325-01) with gain of 25 dB and max output power 23 dBm

Transmitter B utilized an EAM (OKI OSC-LDS-EML-C-500C), combined with a CW laser. The laser's bias current was 100 mA, and the TEC temperature was set to 35 °C, controlled by Thorlabs LDC205C and TED200C. The output optical power was 6.7 dBm.

For Transmitter C, we used an external CW laser (CoBrite DX4) with variable wavelength and a MZM (Fujitsu FTM7938EZ/201), biased at the quadrature point, with an output optical power of 6.6 dBm.

Given that systems' power consumption is mainly in RF signal conditioning (mainly amplifiers) and since all lasers require TEC and have similar bias currents, the transmitters

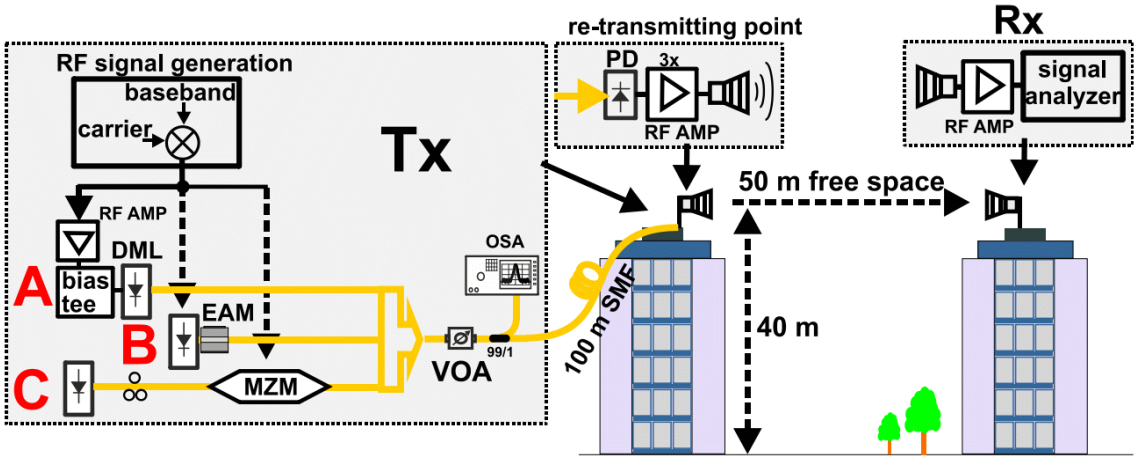

Figure 4.29: Outdoor test setup for performance comparison between different modulation sources.[56]

are comparable in power usage. However, the DML, requiring a substantial input RF signal, is less efficient in terms of power consumption due to the need for a power amplifier as the laser exciter. The estimated laser power consumption of transmitters is around 0.5 W, though this may vary based on the type of laser exciter and TEC used (linear or switched).

Post-laser and modulator, the setup included an adjustable optical attenuator (DA-100-SC-1300/1550-9/125-S-40) and 100 m of SMF. An detection diode (Optilab PD-40) detected the optical signal, and an R&S FSW served as the signal analyzer.

For outdoor measurements, as per Figure 4.29, we utilized the transmission link between the blocks of the electrical engineering faculty building, length 50 m at a height of 40 m above ground. The photodetector was connected through 100 m of SMF to simulate optical infrastructure connectivity. This setup demonstrated that increasing the SMF length is feasible without significant issues.

RF signal conditioning at the photodetector output was necessary to amplify the signal sufficiently for wireless RF channel transmission. Thus, three amplifiers (Miteq AMF-4F-260400-40-10p, Analog Devices HMC1131, and Qorvo TGA4536-SM) were connected. The TGA4536-SM amplifier, with a P1dB of 33 dBm, aligned with typical transmitted power levels. The average power of the modulated signal was around 21 dBm.

A pair of double-ridged horn antennas (RFspin DRH40) with a gain of 14 dBi in this frequency band were employed for transmission and reception. The Free Space Loss (FSL) at 25 GHz was 94.4 dB. An Low-Noise Amplifier (LNA, Miteq AMF-4F-260400-40-10p) was immediately connected to the receiving antenna to prevent SNR degradation from the 3 m long coax (loss of 9 dB at 24 GHz), which then connected to the signal analyzer.

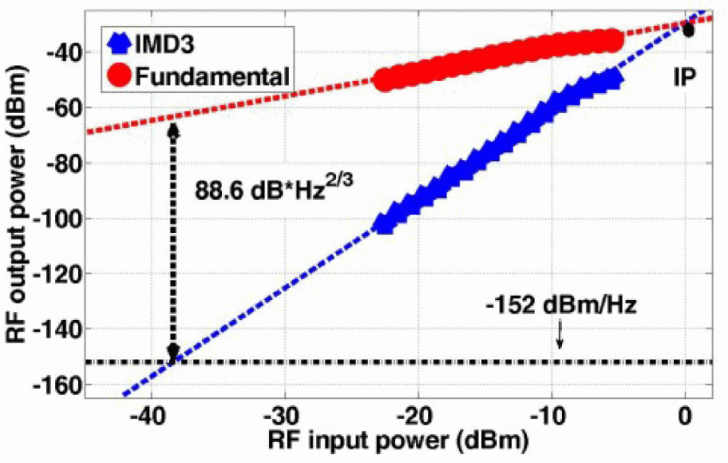

(a) Transmitter A (DML)

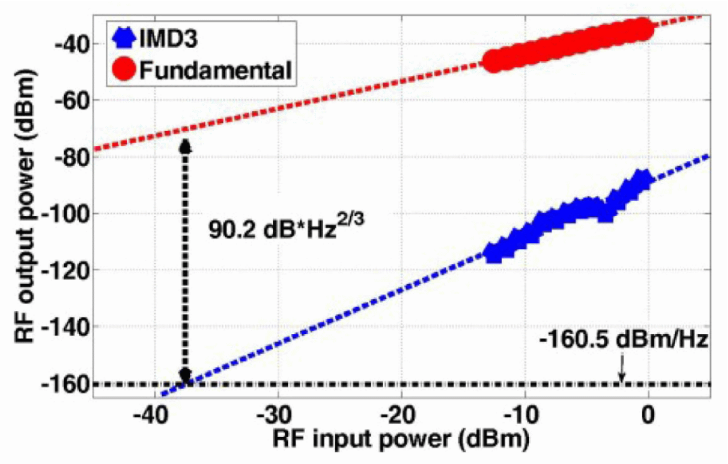

(b) Transmitter B (EAM)

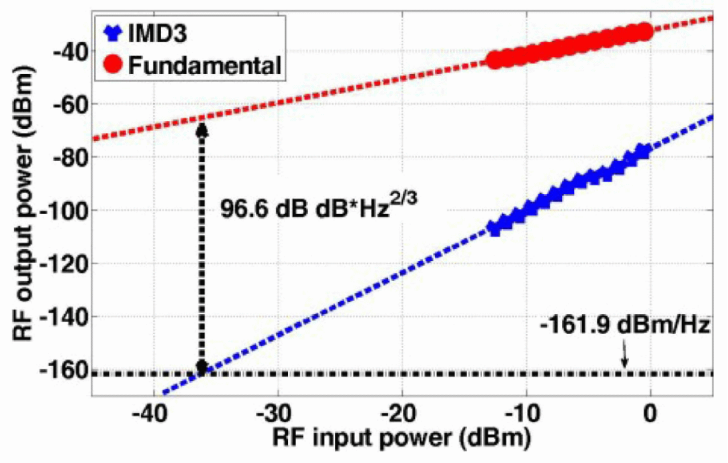

(c) Transmitter C (MZM)

Figure 4.30: Measured intermodulation products and SFDR and IMD3 of transmitters. [56]

4.5.2 Indoor experiments

Initially, we compared the transmitters in terms of linearity by measuring the IMD3, SFDR, and IP3.

These measurements were conducted at 25 GHz using two tones spaced 1 MHz apart. The results are depicted in Figure 4.30. Notably, the same photodiode was used for all measurements to ensure consistency, with its influence equally contributing to each measurement.

The determined SFDR from measurement values for transmitters A, B, and C at input IP3 were 88.6 $\mathrm{dBHz}^{2/3}$, 90.2 $\mathrm{dBHz}^{2/3}$ and 96.6 $\mathrm{dBHz}^{2/3}$ at 0 dBm, 50 dBm and 31 dBm, respectively. Transmitter C exhibited the highest SFDR. Transmitter A had the lowest SFDR, primarily due to the high background noise of −152 dBm/Hz generated by the DML. Additionally, the input IP3 of transmitter A was affected by the input amplifier, which was included in the measurement as it was used for all other measurements.

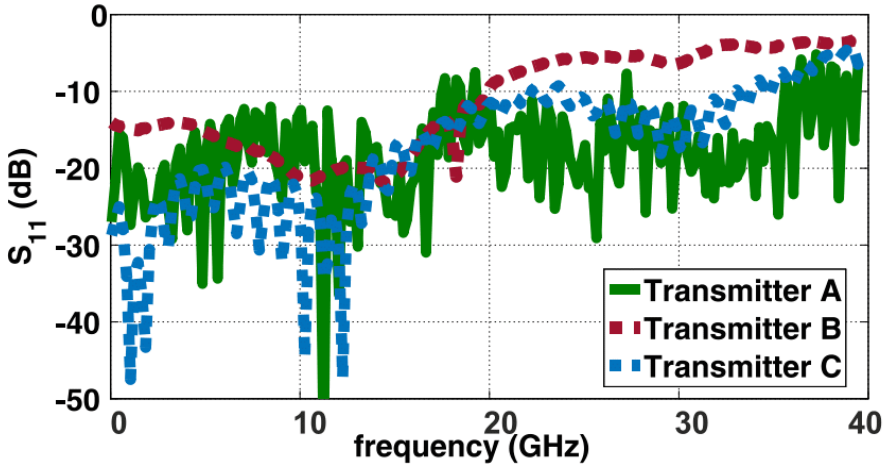

(a) S_{11}

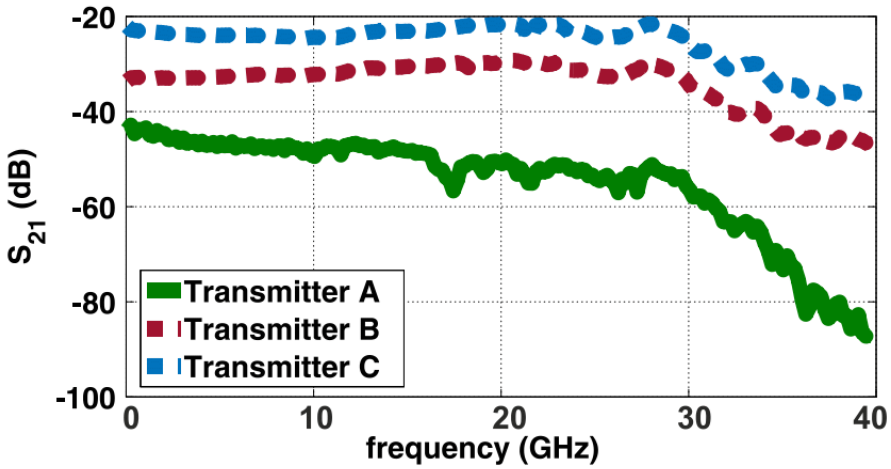

(b) S_{21}

Figure 4.31: Measured S-parameters of transmitters. [56]

Subsequently, the s-parameters of these lasers were evaluated. The impedance matching (S_{11}) and transmission (S_{21}), with the same detection diode, were measured. Figure 4.31 reveals poor impedance matching from 20 GHz for transmitter B, which could impact transmission when interfaced with imperfectly matched components, like the mixer, potentially causing frequency selective dips in the transmission.

Figure 4.31b presents the transmission characteristics of the transmitters. Notably, transmitter A was measured without an input amplifier. Transmitters B and C exhibited almost identical S_{21} waveforms, with the observed drop at higher frequencies likely due to decreased responsivity at the photodetector. This plot also highlights the necessity of compensating for transmission loss with an input amplifier for transmitter A. The transmissions at 25 GHz were −53.9 dB, −32.3 dB and −24.2 dB for transmitters A, B, and C, respectively, with transmitter A including the input amplifier having a transmission of −28.9 dB.

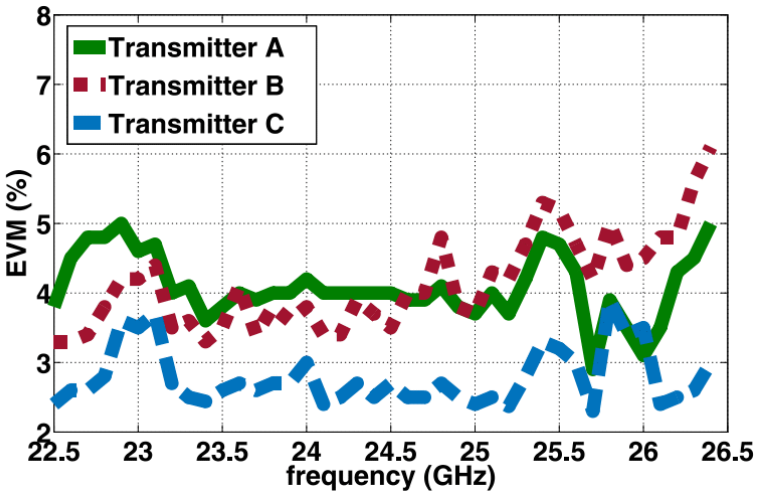

Figure 4.32: Measured EVM in laboratory conditions. [56]

Furthermore, we assessed the transmission quality of modulated signals without an RF link, as shown in Figure 4.32. Transmitter C demonstrated the best EVM performance, likely due to its lowest transmission loss (as seen in Figure 4.31b) and superior background noise characteristics. Transmitter A performed the poorest, attributed to inferior transmission and significant background noise generation (as indicated in 4.30a). However, all transmitters maintained an EVM within the 13.5 % limit for 16-QAM.

4.5.3 Outdoor experiments

Our initial efforts were directed towards evaluating the stability of the overall power transfer. The transmission at 25 GHz was examined using both an RF CW signal and a TM 3.2 modulated signal with a 20 MHz bandwidth. Figure 4.33 show the fluctuations

in received power for the modulated signal. We sampled the power at intervals of 100 ms to capture rapid fluctuations. The results indicate a mean power value of −45.7 dBm with a variance of 1.9 dB. The Figure also includes the power distribution of the signal. This variance aligns with studies [57], [58], which reported variances of 1.1 dB and 3.2 dB for an RF link under similar experimental conditions. For the CW signal, we observed a variance of 2.3 dB in the received power.

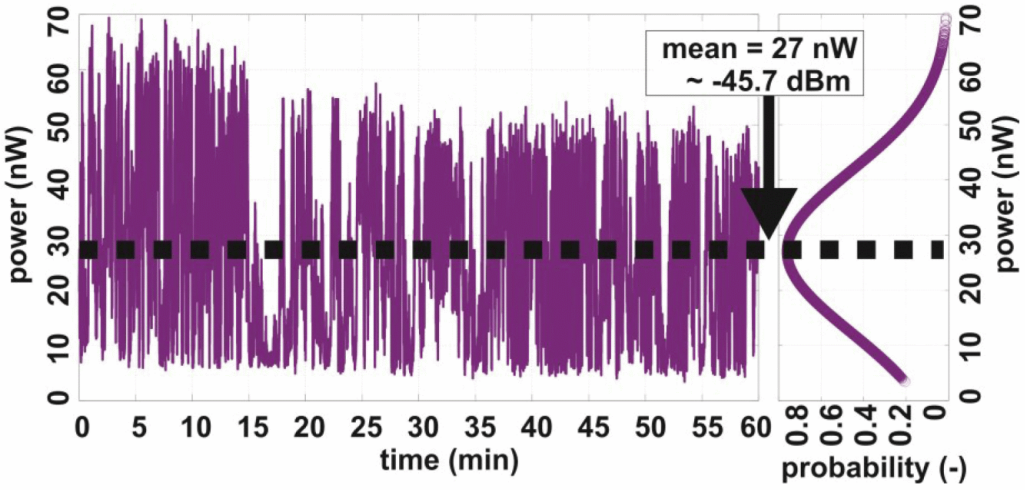

Figure 4.33: Reciever power fluctuations at 25 GHz with 20 MHz signal. [56]

Additionally, these values may be influenced by atmospheric humidity, which ranged from 50 % to 62 % during our measurements, conducted at a temperature of 14 °C. Since no comparable effects were observed in the experiments described in chapter 4.2, it is plausible to attribute these fluctuations to atmospheric phenomena.

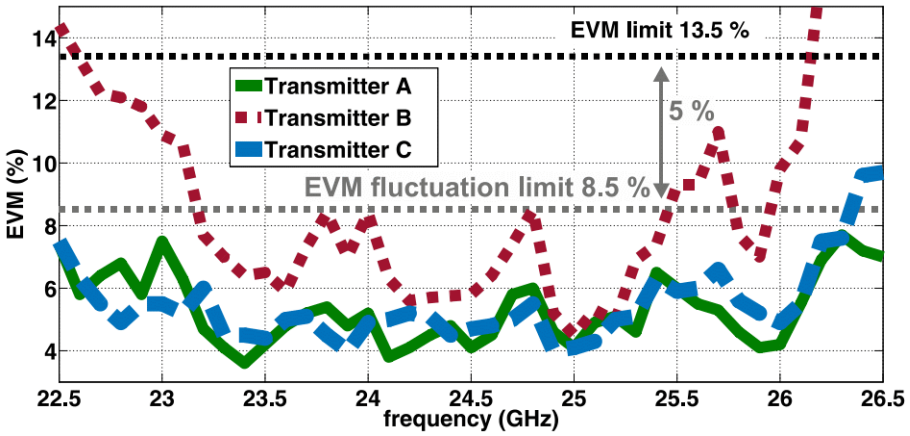

Figure 4.34: Measured EVM in outdoor conditions. [56]

Following the initial confirmation of the system's transmission behavior, we proceeded to assess its performance in transmitting LTE signals using TM 3.2 with a bandwidth of 20 MHz. Figure 4.34 presents the frequency-dependent EVM measurements for each

transmitter. Transmitters A and C consistently achieved EVMs below 6 % throughout the 22.5 GHz to 26.5 GHz band, with the exception of transmitter C in the 26.25 GHz to 26.5 GHz range, where EVM reached 10 %. Nonetheless, the mean EVM for transmitter C remained below the threshold of 13.5 %. In contrast, transmitter B's performance was slightly inferior, remaining within the EVM limit across the 22.75 GHz to 26 GHz band. Despite expectations from indoor measurements for transmitter A to match transmitter B in performance, the latter's lower Extinction Ratio (ER) and poorer impedance matching (S_{11}) may account for its reduced effectiveness.

It is important to emphasize that the EVM values presented are averages. The EVM measurements exhibited fluctuations with power values, with variations up to 5 %. However, the maximum EVM values still provide a sufficient margin for these fluctuations. To accommodate for these variations, a limit value of 8.5 % is also depicted in Figure 4.34.

4.5.4 Discussion

As demonstrated, all transmitters showcased satisfactory transmission parameters. However, transmitter B exhibited a somewhat limited bandwidth, which might be improved by increasing the optical output power of its laser. Generally, lower optical attenuation correlates with enhanced performance. Additionally, precise impedance matching in the electric-to-optical converter is crucial for minimizing standing wave generation between components, thereby reducing frequency selective dips in the transmission.

We also verified the RF transmission path, confirming that even under favorable weather conditions, there are amplitude fluctuations in the range of 2 dB to 3 dB at 25 GHz.

For transmitters with low output power, such as transmitter A employing a DML, integrating an EDFA before the detection diode can be beneficial. This approach was successfully implemented with the aforementioned DML in chapter 4.2, yielding impressive results. In this context, utilizing a DML in this frequency band can be particularly advantageous due to its cost-effectiveness.

These results have been documented and published in [56].

4.6 Experimental comparison of DSB and CS-DSB format modulation

In next experiment, we conducted a comparative analysis of RoF and RoFSO for 5G fronthaul applications. We compared classical Double Sideband (DSB) optical modulation and frequency multiplication modulation. This involved using one MZM set at the zero

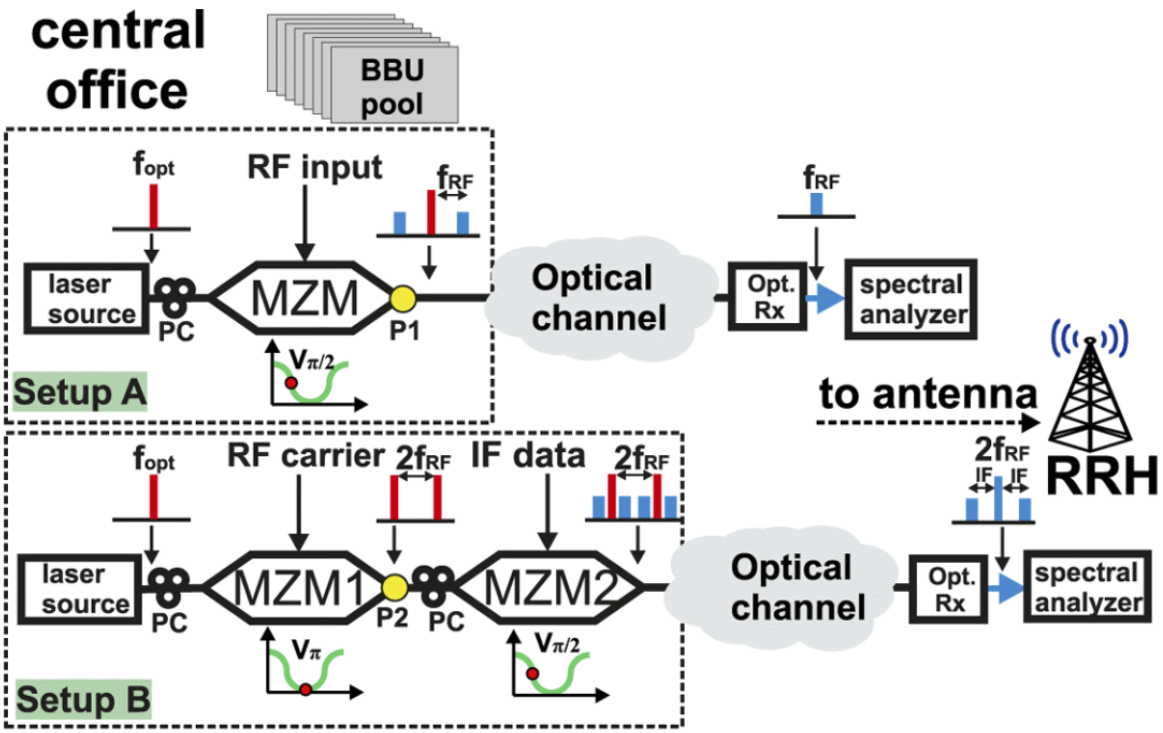

Figure 4.35: Proposed setups A and B for an optical fronthaul network. [61]

transmission point for DSB-SC and second MZM set at the quadrature point for data transmission.

The two systems were evaluated based on EVM, SNR, dynamic range, and phase noise. The tests were carried out at 27 GHz (band n258) and 39 GHz (band n260) [59]. Additionally, for the single DSB setup, measurements were also performed at 3.5 GHz (band n77) [60].

This experiment represented the first assessment of 5G transmission quality in the 27 GHz and 39 GHz bands with bandwidths up to 400 MHz, utilizing a hybrid system comprising SMF, FSO, and RF link. It was also the first to investigate atmospheric turbulence effects on the FSO link for both DSB and CS DSB at 39 GHz within a hybrid SMF and FSO configuration. Additionally, the study included SFDR and phase noise characterizations for both systems.

4.6.1 Experimental setup

Figure 4.35 illustrates the experimental setups used. Setup A is a classic analog microwave photonic system system utilizing direct DSB modulation. The CW laser source (CoBrite DX4) delivers an output power of 16 dBm. The laser feeds into an MZM (Optilab IML-1550-50-PM), set to the quadrature bias point, through a polarization controller. The output optical power of MZM is 7 dBm. A R&S SMW200A vector signal generator serves

as the 5G signal source.

Setup B employs a CoBrite DX4 CW laser as the laser source, connected to an MZM1 (Fujitsu FTM7938EZ/201), set to the zero transfer bias point, via a polarization controller. An R&S SMF100A LO generator, feeding into this MZM, generates half the carrier frequency. The LO frequencies used are 12.5 GHz for the 27 GHz band and 18.5 GHz for the 39 GHz band. A second, low-frequency MZM2 (Covega 10TM 081), biased at the quadrature point, is connected subsequently through another polarization controller to serve as the modulating MZM. An R&S SMW200A vector signal generator is also used here as the 5G signal source, with an output power of −2 dBm.

Both setups utilize the same detection diode (Optilab PD 40) and employ a signal and spectrum analysis (R&S FSW).

In setup B, an EDFA is connected before the detection diode to compensate the low output power of 7 dBm, ensuring comparability with setup A. When an optical channel (SMF and FSO) is included, the EDFA is also incorporated into setup A, compensating for optical channel losses. The EDFA functions as a controlled amplifier, maintaining a consistent output power of 7 dBm.

The optical link comprises a standard 10 km SMF with losses of 2.5 dB and a 4 m FSO link with losses of 6 dB. The FSO link utilizes doublet optical collimators (Thorlabs F810APC-1550) and is situated in a chamber designed to generate atmospheric turbulence.

An optical variable attenuator is incorporated before the EDFA in both setups, allowing for fine-tuning of the input power to the EDFA.

4.6.2 System's SFDR

For measuring the SFDR and IP3, we utilized two tones spaced 1 MHz apart. In setup A, this signal was input directly into the MZM, while in setup B, the signal was fed to the low-frequency MZM2 at an intermediate frequency of 2 GHz. The corresponding measurements are presented in Figure 4.36.

The background noise levels for both setups were measured at −158.0 dBm/Hz for setup A and −156.5 dBm/Hz for setup B. The calculated SFDR values were 88 $\mathrm{dBHz}^{2/3}$ and 89 $\mathrm{dBHz}^{2/3}$ for setup A and setup B, respectively. Despite setup B's marginally poorer background noise, it achieved a slightly better SFDR, largely attributed to its higher S_{21} transmission level, as will be detailed in the subsequent section.

Considering the minimal difference in SFDR values, the two setups can effectively be regarded as equivalent in terms of linearity.

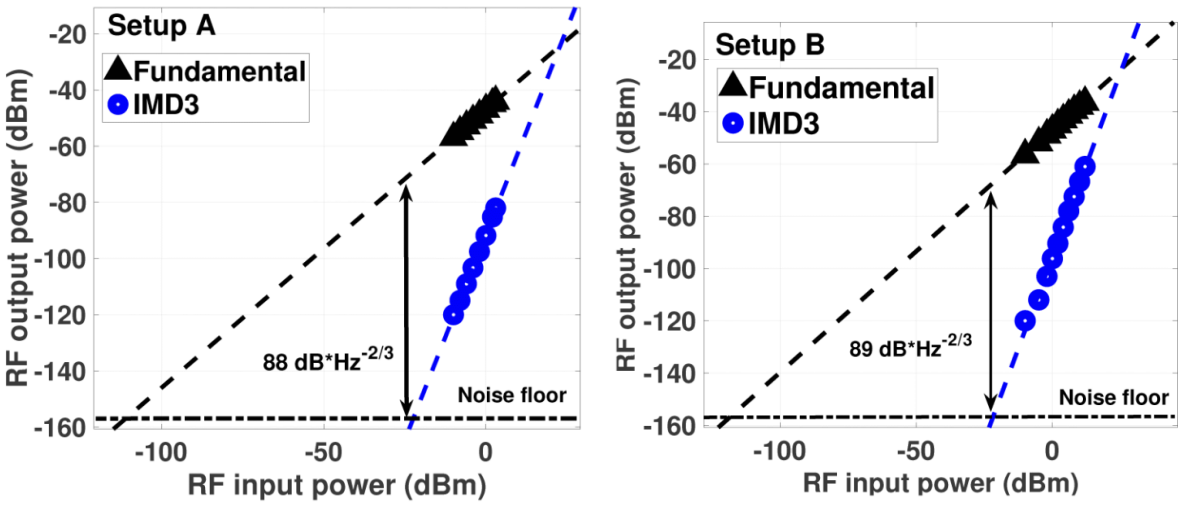

(a) Setup A (b) Setup B

Figure 4.36: Measured dependance of intermodulation products and SFDR and IMD3 of transmitters. [61]

4.6.3 Chromatic dispersion induced fading

To assess the impact of CD, we configured the setup as depicted in Figure 4.35, utilizing only SMF while excluding the FSO component. In setup A, no EDFA was used, while in setup B, the EDFA was adjusted to an output power of 7 dBm. This adjustment ensured uniform optical power conditions for both setups.

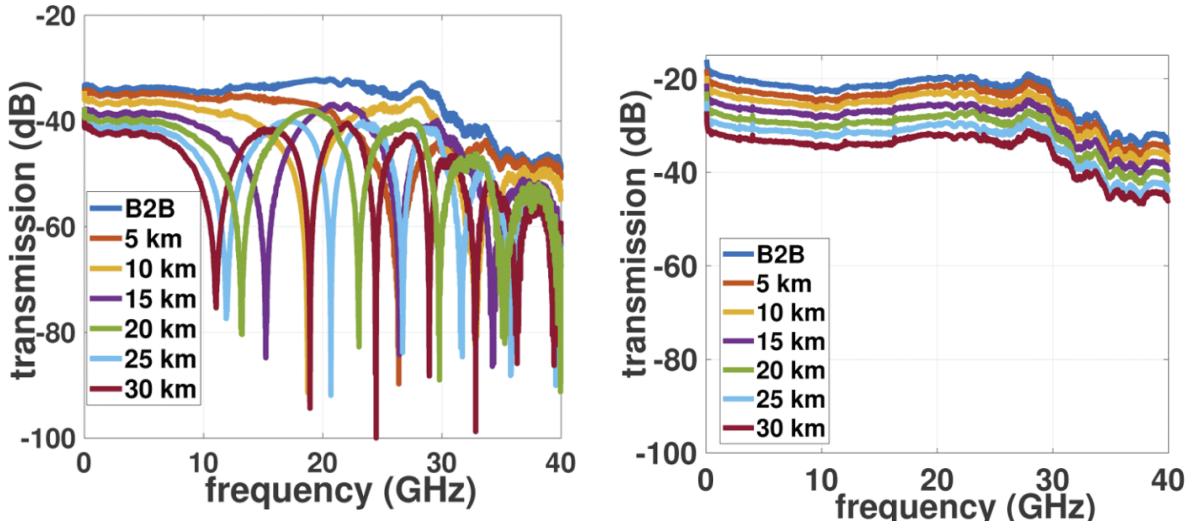

(a) Setup A (b) Setup B

Figure 4.37: Measured transmission response for different SMF lengths. [61]

Using a VNA, we measured the transmission characteristics over varying lengths of SMF, as shown in Figure 4.37. In Figure 4.37a, transmission dips are observed, corresponding to Eq. 1.1. These dips result from the delay (phase shift) between the upper and

lower sidebands of the DSB modulation. At the points with zero detected RF signal, the intensity modulation is fully converted to phase modulation. Conversely, setup B, which employs frequency multiplication, is demonstrated to be immune to CD in Figure 4.37b. Here, transmission differences among curves are attributable to insertion loss from varying SMF lengths. The shape of the transmission curve is given by the frequency response of the detection diode.

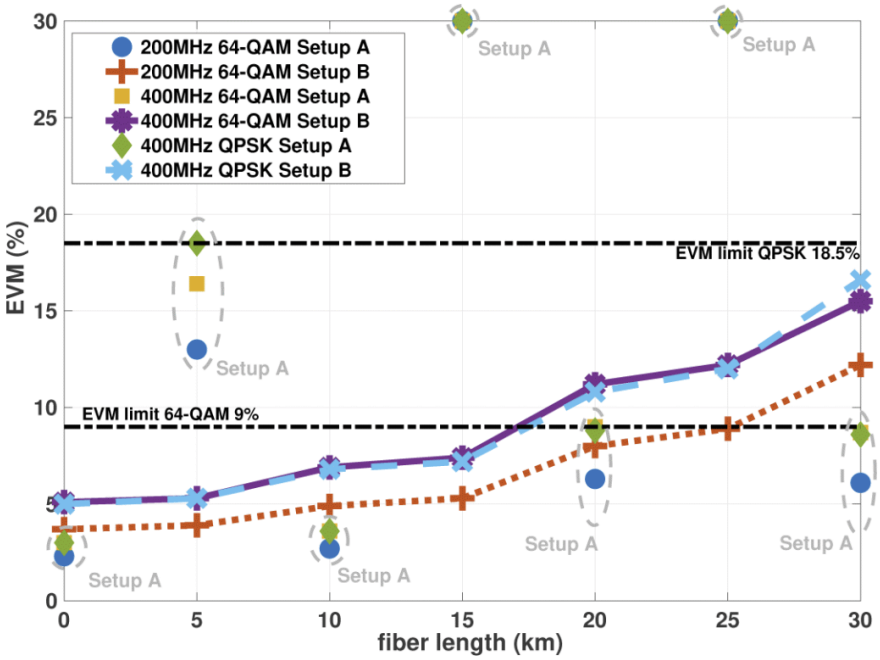

Figure 4.38: Measured EVM vs. SMF lengths. [61]

Subsequently, we conducted tests using a 5G modulated signal with bandwidths of 200 MHz and 400 MHz, incorporating OFDM modulation with either Quadrature Phase Shift Keying (QPSK) or 64-QAM subcarriers at a frequency of 27 GHz. The findings are presented in Figure 4.38. In setup A, the transmission drop results in EVM values exceeding the limits for SMF lengths of 5 km, 15 km and 25 km. Additionally, the graph includes the EVM limits as specified by 3GPP [62]. Notably, for SMF lengths starting from 20 km, the 64-QAM with a 400 MHz bandwidth in setup B fails to meet the EVM threshold. This finding is somewhat counter-intuitive, given that setup B exhibits higher loss. However, this discrepancy is likely due to the elevated noise floor introduced by the EDFA into the optical signal, which is then detected by the diode.

4.6.4 Phase noise

The transmission quality of systems, particularly in the context of OFDM used in LTE and 5G networks, necessitates close attention to the phase noise. This is crucial as phase noise can lead to interference between the subcarriers in the modulated signal. Consequently,

we have conducted phase noise characterization for both setups.

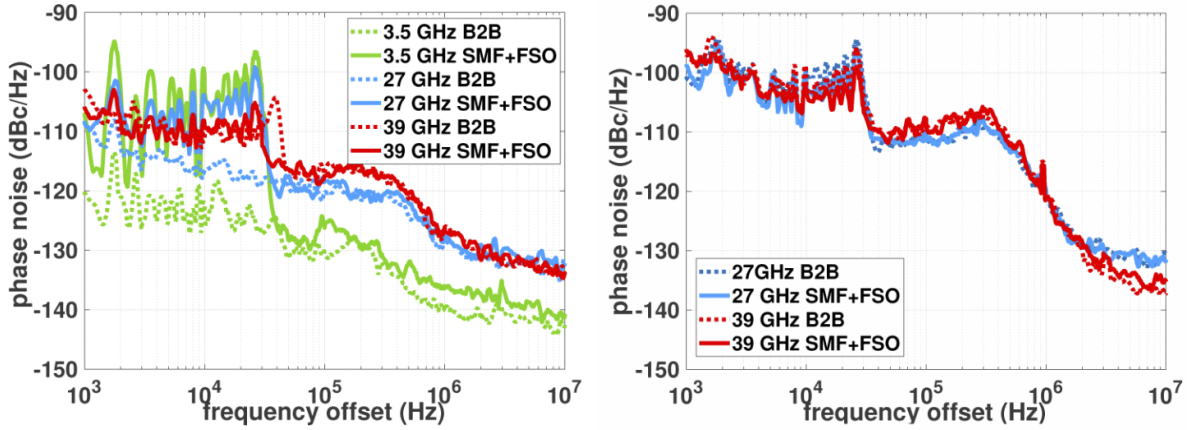

(a) Setup A (b) Setup B with photonic doubling

Figure 4.39: Measured phase noise of proposed setups with 10 km SMF and FSO. [61]

	Setup A			Setup B	
Frequency offset	3.5 GHz (dBc/Hz)	27 GHz (dBc/Hz)	39 GHz (dBc/Hz)	27 GHz (dBc/Hz)	39 GHz (dBc/Hz)
1 kHz	−107	−108	−103	−99	−96
10 kHz	−102	−105	−109	−102	−100
100 kHz	−126	−118	−118	−110	−108
1 MHz	−136	−128	−127	−120	−121
10 MHz	−141	−132	−134	−132	−135

Table 4.6: Measured phase noise of setups with 10 km SMF and FSO link.[61]

Measurements for setup A were taken at 3.5 GHz, 27 GHz and 39 GHz, while for setup B, they were performed at 27 GHz and 39 GHz. These tests included a 10 km SMF and a FSO link. The comparative results at each frequency are presented in Table 4.6. It is evident that setup A demonstrates superior performance with overall lower phase noise in all highlighted frequencies, exhibiting phase noise levels that are 7 dB to 10 dB lower than those of setup B. The observed parameter degradation is attributable to noise propagation from the bias setting of MZM1. Accurate suppression of the carrier frequency is crucial; any deviation from ideal will compromises system performance and bias noise is deviation from ideal. At a 10 MHz offset, the measurements are predominantly limited by the noise floor.

Theoretically, ideal frequency multiplication is expected to worsen phase noise, as per [63]:

$$\Delta P_{\text{phase noise}} = 10 \log \frac{f_2}{f_1} \tag{4.10}$$

where f_1 is input frequency and f_2 is output multiplied frequency.

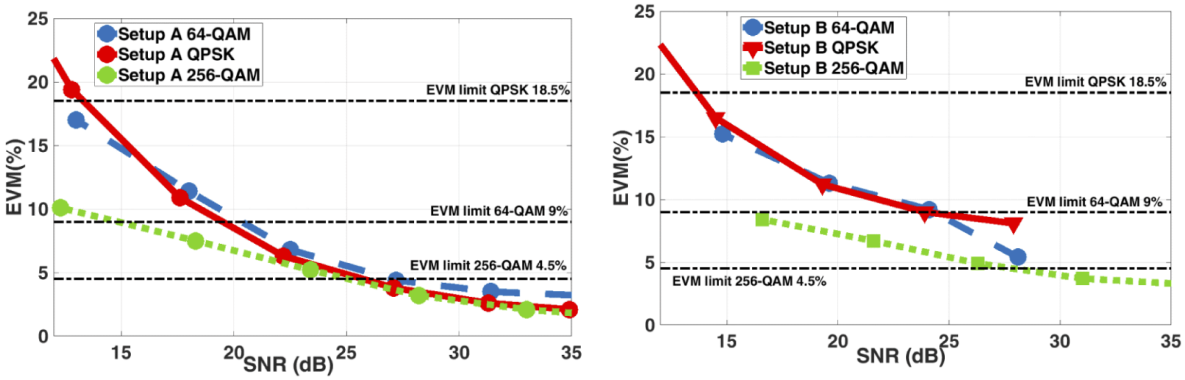

(a) Setup A (b) Setup B

Figure 4.40: EVM versus the SNR at 27 GHz. [61]

This suggests an anticipated deterioration of 8 dB when comparing 3.5 GHz and 27 GHz, and a 1.6 dB difference between 27 GHz and 39 GHz. This pattern is observed in the former scenario but not as pronounced in the latter in the setup A of Table 4.6. The additional phase noise in the second scenario is predominantly evident in the plots of 4.39a.

The phase noise waveforms measured are depicted in the plots of 4.39. Two key observations are made: firstly, the impact of phase noise degradation through the optical path is noticeable up to a frequency offset of 50 kHz. Secondly, setup B demonstrates relative immunity to these effects, showing similar performance in the Back-to-Back (B2B) circuitry and the combined SMF and FSO circuitry.

4.6.5 Full optical channel

We further explored the EVM of the output signal in relation to the SNR for both setups at frequencies of 27 GHz and 39 GHz. The corresponding measurements are depicted in Figure 4.40. Our analysis included a comparison of OFDM signals with 256-QAM in a 100 MHz bandwidth and signals using QPSK and 64-QAM in a 400 MHz bandwidth.

As anticipated, the QPSK and 64-QAM signals exhibited similar dependency profiles. This similarity stems from the differing bandwidths between QPSK and 64-QAM (both 400 MHz) and 256-QAM (100 MHz). The former signals have a 6 dB higher spectral power density, resulting in a better spectral SNR.

Overall, setup A demonstrated superior transmission characteristics, which can be partly attributed to its enhanced phase noise performance.

We next focused on evaluating the behavior of the setups during turbulence in the FSO channel. Turbulence can induce fluctuations in both the amplitude and phase of the measured signal, potentially leading to intersymbol interference. These turbulence tests were conducted in a 4 m long turbulence chamber, where temperature sensors were positioned every 20 cm. The turbulence calculation, based on temperature difference

FSO Length	T0 C_n^2 ($m^{-2/3}$)	T1 C_n^2 ($m^{-2/3}$)
4 m	5.54×10^{-14}	1.15×10^{-11}
100 m	1.52×10^{-16}	3.14×10^{-14}
400 m	7.93×10^{-18}	1.65×10^{-15}

Table 4.7: FSO link atmospheric turbulence refractive index structure parameter.

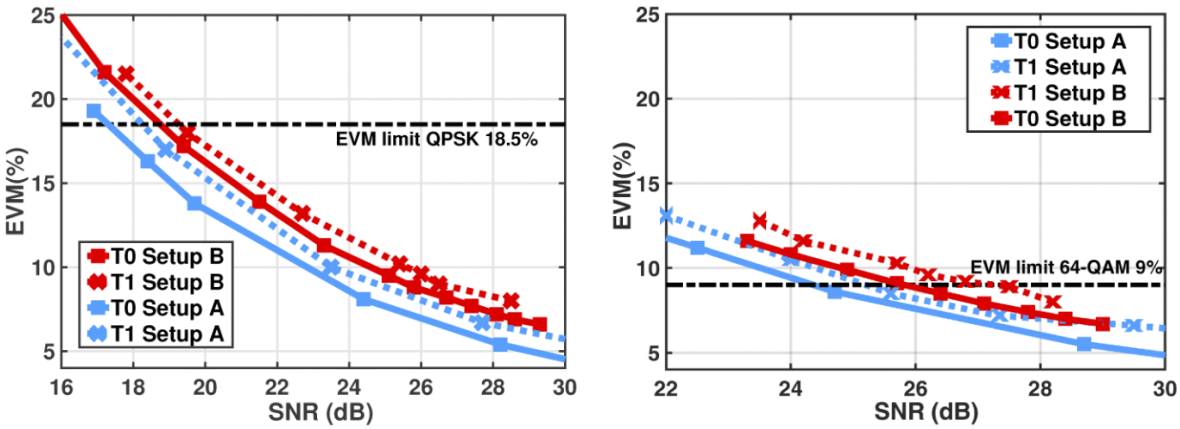

(a) Setup A (b) Setup B

Figure 4.41: EVM versus the SNR with atmospheric turbulence at 27 GHz with bandwidth 400 MHz. [61]

measurements, followed the same methodology outlined in Section 4.2.1.

Measurements were taken under two distinct turbulence levels. The first, denoted as weak turbulence T0, had a refractive index structure parameter $C_n^2 = 5.54 \times 10^{-14}\,\mathrm{m}^{-2/3}$. The second, strong turbulence T1, had a parameter $C_n^2 = 1.15 \times 10^{-11}\,\mathrm{m}^{-2/3}$. These values were further extrapolated using Rytov variance to represent larger distances for standard FSO channels. Table 4.7 presents the recalculated refractive index structure parameters for these extended distances.

The tests were conducted using signals with QPSK (as shown in Figure 4.41a) and 64-QAM (as shown in Figure 4.41b) subcarriers, each within a 400 MHz bandwidth at a 27 GHz carrier frequency. SNR in the link was adjusted using a variable optical attenuator. In setup A, SNRs up to 36 dB were achieved (not depicted in the plot due to x-axis truncation). On average, setup A demonstrated 3 % and 1 % lower EVM for QPSK and 64-QAM, respectively, compared to setup B. An average increase in EVM at a given SNR of 2 % for QPSK and 1 % for 64-QAM was observed.

The same tests were replicated for both setups at 39 GHz, utilizing signals with QPSK subcarriers in a 400 MHz bandwidth. The results indicated a nearly linear decrease in EVM with increasing perturbations. For setup B, required by 0.5 dB higher SNR to achieve the EVM limit of 18.5 %. In contrast,setup A experienced a higher degradation

of 1 dB in immunity against turbulences.

4.6.6 Discussion

The two setups showcased were rigorously evaluated for their compatibility with 5G network requirements, with the outcomes of these evaluations detailed in [61]. At the 39 GHz frequency, both setups exhibited comparable performance in terms of the EVM parameter. However, when evaluating the cost-effectiveness of MZMs within high frequency bands alongside with the efficiency of signal generation, setup B emerges as potentially more advantageous. This preference arises despite the incorporation of two modulators, attributed to the employment of an MZM at lower frequencies by modulating the signal at a lower frequency. This advantage is attributed to its ability to generate a signal at a lower IF and mixing with LO on corresponding to half the carrier frequency, while the mixing process occurring optically at the detection diode. This design also confers immunity to CD. Additionally Figure 4.37a illustrates that setup A is only effective for certain combinations of carrier frequencies and optical fiber lengths due to CD.

One drawback of setup B is the necessity to use an EDFA to compensate for the attenuation caused by the two MZMs, ensuring adequate received optical power at the detection diode and, subsequently, at the RF output. As discussed in previous chapters (specifically Chapter 4.3), incorporating an EDFA before the detection diode-particularly with an optical filter-enhances the system's immunity to loss in both the SMF and FSO.

Additionally, it is feasible to employ a DSB-SC circuit with two MZMs for frequency multiplication higher than 2x. This approach can significantly simplify the RF component on the transmit side.

4.7 Experimental analysis of 5G NR transmission on FR2-2.

This chapter provides an experimental validation of the implementation of 5G NR transmission in the FR 2-2 frequency band, specifically at 62 GHz. The employed frequency doubling scheme offers significant advantages, including reduced requirements for LO generation and the capability for direct modulation from a low IF. This approach is designed to replicate a realistic signal distribution scenario from a central BBU pool to individual RRH. The system configuration incorporates an EDFA to counterbalance power losses in the optical segment, aiming to maintain consistent optical power at the detection diode.

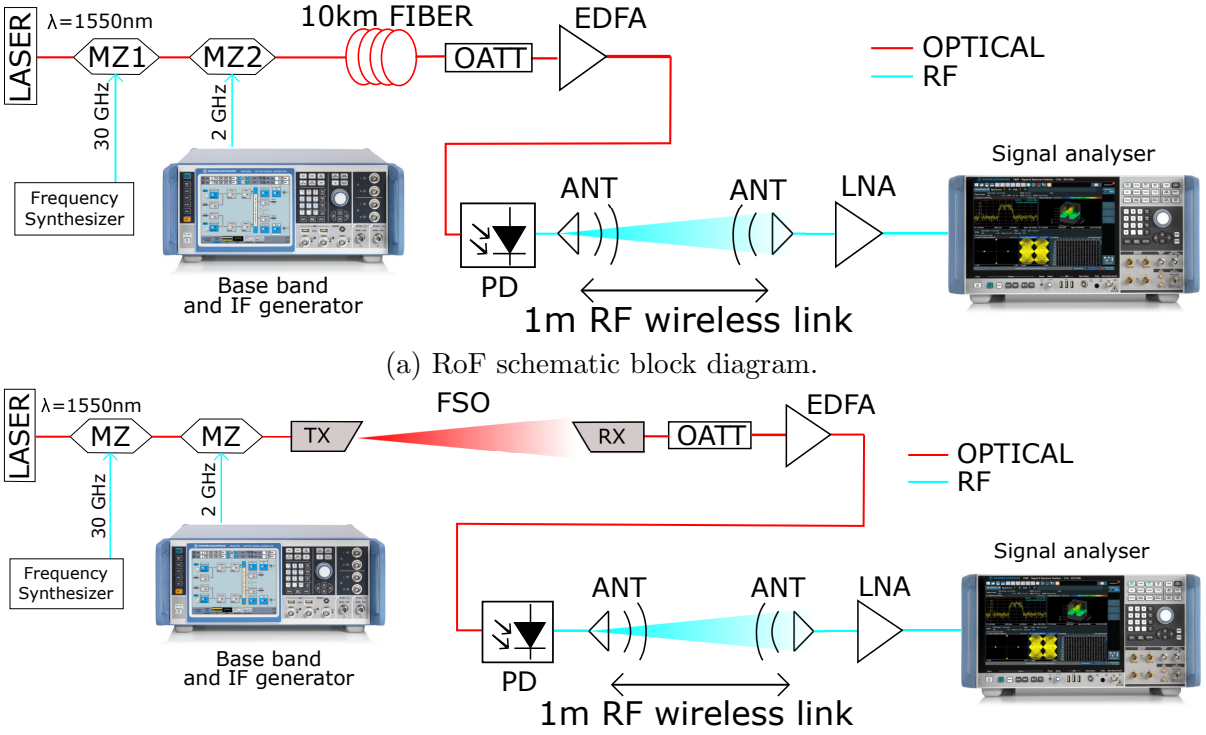

(a) RoF schematic block diagram.

(b) RoF with FSO schematic block diagram.

Figure 4.42: 5G system block diagrams. [64]

4.7.1 Experimental setup

For the implementation of a practical data transmission link, we employed a 5G NR signal generated by a vector signal generator (R&S SMW200A) operating at an IF of 2 GHz. Notably, the low-frequency signal utilized can be readily generated in the contemporary landscape with a high-speed DAC. The selected bandwidth aligns with signals designated for FR2-2 in 5G, specifically the mmW frequency bands. [33]

In our setup, an optical DSB-SC transmission approach was employed. This involved using a MZM (Fujitsu FTM7938EZ/201) biased at the minimum transmission point to generate the desired double-frequency modulated signal in the electrical domain. Additionally, another low-frequency linearly biased MZM (Covega 10TM 081) was utilized for data modulation.

The input signal to the first MZM was a single tone at 30 GHz with a power of 13.6 dBm to generate a 60 GHz RF carrier. The optical source used was a CW laser (ID-Photonics TLCoBrite DX4) with an optical power of 16 dBm at the standard wavelength of 1550 nm. The bias voltage of the first MZM was set to 2.4 V to achieve optical carrier suppression.

While an RF single tone generator (R&S SMF100A) was employed for modulating the first MZM, the second MZM was modulated by the 5G NR signal with an IF of 2 GHz. The second MZM was biased at the quadrature point with a bias of 4 V, while the electrical input mean power and the peak envelope power (PEP) were 7 dBm and 19 dBm,

respectively, nearing the maximum output power of the vector signal generator, approximately 25 dBm. However, in order to maintain high linearity without adversely affecting the measured EVM and degrading the overall system performance, we have configured the maximum output power to 20 dBm. This configuration represented the transmitting part of the experimental system, yielding an output optical power of −6.8 dBm.

The frequency doubling was subsequently achieved through the beating of the optical sidebands at the photodetector (PD, FINISAR XPDV3120).

For the B2B configuration, we conducted measurements on the proposed system without the inclusion of any additional channel components, such as SMF, FSO, or antenna links to have reference measurements. Subsequently, our optical fronthaul performance tests were categorized into three distinct scenarios. The first scenario (Figure 4.42a) illustrates a RoF setup comprising 10 km of SMF and an RF wireless link. In the second scenario (Figure 4.42b), labeled as RoFSO, a 4 m FSO channel replaced the SMF. The FSO link was implemented using two optical collimators (OC, Thorlabs F810APC-1550). It's noteworthy that the distance covered by these collimators can be extended, for example, up to 100 m, making it suitable for applications between buildings, as demonstrated in [65]. The third setup combines elements (SMF and FSO) from both of the previously mentioned configurations.

To simulate the SNR by introducing additional attenuation in the optical path, a variable OATT (OZ Optics DA-100) was employed.

Prior to optical detection, an amplifier is positioned to counteract optical attenuation. This amplification process is facilitated by an EDFA (Keopsys CEFA-C-HG-SM-50-B130-FAFA) functioning under an automatic gain control regime. This setup guarantees a uniform output optical power of 8.2 dBm, subsequently directed to a PD for direct detection.

All three tested scenarios utilized a 1 m long indoor RF wireless link to simulate the free-space path between a RRH and user equipment. This link was established through a pair of waveguide pyramidal horn antennas (ANT, RFspin H-A90-W25). The total loss of the 62 GHz seamless radio link, accounting for the antennas' gains, was 18 dB. It's worth noting that while horn antennas may not be suitable for practical use in user equipment, in this experimental setup, they effectively emulate the overall gain and directional characteristics expected in a practical antenna array implementation.

To amplify the received signal to an adequate power level, a LNA (SAGE SBL-5037033550-VFVF-S1) with 35 dB gain and a reasonable 5 dB noise figure at 62 GHz frequency was positioned after the receiving antenna. Signal performance at target frequency was evaluated using a spectrum and signal analyzer (R&S FSW40) equipped with a harmonic mixer (R&S FS-Z90). The harmonic mixer's LO and IF were carefully chosen

Laser wavelength	1550 nm
Laser output power	16 dBm
MZM2 output power	−8.2 dBm
EDFA output power	8.2 dBm
FSO loss	7.2 dB
FSO length	4 m
SMF loss	3.1 dB
SMF length	4 km
PD responsibility	0.6 A/W
RFGEN1 output power	13.6 dBm
RFGEN2 output power	7 dBm
FSL	68 dB
Antenna gain	16 dB
LNA gain	35 dB

Table 4.8: System parameters. [64]

to ensure a clean output signal without interference from other mixed products.

4.7.2 System characterization

In the initial phase, we fine-tuned the RoF system (Figure 4.42a) to optimize its overall performance. To evaluate the system, we employed the predefined 5G NR test model, specifically NR-FR2-TM3.1, operating in a time division duplex mode with a subcarrier spacing of 120 kHz. This finely tuned system forms the basis for all subsequent measurements.

Given the stringent requirements for 5G NR signal performance, we next measured the phase noise characteristics at 62 GHz. Three systems - RoF, RoFSO, and a hybrid RoF-FSO configuration - were evaluated as illustrated in Figs. 4.42.

Initially, the B2B configuration was characterized for frequency offsets up to 10 MHz. Subsequently, each optical channel configuration was examined, both with and without an additional 1 m antenna link. To discern the influence of the measurement setup, we also assessed the phase noise characteristic of the signal generator itself. The results of these measurements are presented in Figure 4.43.

The generator's phase noise profile, depicted in red and demonstrating the lowest phase noise across all configurations, recorded a magnitude better than −80 dBc/Hz at a 100 Hz offset. Notably, the phase noise levels for the RoF, RoFSO, and hybrid systems were remarkably similar, hovering around −75 dBc/Hz at the 100 Hz offset. Furthermore, comparisons between B2B, optical channel (SMF/FSO), and the complete link incorporating a 1 m antenna channel revealed negligible differences in their phase noise profiles.

This implies that at 62 GHz, the phase noise performance is largely unaffected by the

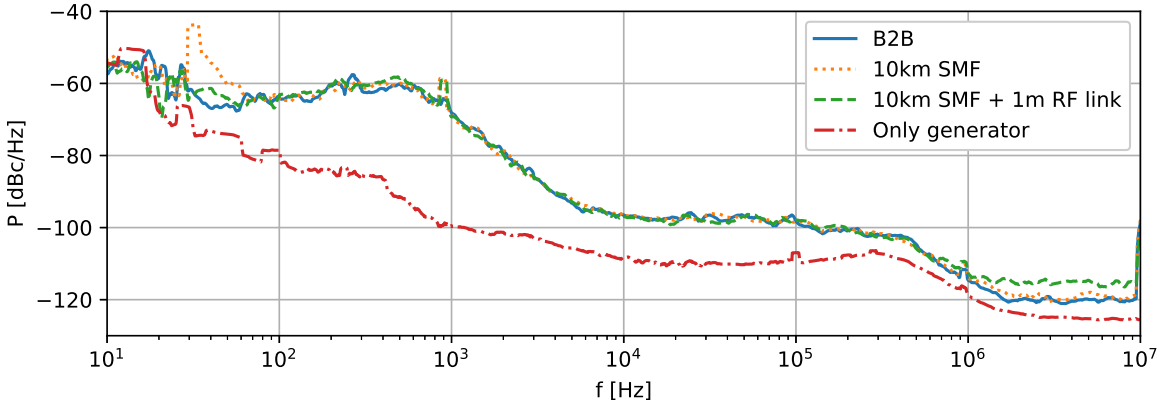

(a) SMF channel.

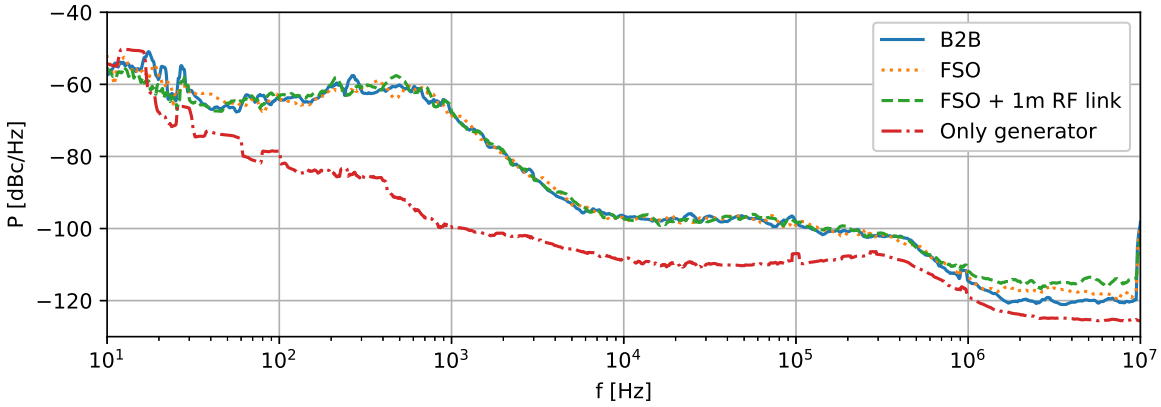

(b) FSO channel.

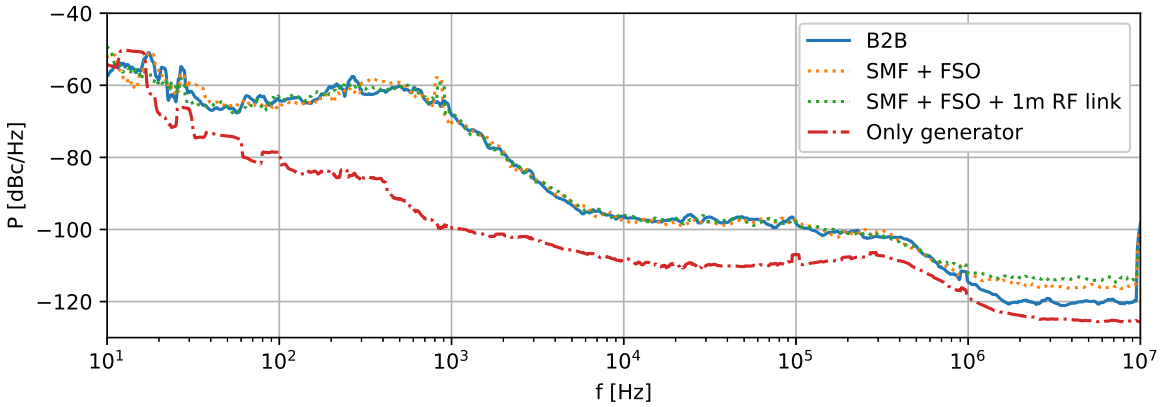

(c) Hybrid SMF and FSO channel

Figure 4.43: Phase noise of proposed 5G setups at 62 GHz.

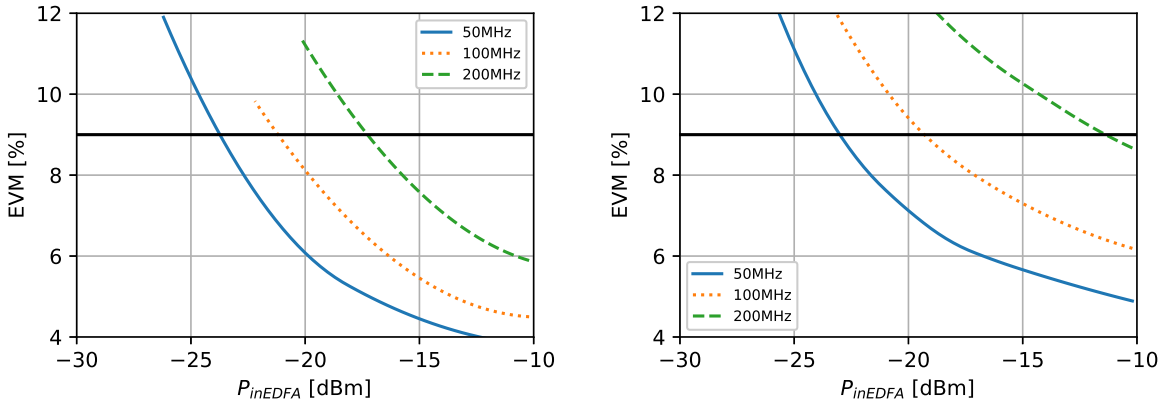

(a) RoF system

(b) RoF system with 1 m indoor RF link

Figure 4.44: Dependencies of EVM on input power to EDFA for RoF system with 10 km of SMF.

type of optical channel - whether SMF or FSO - and that the inclusion of a seamless antenna link does not significantly degrade performance for offsets up to 1 MHz. The most noticeable divergence occurs in the range of 1 MHz to 10 MHz, predominantly due to the noise floor of the system.

4.7.3 System performance

The system underwent testing across various bandwidths, specifically 50 MHz, 100 MHz and 200 MHz. The selected test model, compliant with [33], is designed for evaluating both output power dynamics at maximum power with all 64-QAM subcarriers allocated and signal quality and EVM for 64-QAM modulation at maximum power.

Subsequently, EVM as a function of the input optical power to the EDFA was investigated (Figure 4.44) for the RoF system, employing 10 km of SMF with and without an antenna link. The EVM was measured for a range of input power levels set by OATT in 1 dB steps, simulating power losses in the optical setup. It is observed that there is a margin of more than 5 dB for additional loss in the optical path for the fiber setup. However, for the fiber setup with an antenna link, this margin is insufficient to meet the EVM limit for 200 MHz bandwidth. Other bandwidths maintain sufficient power margin to meet the 9 % EVM limit for 64-QAM. The EVM requirements [33] vary with the modulation format used, such as 18.5 % for QPSK, suggesting that employing adaptive modulation could maintain error-free communication at reduced speeds.

Furthermore, we examined the system's linear response across a spectrum of modulated signal bandwidths. This exploration is critical for generalizing the system's performance across a wide range of signal bandwidths. We utilized EVM measurements as a key metric, examining its correlation with the SNR of the received signal. The SNR,

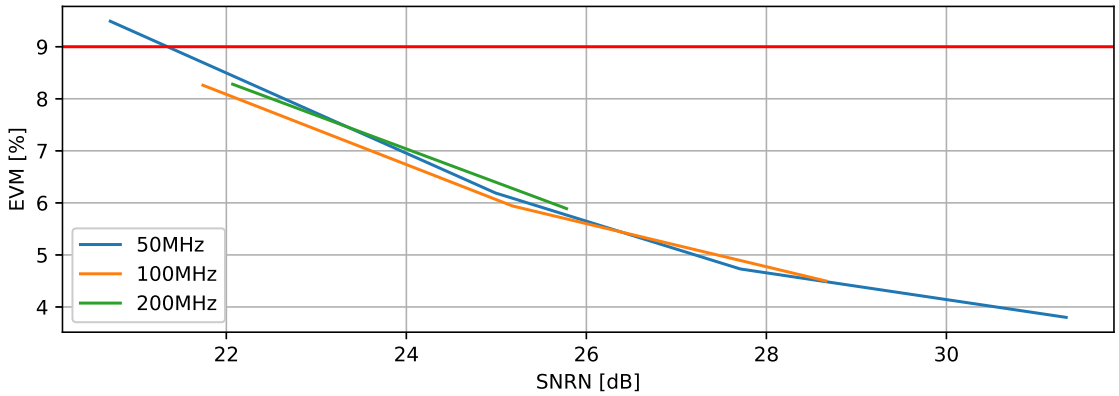

Figure 4.45: Achieved EVM for different bandwidths depending on SNRN for RoF setup.

defined as the ratio of the received power of the modulated signal to the noise power in the channel, is a fundamental parameter in evaluating the system's linearity. To achieve a normalized comparison across different bandwidths, we normalized the SNR with the bandwidth of the modulated signals:

$$\mathrm{SNRN} = \frac{P_{\mathrm{RX}}}{N_{\mathrm{RX}}\mathrm{BW}} \tag{4.11}$$

Here, P_{RX} represents the received power at the signal analyzer, N_{RX} denotes the measured noise spectral density in the channel, and BW is the bandwidth of the measured signal. Figure 4.45 presents a comprehensive comparison of EVM against SNRN for the SMF setup. In this configuration, the SNR was adjusted using an optical attenuator. The observations indicate that the bandwidth, in isolation, exerts a minimal impact on the overall transmission quality. It is the reduction in the spectral power density, particularly for signals with larger bandwidths, that proves to be a critical factor affecting transmission performance. This underscores the importance of considering spectral power density alongside bandwidth when assessing the efficiency and effectiveness of signal transmission.

The RoFSO system, as depicted in Figure 4.46, exhibited generally poorer performance compared to the RoF setup, primarily due to the lower input power to the EDFA. This reduction in power is attributed to the losses incurred in the FSO link, resulting in an input power of $-14.3\,\mathrm{dBm}$ for the FSO system, as opposed to $-10.2\,\mathrm{dBm}$ in the RoF setup. It is noteworthy that the loss for the 4 m FSO link was measured at 7.2 dB.

In the FSO configuration without the antenna link, the margin of input power to the EDFA varied depending on the modulation and bandwidth: 4 dB for 64-QAM with 200 MHz, 7 dB for 64-QAM with 100 MHz, and 9 dB for 64-QAM with 50 MHz. Upon incorporating the antenna link, the system maintained a sufficient margin of 5 dB for 64-QAM with 100 MHz and 9 dB for 64-QAM with 50 MHz. These margins could potentially accommodate future extensions of the FSO link.

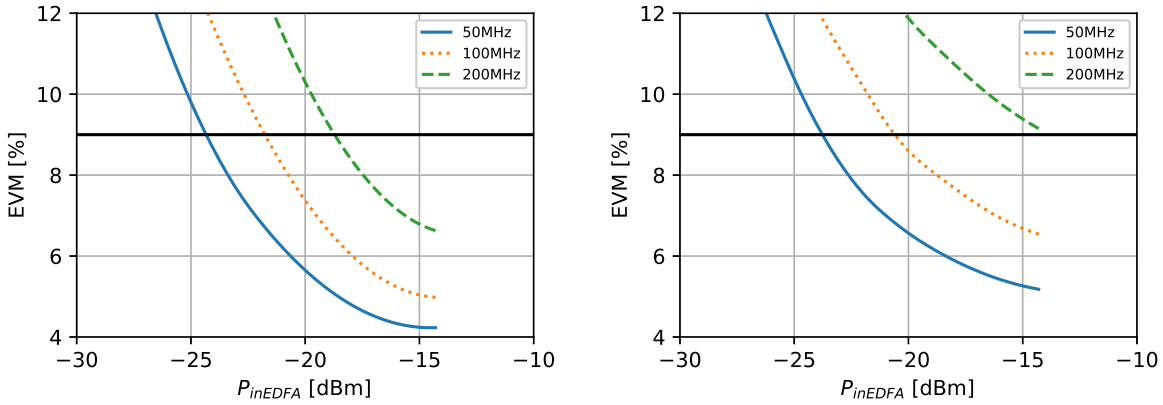

(a) FSO system

(b) FSO system with 1 m indoor RF link

Figure 4.46: Dependencies of EVM on input power to EDFA for FSO system.

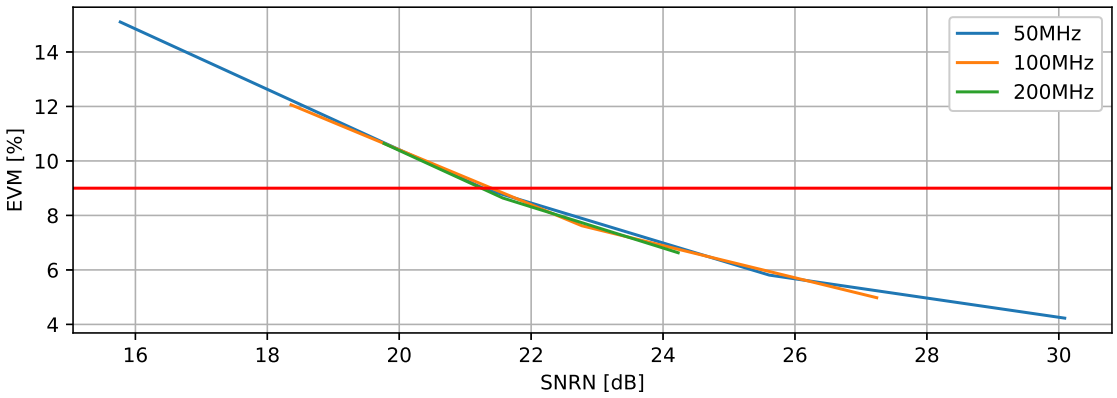

Figure 4.47: Achieved EVM for different bandwidths depending on SNRN for RoFSO setup.

Consistent with the approach taken in the previous case, we conducted an analysis utilizing normalized SNR. The outcome of this analysis, illustrated in Figure 4.47, corroborates our earlier conclusion: the bandwidth of the transmitted signal does not fundamentally affect the performance of this system in terms of SNR. This finding emphasizes that the system's efficiency is not critically dependent on the signal bandwidth.

Figure 4.48 displays the EVM as a function of input power to the EDFA for a hybrid system comprising both SMF and FSO. The input power to the EDFA in this setup is −16.5 dBm, noticeably lower than in previous scenarios. This reduction in power is evident in the transmission challenges encountered for the test signal with a 200 MHz bandwidth, which only meets the EVM limit in scenarios without RF coupling.

In scenarios without an RF link (as shown in Figure 4.48a), the dynamic range of input power required to meet the EVM standards varies with the signal bandwidth. For a 50 MHz bandwidth signal, the dynamic range is 8 dB, while for 100 MHz, it is 5 dB. However, for a signal with 200 MHz bandwidth, the dynamic range narrows to just 1 dB,

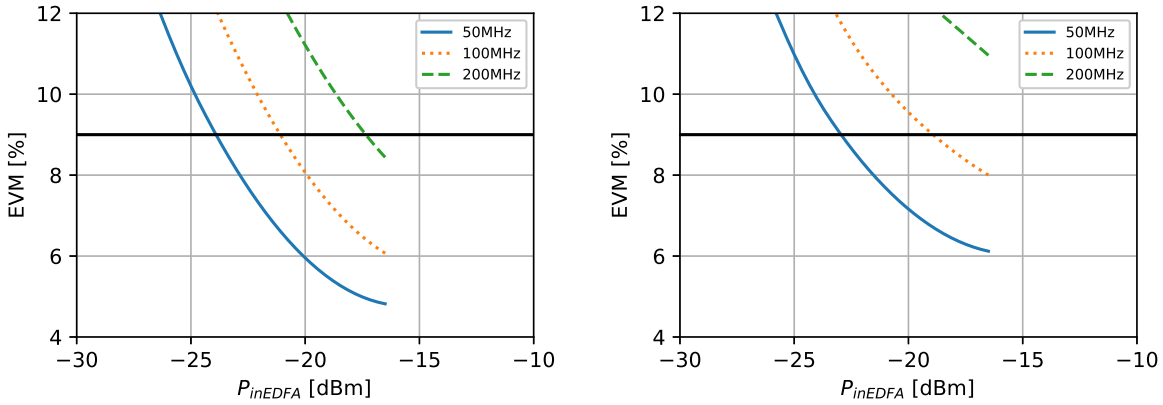

(a) Hybrid system (b) Hybrid system with 1 m indoor RF link

Figure 4.48: Dependencies of EVM on input power to EDFA for FSO system.

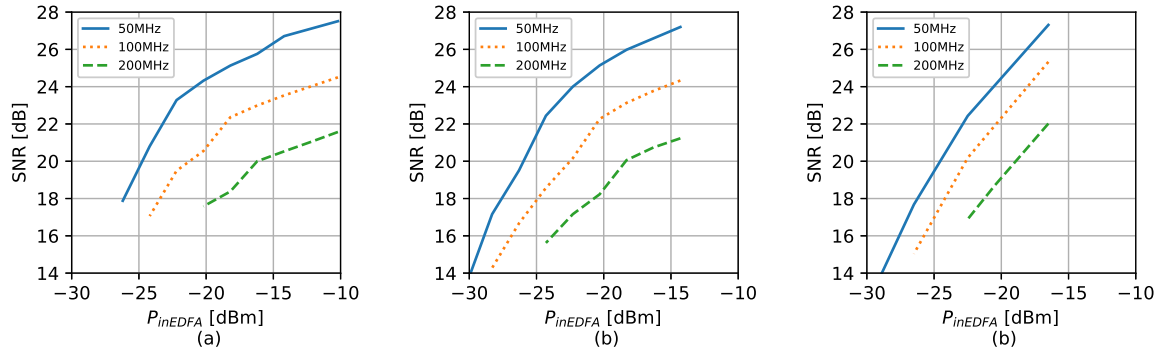

(a) RoF system (b) FSO system (c) Hybrid system

Figure 4.49: Dependencies of SNR at the signal analyzer and input power to EDFA.

leaving an insufficient margin for any additional system requirements. This limitation becomes more pronounced with the inclusion of an RF link, where a 200 MHz bandwidth signal fails to stay within the 9 % EVM threshold.

Figure 4.49 presents the dependency of electrical SNR levels on the input power to the EDFA for various signal bandwidths. The highest SNR values observed are 27.5 dB for the 50 MHz bandwidth with RoF, 27.2 dB with FSO, and 27.1 dB for the hybrid system incorporating an antenna link. While the RoF system yields higher SNR values, the results indicate that to achieve a comparable SNR level as in the RoF setup, the FSO setup requires slightly lower optical input power to the EDFA. Specifically, an input power of −20 dBm to the EDFA is sufficient to attain an SNR of 22.5 dB in the FSO setup, compared to approximately −18 dBm required in the RoF setup to reach the same SNR level.

Generally, the dependency of EDFA input power on the final signal SNR exhibits greater variability in the RoF setup. This is primarily attributed to the higher input

power to the low-noise EDFA in the RoF system (−10.2 dBm) versus FSO (−14.3 dBm), resulting in different linearity characteristics between the two setups.

4.7.4 Discussion

A significant advantage of the photonically frequency-doubling technique used in our proposed transmission scheme, as highlighted in Chapter 4.6,is its immunity to chromatic dispersion, a common issue in double sideband transmission regimes. Furthermore, after the mmW signal generation, the phase noise does not experience further degradation. Our system has demonstrated robust performance in both RoF and FSO scenarios, even under conditions of low input optical power to the EDFA. However, an increase in bandwidth imposes an additional penalty on EVM, primarily because the EDFA output power remains constant regardless of input power variations. As bandwidth expands, the power spectral density in the channel diminishes, leading to a flattening of noise generation by the EDFA, as elaborated in [66]. This issue poses a challenge for the system's dynamic range, necessitating either i) an increase in EDFA output power, which may not always be feasible, or ii) a dynamic adaptation of bandwidth based on the available SNR. Further insights into the theory of spectral efficiency and SNR in analog RoF systems are discussed in [67].

Given the efficacy of analog RoF and FSO technologies in the high-frequency mmW range, specifically around the 60 GHz band known for high free space losses, their optimal application is foreseen in small- and femto-cell deployments. These cells are ideally suited for environments like offices and shopping centers, where a high concentration of users necessitates high-speed connections over short distances.

A portion of the findings from this experimental demonstration has been documented and published in [64].

4.8 Bidirectional 60/25 GHz heterogeneous fronthaul link

In this experimental demonstration, we proposed a system transmitting 16/64-QAM LTE OFDM signals utilizing mmW frequencies at 60 GHz and 25 GHz for DL and UL, respectively, over a diverse optical fronthaul infrastructure. Both communication links employ a DML, facilitating a cost-effective, full-duplex system design. Whereas direct modulation of mmW signal is applied to the DML for UL, the DL, operating at 60 GHz, exploits an photonical up-conversion by using additional MZM. The experimental configuration comprises a 10 km SMF, a 100 m FSO long channel, and a 2 m wireless RF link. The

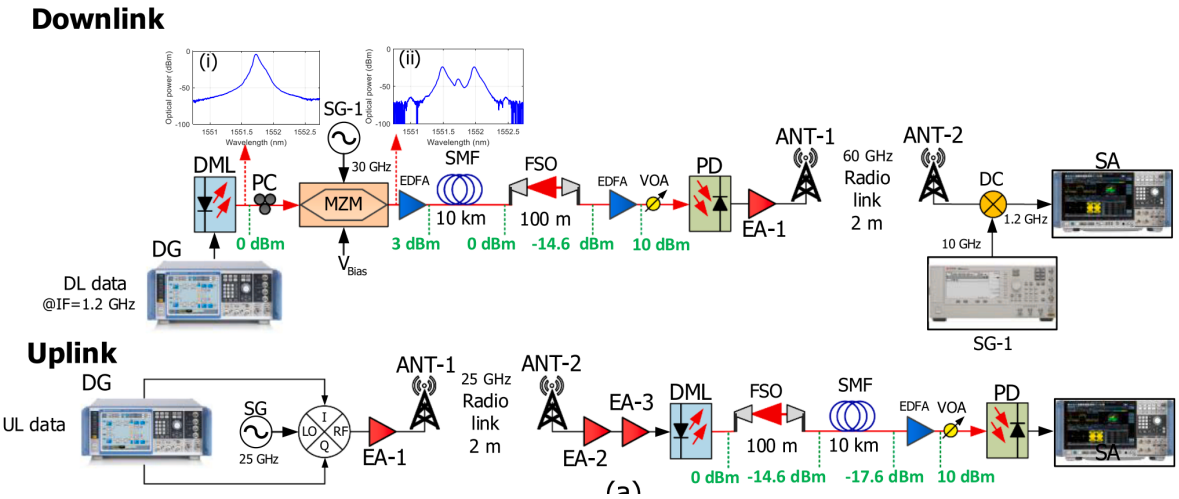

Figure 4.50: Experimental setup of bidirectional 60/25 GHzheterogeneous fronthaul link. [68]

measured EVM serves as the principal metric for assessing transmission quality.

4.9 Experimental setups

The experimental configuration is divided into two parts: the DL path, operating at a frequency of 60 GHz (specifically $f_{\mathrm{LO}} + f_{\mathrm{IF}} = 61.2\,\mathrm{GHz}$) leveraging photonic mixing with frequency doubling techniques, and the UL path, functioning at 25 GHz utilizing a DML for signal generation, is directly fed by the mmW signal. This setup is illustrated in Figure 4.50.

In the DL path, the signal generation employs a DML, specifically a monolithically-integrated laser with passive feedback, driven by an IF signal of 1.2 GHz produced by an R&S SMW200A vector signal generator. To achieve frequency up-conversion of the DML's output, we utilize a mmW photonic generation technique that incorporates carrier-suppressed external modulation. This process is implemented by a MZM (Optilab IML-1550-50-PM), with the LO frequency set to $f_{\mathrm{LO}} = 60\,\mathrm{GHz}/2$ and biased to suppress the optical carrier. Subsequent signal amplification is carried out using an EDFA to compensate losses incurred, particularly from MZM biased in minimum transmission point.

For the optical transmission, the system integrates 10 km of SMF and a 100 m FSO link. The FSO component utilizes two collimators (Thorlabs F810APC-1550) and exhibits insertion losses of 14.6 dB over 100 m distance. Given the indoor setup of the FSO link, environmental factors are considered negligible. Post-FSO transmission, an EDFA is used for loss compensation, with a variable OATT to fine-tune the received optical power (RoP). A photodetector (Finisar XPDV3120) is connected after the attenuator. The photodetector enables signal beating and upconversion of the modulated IF signal. The

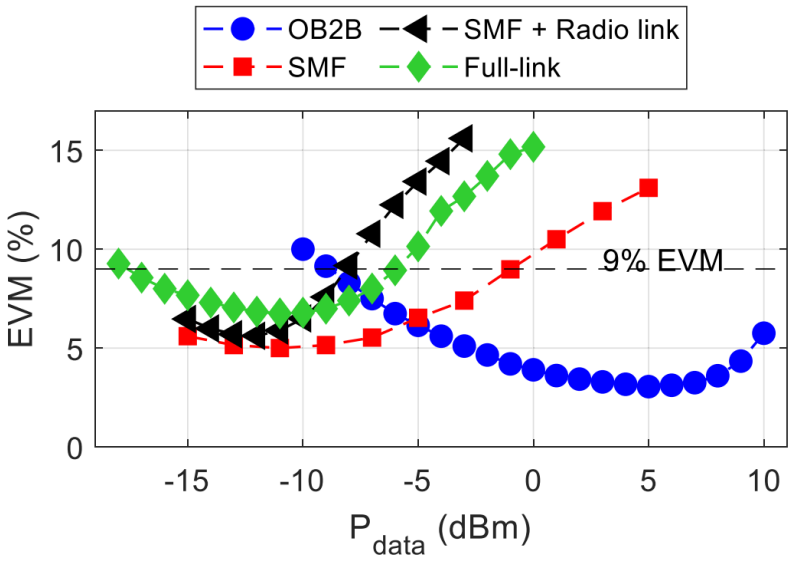

Figure 4.51: DL signal power optimization. [68]

upconverted signal is amplified using an EA-1 amplifier (SAGE SBL-5037033550-VFVF-S1), and wireless transmission occurs over a 2 m RF link utilizing horn antennas (RF spin, H-A90-W25). The signal is finally applied into a signal analyzer (R&S FSW) for evaluation, with a downconverter (R&S FS-Z90) employed prior to analysis.

The UL signal generation starts in baseband, utilizing the SMW200A for signal generation, followed by electrical upconversion in an IQ modulator. Post-modulation, signal amplification is done by an EA-1 amplifier (Wisewave AGP-33142325-01) and wireless transmission occurs through a double-ridged horn antenna (RF spin DRH40) over a 2 m wireless link. The received signal undergoing further amplification through a cascade of two amplifiers (MITEQ AMF-4F-2604000-40-10P) before being fed into the same DML used in the DL path. It is worth to mention that both the DL and UL have been tested separately. The modulated signal then goes through the FSO and SMF links, with an EDFA and a variable OATT employed to compensate for losses and adjust the optical power at the photodetector, which performs the opto-electronic conversion. The converted signal is analyzed directly by the R&S FSW signal analyzer.

The test signal utilized for radio transmission performance measurement, the LTE TM3.1 described in [53], incorporating a 20 MHz bandwidth at 1.2 GHz IF. This test model employs OFDM with 64-QAM modulation.

Optimization efforts for the IF signal power in the DL setup (Figure 4.51) revealed the optimal power settings for optical back-to-back (OB2B) is 5 dBm, and for the combined SMF and FSO segments is −12 dBm. These findings underscore the influence of dispersion effects on the DML's output signal, necessitating specific power adjustments to mitigate signal distortion across different transmission scenarios, including the SMF followed by

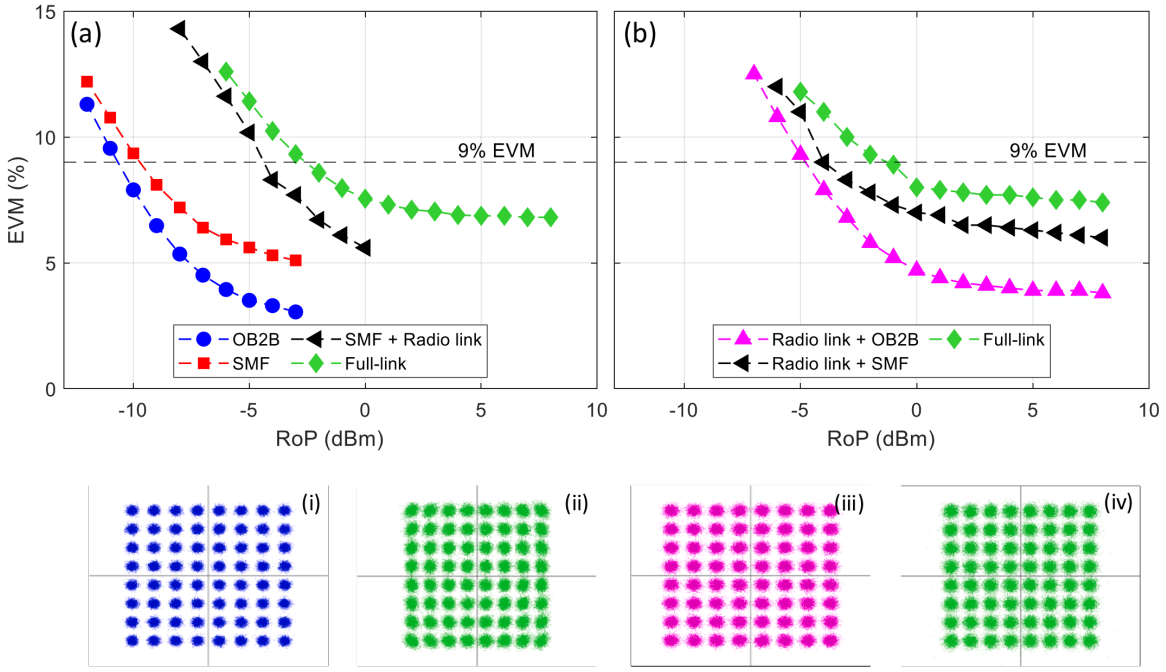

Figure 4.52: EVM vs. RoP for 64-QAM with different configuration in both links: (a) 61.2 GHz DL (b) 25 GHz UL. [68]

the radio sub-link and the comprehensive link setup.

A similar optimization process was undertaken for the UL direction, involving a sweep of the LO power to characterize its impact on the signal quality. The selected LO power was determined to be 18 dBm, chosen to maximize the RoP.

4.10 Experimental transmission results

Performance evaluations for both the DL and UL were conducted by evaluation the EVM as a function of the RoP for a 64-QAM signal in the 60 GHz band (DL) and the 25 GHz band (UL). Notably, the DL OB2B scenario necessitated different input power levels (P_{data}) compared to other DL configurations, specifically 5 dBm versus −12 dBm, which has been adopted for all other scenarios. The EVM's dependence on the RoP, controlled by the optical losses introduced through the variable OATT, for both DL and UL configurations using 64-QAM modulation, is illustrated in Figure 4.52. As illustrated in Figure 4.52(a), the DL EVM improves (decreases) with increasing RoP. For the configurations combining SMF with radio links and the comprehensive full-link configuration, a power penalty of 5 dB and 7 dB, respectively, was observed at the 9 % EVM threshold, which is in line with 3GPP standards for LTE [53]. This indicates that maintaining acceptable transmission quality for the full-link scenario necessitates a minimum RoP of −2.7 dBm.

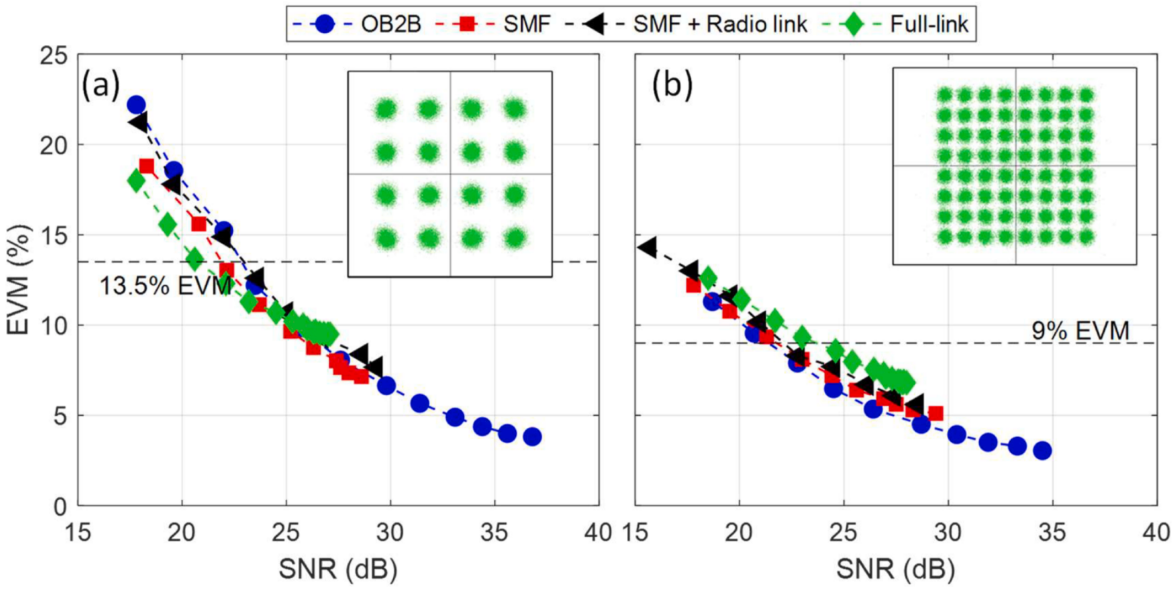

Figure 4.53: EVM vs. SNR measured for DL with different modulation formats: (a) 16-QAM, (b) 64-QAM. [68]

Figure 4.52(b) presents the EVM's RoP dependency in the UL, where introducing SMF and full-link configurations incurs penalties of 1.5 dB and 3 dB, respectively, compared to the OB2B scenario. To maintain EVM below the 9 % threshold for full-link operations, a minimum RoP of −1 dBm is required.

Further characterization for the DL was conducted using both 64-QAM and 16-QAM modulation formats (LTE test model TM 3.2) with 20 MHz bandwidth, measuring the EVM's dependence on the SNR of the electrically recovered signal. This measurement provides insights into the DL transmission system's distortions. Unlike previous tests that only utilized 64-QAM, this assessment included 16-QAM to explore performance under different modulation schemes. As depicted in Figure 4.53(a), the 16-QAM configuration exhibits a consistent performance across all scenarios, requiring a minimum SNR of 22 dB to achieve EVM levels below the 13.5 % limit for full link configuration (as specified in [53]).

Figure 4.53(b) showcases the EVM performance for 64-QAM signal transmission, where the full-link characterization reveals a maximum penalty of 2.5 dB compared to the OB2B link at the 9 % EVM threshold. An SNR of at least 23.7 dB is necessary to ensure the integrity of 64-QAM signal transmission at 61 GHz across all DL scenarios.

Figure 4.53 also includes constellation diagrams both corresponding to an SNR of 28 dB, offering a visual representation of the signal integrity under these conditions.

4.11 Discussion

This work presents an experimental demonstration of LTE M-QAM signal transmission across both 60 GHz and 25 GHz bands for DL and UL paths, traversing through a hybrid network consisting of 10 km of SMF, a 100 m FSO link, and a 2 m seamless radio link. These findings are detailed in [68]. To adhere to the stringent 9 % EVM criterion for 64-QAM signals with a 20 MHz bandwidth, it was established that the minimum necessary received optical powers are −2.7 dBm for the DL and −1 dBm for the UL, respectively.

A significant focus of this study is on the advantages offered by the DML in both the DL and UL configurations. For the DL, the DML presents a cost-effective approach that notably simplifies the overall system architecture by integrating the laser and modulator into a singular unit. Remarkably, for transmissions at 61.2 GHz, a DML with a relatively low bandwidth i.e. less than 2 GHz would be sufficient. This setup benefits from the frequency doubling feature inherent in photonic signal generation techniques, necessitating only a 30 GHz LO frequency to the MZM for achieving of 61 GHz transmission. This characteristic leads to a substantial downsizing in the equipment prerequisites. Moreover, through experimental validation, it has been demonstrated that a 100 m FSO link can serve efficiently as the “last mile” connectivity solution in bidirectional optical fronthaul networks, specifically within mmW bands.

Chapter 5

Conclusion of the thesis

5.1 Contribution of the thesis

This doctoral thesis presents a novel perspective on the utilization of RoF, RoFSO, and their combinations within the C-RAN for 5G networks in the FR2-1 and FR2-2 frequency bands. It demonstrates, optimizes and methodically tests setups for transmission between BBU pools and RRHs, exploring the overall transmission performances of these setups.

The outputs from this doctoral work have been published in [5], [50], [51], [54], [56], [61], [65], [69] for the FR2-1 band. Furthermore, the work transitioned into the FR2-2 band, culminating in two publications [64], [68]. Especially in the case of [64], where I used 5G NR with bandwidth up to 200 MHz. Throughout this work, a lot of effort was made to optimally configure and characterize the proposed setups, to derive recommendations for deployment in 5G and emerging 6G networks. This has resulted in a significant number of outputs with a considerable citation impact.

The findings of this thesis contribute to a substantial simplification of RRHs. This leads to the ultimate goal where the mmW signal will be routed over the RoF with a minimum of additional circuits in the RRH. Especially since we have achieved bidirectional transmission, as published in [68]. Furthermore, this work extended the knowledge in RoFSO and the effect of atmospheric turbulence on FSO transmission of LTE and 5G NR.

Additionally, the work delved into the verification of optically controlled beamforming based on the optical delay lines and the effect of CD. The outcomes from this verification were published in [46], [48] and have been further utilized in projects [70] and a utility sample [71].

5.2 Conclusions for further development

The majority of the experiments were conducted approximately at a frequency of 25 GHz within the FR2-1 band. Therefore, it would be beneficial to more explore the FR2-2 band, utilizing both external modulation techniques and DML with usage of OFM. Due to continuous advances in research, directly modulated lasers with bandwidths up to 108 GHz are already being achieved [16], offering new development opportunities for implementation of fronthaul networks. Additionally, there is also potential for the linearization of MZM [72], presenting a path for future development.

Bibliography

[1] J. Lee, E. Tejedor, K. Ranta-aho, H. Wang, K.-T. Lee, E. Semaan, E. Mohyeldin, J. Song, C. Bergljung, and S. Jung, "Spectrum for 5G: Global status, challenges, and enabling technologies", *IEEE Communications Magazine*, vol. 56, no. 3, pp. 12–18, 2018. DOI: 10.1109/mcom.2018.1700818. [Online]. Available: https://ieeexplore.ieee.org/document/8316581.

[2] M. A. Habibi, M. Nasimi, B. Han, and H. D. Schotten, "A comprehensive survey of RAN architectures toward 5G mobile communication system", *IEEE Access*, vol. 7, pp. 70 371–70 421, 2019. DOI: 10.1109/ACCESS.2019.2919657.

[3] G. O. Perez, D. L. Lopez, and J. A. Hernandez, "5G new radio fronthaul network design for eCPRI-IEEE 802.1cm and extreme latency percentiles", *IEEE Access*, vol. 7, pp. 82 218–82 230, 2019. DOI: 10.1109/access.2019.2923020. [Online]. Available: https://ieeexplore.ieee.org/document/8736787.

[4] H. Schmuck, "Comparison of optical millimetre-wave system concepts with regard to chromatic dispersion", *Electronics Letters*, vol. 31, no. 21, pp. 1848–1849, Oct. 1995, ISSN: 1350-911X. DOI: 10.1049/el:19951281.

[5] J. Bohata, J. Spacil, D.-N. Nguyen, S. Zvanovec, L. Vallejo, and B. Ortega, "Radio over 50 km fiber and joint 80 m FSO/wireless links using photonic frequency doubling for 5G", in *2019 IEEE Global Communications Conference (GLOBECOM)*, IEEE, Dec. 2019. DOI: 10.1109/globecom38437.2019.9013212. [Online]. Available: https://doi.org/10.1109/GLOBECOM38437.2019.9013212.

[6] C. Lim, C. Ranaweera, A. Nirmalathas, Y. Tao, S. Edirisinghe, L. Wosinska, and T. Song, "Optical X-haul for 5G /6G: Design and deployment standpoint", in *2022 IEEE Future Networks World Forum (FNWF)*, 2022, pp. 507–512. DOI: 10.1109/FNWF55208.2022.00095.

[7] C. Lanzani, G. Kardaras, and D. Boppana, *Remote radio heads and the evolution towards 4G networks*, English, Whitepaper, 2009.

[8] B. H. Jung, H. Leem, and D. K. Sung, "Modeling of power consumption for macro-, micro-, and RRH-based base station architectures", in *2014 IEEE 79th Vehicular Technology Conference (VTC Spring)*, IEEE, May 2014. DOI: 10.1109/vtcspring.2014.7022990. [Online]. Available: https://ieeexplore.ieee.org/document/7022990.

[9] I. P. Kaminow and T. L. Koch, Eds., *Optical fiber telecommunications IIIB* (Optics and Photonics). San Diego, Calif: Academic Press, 1997, 515 pp., Includes bibliographical references and index.

[10] G. P. Agrawal, *Fiber-optic communication systems* (@Wiley series in microwave and optical engineering), 3. ed. New York, NY: Wiley-Interscience, 2002, ISBN: 9786610556304.

[11] Andrews, C. Larry, Phillips, and L. Ronald, *Laser Beam Propagation through Random Media, Second Edition*. SPIE–The International Society for Optical Engineering, 2005, p. 808, ISBN: 9781510643703.

[12] G. Meslener, "Chromatic dispersion induced distortion of modulated monochromatic light employing direct detection", *IEEE Journal of Quantum Electronics*, vol. 20, no. 10, pp. 1208–1216, 1984, ISSN: 1558-1713. DOI: 10.1109/JQE.1984.1072286.

[13] Y. Li, Q. Xie, M. El-Hajjar, and L. Hanzo, *Analogue radio over fiber for next-generation RAN: Challenges and opportunities*, 2021. DOI: 10.48550/ARXIV.2111.13851. [Online]. Available: https://arxiv.org/abs/2111.13851.

[14] R. Samy, H.-C. Yang, T. Rakia, and M.-S. Alouini, "Space-air-ground FSO networks for high-throughput satellite communications", *IEEE Communications Magazine*, vol. 60, no. 12, pp. 82–87, Dec. 2022, ISSN: 1558-1896. DOI: 10.1109/mcom.002.2200018. [Online]. Available: https://ieeexplore.ieee.org/document/9887916.

[15] M. Uysal, *Optical Wireless Communications, An Emerging Technology* (Signals and Communication Technology Ser.), C. Capsoni, Z. Ghassemlooy, A. Boucouvalas, and E. Udvary, Eds. Cham: Springer International Publishing AG, 2016, 1639 pp., Description based on publisher supplied metadata and other sources., ISBN: 9783319302010.

[16] S. Yamaoka, N.-P. Diamantopoulos, H. Nishi, *et al.*, "Directly modulated membrane lasers with 108 GHz bandwidth on a high-thermal-conductivity silicon carbide substrate", *Nature Photonics*, vol. 15, no. 1, pp. 28–35, Oct. 2020, ISSN: 1749-4893. DOI: 10.1038/s41566-020-00700-y. [Online]. Available: https://doi.org/10.1038/s41566-020-00700-y.

[17] P. C. D. Hobbs, *Building electro-optical systems, Making it all work* (Wiley series in pure and applied optics), 2nd ed. Hoboken, N.J: Wiley, 2009, 1799 pp., Includes bibliographical references and index, ISBN: 9780470402290.

[18] B. Wilson, Z. Ghassemlooy, and I. Darwazeh, Eds., *Analogue optical fibre communications* (IEE telecommunications series 32). London: Institution of Electrical Engineers, 1995, 319 pp., ISBN: 0852968329.

[19] L. J. Lembo, F. D. Alvarez, D. Lo, C. A. Tu, P. H. Wisseman, C. Zmudzinski, and J. C. Brock, "Optical electroabsorption modulators for wideband, linear, low-insertion-loss photonic links", in *Photonic Device Engineering for Dual-Use Applications*, A. R. Pirich, Ed., SPIE, Jun. 1995. DOI: 10.1117/12.212725. [Online]. Available: https://doi.org/10.1117/12.212725.

[20] M. Aoki, M. Suzuki, H. Sano, T. Kawano, T. Ido, T. Taniwatari, K. Uomi, and A. Takai, "InGaAs/InGaAsP MQW electroabsorption modulator integrated with a DFB laser fabricated by band-gap energy control selective area MOCVD", *IEEE Journal of Quantum Electronics*, vol. 29, no. 6, pp. 2088–2096, 1993, ISSN: 1558-1713. DOI: 10.1109/3.234473. [Online]. Available: https://ieeexplore.ieee.org/document/234473.

[21] F. Valdez, V. Mere, X. Wang, *et al.*, "110 GHz, 110 mW hybrid silicon-lithium niobate mach-zehnder modulator", *Scientific Reports*, vol. 12, no. 1, Nov. 2022, ISSN: 2045-2322. DOI: 10.1038/s41598-022-23403-6. [Online]. Available: https://www.nature.com/articles/s41598-022-23403-6.

[22] R. Mears, L. Reekie, I. Jauncey, and D. Payne, "Low-noise erbium-doped fibre amplifier operating at 1.54 um", *Electronics Letters*, vol. 23, no. 19, p. 1026, 1987, ISSN: 0013-5194. DOI: 10.1049/el:19870719. [Online]. Available: https://doi.org/10.1049/el:19870719.

[23] E. Desurvire, J. R. Simpson, and P. C. Becker, "High-gain erbium-doped traveling-wave fiber amplifier", *Optics Letters*, vol. 12, no. 11, p. 888, Nov. 1987, ISSN: 1539-4794. DOI: 10.1364/ol.12.000888. [Online]. Available: https://doi.org/10.1364/OL.12.000888.

[24] J. S. Tan, "Noise performance of erbium-doped fiber amplifiers with forward and reverse plumbing", Accessed: 2024-01-24, Ph.D. dissertation, Massachusetts Institute of Technology, 2000. [Online]. Available: http://oastats.mit.edu/bitstream/handle/1721.1/86506/46894894-MIT.pdf.

[25] K. S. Abedin, T. F. Taunay, M. Fishteyn, M. F. Yan, B. Zhu, J. M. Fini, E. M. Monberg, F. Dimarcello, and P. Wisk, "Amplification and noise properties of an erbium-doped multicore fiber amplifier", *Optics Express*, vol. 19, no. 17, p. 16 715, Aug. 2011, ISSN: 1094-4087. DOI: 10.1364/oe.19.016715. [Online]. Available: https://doi.org/10.1364/OE.19.016715.

[26] K.-P. Ho, S.-K. Liaw, and C. Lin, "Efficient photonic mixer with frequency doubling", *IEEE Photonics Technology Letters*, vol. 9, no. 4, pp. 511–513, Apr. 1997, ISSN: 1941-0174. DOI: 10.1109/68.559405. [Online]. Available: https://ieeexplore.ieee.org/document/559405.

[27] R. T. Logan and R. D. Bynum, "Millimeter wave optical link/frequency converter system", Tracor Aerospace Electronics Systems, Inc., Final Technical Report, Jul. 1998.

[28] G. Qi, J. Yao, J. Seregelyi, S. Paquet, C. Belisle, X. Zhang, K. Wu, and R. Kashyap, "Phase-noise analysis of optically generated millimeter-wave signals with external optical modulation techniques", *Journal of Lightwave Technology*, vol. 24, no. 12, pp. 4861–4875, Dec. 2006, ISSN: 0733-8724. DOI: 10.1109/jlt.2006.884990. [Online]. Available: https://ieeexplore.ieee.org/document/4063427.

[29] R. Wang, H. Hu, and X. Yang, "Potentials and challenges of c-ran supporting multi-rats toward 5g mobile networks", *IEEE Access*, vol. 2, pp. 1187–1195, 2014. DOI: 10.1109/ACCESS.2014.2360555.

[30] J. G. Andrews, S. Buzzi, W. Choi, S. V. Hanly, A. Lozano, A. C. K. Soong, and J. C. Zhang, "What will 5g be?", *IEEE Journal on Selected Areas in Communications*, vol. 32, no. 6, pp. 1065–1082, 2014. DOI: 10.1109/JSAC.2014.2328098.

[31] P. T. Dat, A. Kanno, and T. Kawanishi, "Radio-on-radio-over-fiber: Efficient fronthauling for small cells and moving cells", *IEEE Wireless Communications*, vol. 22, no. 5, pp. 67–75, 2015. DOI: 10.1109/MWC.2015.7306539.

[32] M. Sung, J. Kim, E.-S. Kim, S.-H. Cho, Y.-J. Won, B.-C. Lim, S.-Y. Pyun, H. Lee, J. K. Lee, and J. H. Lee, "RoF-based radio access network for 5G mobile communication systems in 28 GHz millimeter-wave", *Journal of Lightwave Technology*, vol. 38, no. 2, pp. 409–420, 2020. DOI: 10.1109/JLT.2019.2942636.

[33] "ETSI TS 138 141-2 V15.1.0 (2019-04) - 5G; NR; Base Station (BS) conformance testing Part 2: Radiated conformance testing (3GPP TS 38.141-2 version 15.1.0 Release 15)", European Telecommunications Standards Institute (ETSI), Standard, Apr. 2019.

[34] E.-S. Kim, M. Sung, J. H. Lee, J. K. Lee, S.-H. Cho, and J. Kim, "Coverage extension of indoor 5G network using rof-based distributed antenna system", *IEEE Access*, vol. 8, pp. 194 992–194 999, 2020. DOI: 10.1109/ACCESS.2020.3033592.

[35] G. Pandey, A. Choudhary, and A. Dixit, "Radio over fiber based fronthaul for next-generation 5G networks", in *2020 22nd International Conference on Transparent Optical Networks (ICTON)*, 2020, pp. 1–4. DOI: 10.1109/ICTON51198.2020.9203207.

[36] X. Li and J. Yu, "Photonics-aided 32-gb/s wireless signal transmission over 1 km at k-band", *IEEE Photonics Technology Letters*, vol. 29, no. 13, pp. 1120–1123, 2017. DOI: 10.1109/LPT.2017.2706696.

[37] H. Zhang, L. Cai, S. Xie, K. Zhang, X. Wu, and Z. Dong, "A novel radio-over-fiber system based on carrier suppressed frequency eightfold millimeter wave generation", *IEEE Photonics Journal*, vol. 9, no. 5, pp. 1–6, 2017. DOI: 10.1109/JPHOT.2017.2731620.

[38] X. Li, Y. Xu, and J. Yu, "Over 100-gb/s v-band single-carrier pdm-64qam fiber-wireless-integration system", *IEEE Photonics Journal*, vol. 8, no. 5, pp. 1–7, 2016. DOI: 10.1109/JPHOT.2016.2615101.

[39] M. Safak, *Digital Communications* (New York Academy of Sciences Series), 1st ed. Newark: John Wiley & Sons, Incorporated, 2017, 1909 pp., Description based on publisher supplied metadata and other sources., ISBN: 9781119091264.

[40] L. Zhao, L. Xiong, M. Liao, S. Liu, and X. Yu, "Qpsk vector millimeter-wave signal generation based on odd times of frequency without precoding", *IEEE Photonics Journal*, vol. 10, no. 6, pp. 1–9, 2018. DOI: 10.1109/JPHOT.2018.2878873.

[41] A. O. Mufutau, F. P. Guiomar, M. A. Fernandes, A. Lorences-Riesgo, A. Oliveira, and P. P. Monteiro, "Demonstration of a hybrid optical fiber–wireless 5G fronthaul coexisting with end-to-end 4G networks", *Journal of Optical Communications and Networking*, vol. 12, no. 3, p. 72, Feb. 2020, ISSN: 1943-0639. DOI: 10.1364/jocn.382654.

[42] O. Alkhalifah, O. Alrabiah, A. Ragheb, M. A. Esmail, and S. Alshebeili, "Investigation and demonstration of 5G signal transmission over fiber/FSO/wireless links", in *2017 International Conference on Electrical and Computing Technologies and Applications (ICECTA)*, 2017, pp. 1–4. DOI: 10.1109/ICECTA.2017.8252029.

[43] M. A. Esmail, A. M. Ragheb, H. A. Fathallah, M. Altamimi, and S. A. Alshebeili, "5g-28 GHz signal transmission over hybrid all-optical FSO/RF link in dusty weather conditions", *IEEE Access*, vol. 7, pp. 24 404–24 410, 2019. DOI: 10.1109/ACCESS.2019.2900000.

[44] H. K. Al-Musawi, T. Cseh, M. M. Abadi, W. P. Ng, Z. Ghassemlooy, E. Udvary, and T. Berceli, "Experimental demonstration of transmitting lte over fso for in-building pof networks", in *2015 17th International Conference on Transparent Optical Networks (ICTON)*, 2015, pp. 1–4. DOI: 10.1109/ICTON.2015.7193687.

[45] Z. N. Chen, D. Liu, H. Nakano, X. Qing, and T. Zwick, Eds., *Handbook of Antenna Technologies* (Springer eBook Collection). Singapore: Springer, 2016, 24731425 pp., ISBN: 9789814560443.

[46] J. Bohata, T. Lonsky, J. Spacil, P. Hazdra, Z. Hradecky, M. Komanec, S. Zvanovec, L. Vallejo, and B. Ortega, "Antenna phased array beamforming at 26 GHz using optical true time-delay", in *2020 12th International Symposium on Communication Systems, Networks and Digital Signal Processing (CSNDSP)*, IEEE, Jul. 2020. DOI: 10.1109/csndsp49049.2020.9249587. [Online]. Available: https://doi.org/10.1109/CSNDSP49049.2020.9249587.

[47] S. Akiba, M. Oishi, Y. Nishikawa, J. Hirokawa, and M. Ando, "Photonic approach to beam steering of phased array antenna", in *2013 International Symposium on Electromagnetic Theory*, 2013, pp. 448–451. [Online]. Available: https://ieeexplore.ieee.org/document/6565778.

[48] J. Bohata, M. Komanec, J. Spáčil, P. Hazdra, T. Lonský, Z. Hradecký, and S. Zvánovec, "Experimental demonstration of a microwave photonic link using an optically phased antenna array for a millimeter wave band", *Applied Optics*, vol. 60, no. 4, p. 1013, Jan. 2021, ISSN: 2155-3165. DOI: 10.1364/ao.414069. [Online]. Available: https://doi.org/10.1364/AO.414069.

[49] European Telecommunications Standards Institute, *Etsi ts 136 141 v15.7.0 (2020-04) lte; evolved universal terrestrial radio access (e-utra); base station (bs) conformance testing*, https://www.etsi.org/deliver/etsi_ts/136100_136199/136141/15.07.00_60/ts_136141v150700p.pdf, 2020.

[50] J. Bohata, M. Komanec, J. Spacil, S. Zvanovec, Z. Ghassemlooy, and R. Slavik, "Hybrid RoF-RoFSO system using directly modulated laser for 24 – 26 GHz 5G networks", in *2018 11th International Symposium on Communication Systems, Networks & Digital Signal Processing (CSNDSP)*, IEEE, Jul. 2018. DOI: 10.1109/csndsp.2018.8471867. [Online]. Available: https://doi.org/10.1109/CSNDSP.2018.8471867.

[51] J. Bohata, M. Komanec, J. Spacil, Z. Ghassemlooy, S. Zvanovec, and R. Slavik, "24-26 GHz radio-over-fiber and free-space optics for fifth-generation systems", *Optics Letters*, vol. 43, no. 5, p. 1035, Feb. 2018, ISSN: 1539-4794. DOI: 10.1364/ol.43.001035. [Online]. Available: https://doi.org/10.1364/OL.43.001035.

[52] A. Gupta and R. K. Jha, "A survey of 5G network: Architecture and emerging technologies", *IEEE Access*, vol. 3, pp. 1206–1232, 2015, ISSN: 2169-3536. DOI: 10.1109/access.2015.2461602. [Online]. Available: https://ieeexplore.ieee.org/document/7169508.

[53] European Telecommunications Standards Institute, *ETSI TS 136 104 V17.1.0 (2021-07) LTE; evolved universal terrestrial radio access (E-UTRA); base station (BS) radio transmission and reception*, https://www.etsi.org/deliver/etsi_ts/136100_136199/136104/17.01.00_60/ts_136104v170100p.pdf, 2021.

[54] D.-N. Nguyen, J. Bohata, J. Spacil, D. Dousek, M. Komanec, S. Zvanovec, Z. Ghassemlooy, and B. Ortega, "M-QAM transmission over hybrid microwave photonic links at the K-band", *Optics Express*, vol. 27, no. 23, p. 33 745, Nov. 2019, ISSN: 1094-4087. DOI: 10.1364/oe.27.033745. [Online]. Available: https://doi.org/10.1364/OE.27.033745.

[55] R. Li, X. Han, X. Chen, X. Chen, and J. Yao, "A phase-modulated microwave photonic link with an extended transmission distance", *IEEE Photonics Technology Letters*, vol. 27, no. 24, pp. 2563–2566, Dec. 2015, ISSN: 1941-0174. DOI: 10.1109/lpt.2015.2478135. [Online]. Available: https://ieeexplore.ieee.org/document/7258362.

[56] J. Bohata, M. Komanec, J. Spacil, R. Slavik, and S. Zvanovec, "Transmitters for combined radio over a fiber and outdoor millimeter-wave system at 25 GHz", *IEEE Photonics Journal*, vol. 12, no. 3, pp. 1–14, Jun. 2020, ISSN: 1943-0647. DOI: 10.1109/jphot.2020.2997976. [Online]. Available: https://doi.org/10.1109/JPHOT.2020.2997976.

[57] T. S. Rappaport, G. R. MacCartney, M. K. Samimi, and S. Sun, "Wideband millimeter-wave propagation measurements and channel models for future wireless communication system design", *IEEE Transactions on Communications*, vol. 63, no. 9, pp. 3029–3056, 2015, ISSN: 1558-0857. DOI: 10.1109/TCOMM.2015.2434384. [Online]. Available: https://ieeexplore.ieee.org/document/7109864.

[58] S. Sun, T. S. Rappaport, T. A. Thomas, A. Ghosh, H. C. Nguyen, I. Z. Kovács, I. Rodriguez, O. Koymen, and A. Partyka, "Investigation of prediction accuracy, sensitivity, and parameter stability of large-scale propagation path loss models for 5G wireless communications", *IEEE Transactions on Vehicular Technology*, vol. 65, no. 5, pp. 2843–2860, 2016, ISSN: 1939-9359. DOI: 10.1109/TVT.2016.2543139. [Online]. Available: https://ieeexplore.ieee.org/document/7434656.

[59] "NR; user equipment (UE) radio transmission and reception; part 2: Range 2 standalone", 3rd Generation Partnership Project (3GPP), Technical Specification 38.101-2, 2017. [Online]. Available: https://www.3gpp.org/DynaReport/38-series.htm.

[60] "NR user equipment (UE) radio transmission and reception; part 1: Range 1 standalone", 3rd Generation Partnership Project (3GPP), Technical Specification 38.101-1, 2017. [Online]. Available: https://www.3gpp.org/DynaReport/38-series.htm.

[61] J. Bohata, D. N. Nguyen, J. Spáčil, M. Komanec, B. Ortega, L. Vallejo, Z. Ghassemlooy, and S. Zvánovec, "Experimental comparison of DSB and CS-DSB mmW formats over a hybrid fiber and FSO fronthaul network for 5G", *Optics Express*, vol. 29, no. 17, p. 27 768, Aug. 2021, ISSN: 1094-4087. DOI: 10.1364/oe.434334. [Online]. Available: https://doi.org/10.1364/OE.434334.

[62] "ETSI TS 138 141-1 V15.3.0 (2019-10)", European Telecommunications Standards Institute, Technical Specification TS 138 141-1 V15.3.0, Oct. 2019, Accessed: Date-of-Access. [Online]. Available: https://www.etsi.org/deliver/etsi_ts/138100_138199/13814101/15.03.00_60/ts_13814101v150300p.pdf.

[63] F. Walls and C. Felton, "Low noise frequency synthesis", in *41st Annual Symposium on Frequency Control*, IEEE, 1987, pp. 512–518. [Online]. Available: http://tf.nist.gov/general/pdf/715.pdf.

[64] J. Spáčil, J. Bohata, D.-N. Nguyen, M. Mazánek, and S. Zvánovec, "Effect of erbium-doped fiber amplifier loss compensation on 5G new radio millimeter-wave seamless transmission over analog fiber and free space optical fronthaul at 60 GHz", *Optical Engineering*, vol. 61, no. 06, Jun. 2022, ISSN: 0091-3286. DOI: 10.1117/1.oe.61.6.066104. [Online]. Available: https://doi.org/10.1117/1.OE.61.6.066104.

[65] J. Bohata, D.-N. Nguyen, J. Spáčil, D. Suslov, D. Dousek, S. Zvánovec, Z. Ghassemlooy, and M. Komanec, "Performance evaluation of seamless 5G outdoor RoFSO transmission at 39 GHz", *IEEE Photonics Technology Letters*, pp. 1–1, 2021. DOI: 10.1109/LPT.2021.3134559. [Online]. Available: https://ieeexplore.ieee.org/document/9645565.

[66] A. W. Setiawan Putra, M. Yamada, H. Tsuda, and S. Ambran, "Theoretical analysis of noise in erbium doped fiber amplifier", *IEEE Journal of Quantum Electronics*, vol. 53, no. 4, pp. 1–8, 2017, ISSN: 1558-1713. DOI: 10.1109/JQE.2017.2717703. [Online]. Available: https://ieeexplore.ieee.org/document/7953635.

[67] D. Che, "Analog vs digital radio-over-fiber: A spectral efficiency debate from the SNR perspective", *Journal of Lightwave Technology*, vol. 39, no. 16, pp. 5325–5335, 2021, ISSN: 1558-2213. DOI: 10.1109/JLT.2021.3102220. [Online]. Available: https://ieeexplore.ieee.org/document/9507332.

[68] L. Vallejo, B. Ortega, J. Mora, D.-N. Nguyen, C. Guerra, J. Bohata, J. Spacil, and S. Zvanovec, "Demonstration of M-QAM OFDM bidirectional 60/25 GHz transmission over 10 km fiber, 100 m FSO and 2 m radio seamless heterogeneous fronthaul link", *Optical Fiber Technology*, vol. 77, p. 103 161, May 2023, ISSN: 1068-5200. DOI: 10.1016/j.yofte.2022.103161. [Online]. Available: https://linkinghub.elsevier.com/retrieve/pii/S1068520022003455.

[69] D.-N. Nguyen, J. Bohata, J. Spacil, M. Komanec, N. Stevens, Z. Ghassemlooy, P. T. Dat, and S. Zvanovec, "Polarization division multiplexing-based hybrid microwave photonic links for simultaneous mmW and Sub-6 GHz wireless transmissions", *IEEE Photonics Journal*, vol. 12, no. 6, pp. 1–14, Dec. 2020, ISSN: 1943-0647. DOI: 10.1109/jphot.2020.3036440. [Online]. Available: https://doi.org/10.1109/JPHOT.2020.3036440.

[70] Z. Hradecký, J. Bohata, M. Komanec, S. Zvánovec, P. Hazdra, J. Spáčil, and T. Lonský, *Radio-optical transmission terminal*, 2020.

[71] P. Hazdra, M. Komanec, J. Bohata, S. Zvánovec, T. Lonský, Z. Hradecký, and J. Spáčil, *Equipment with radio terminal*, Czech, 2020.

[72] B. Tamrakar, K. Singh, and V. Gupta, "Tackling third-order intermodulation distortion: Modeling and analysis of linearized RoF link for future perspective networks", *Journal of Optics*, Oct. 2023, ISSN: 0974-6900. DOI: 10.1007/s12596-023-01432-2.

List of candidate's work related to the thesis

The percentage is even for all listed authors at each publication.

Journals (Impact)

- J. Spáčil, J. Bohata, D.-N. Nguyen, M. Mazánek, and S. Zvánovec, "Effect of erbium-doped fiber amplifier loss compensation on 5G new radio millimeter-wave seamless transmission over analog fiber and free space optical fronthaul at 60 GHz", *Optical Engineering*, vol. 61, no. 06, Jun. 2022, ISSN: 0091-3286. DOI: 10.1117/1.oe.61.6.066104. [Online]. Available: https://doi.org/10.1117/1.OE.61.6.066104

- L. Vallejo, B. Ortega, J. Mora, D.-N. Nguyen, C. Guerra, J. Bohata, J. Spacil, and S. Zvanovec, "Demonstration of M-QAM OFDM bidirectional 60/25 GHz transmission over 10 km fiber, 100 m FSO and 2 m radio seamless heterogeneous fronthaul link", *Optical Fiber Technology*, vol. 77, p. 103 161, May 2023, ISSN: 1068-5200. DOI: 10.1016/j.yofte.2022.103161. [Online]. Available: https://linkinghub.elsevier.com/retrieve/pii/S1068520022003455

  This article has been cited 2 times, according to V3S.

- J. Bohata, M. Komanec, J. Spacil, Z. Ghassemlooy, S. Zvanovec, and R. Slavik, "24-26 GHz radio-over-fiber and free-space optics for fifth-generation systems", *Optics Letters*, vol. 43, no. 5, p. 1035, Feb. 2018, ISSN: 1539-4794. DOI: 10.1364/ol.43.001035. [Online]. Available: https://doi.org/10.1364/OL.43.001035

  This article has been cited 57 times, according to V3S without self-citations.

- D.-N. Nguyen, J. Bohata, J. Spacil, D. Dousek, M. Komanec, S. Zvanovec, Z. Ghassemlooy, and B. Ortega, "M-QAM transmission over hybrid microwave photonic links at the K-band", *Optics Express*, vol. 27, no. 23, p. 33 745, Nov. 2019, ISSN: 1094-4087. DOI: 10.1364/oe.27.033745. [Online]. Available: https://doi.org/10.1364/OE.27.033745

  This article has been cited 35 times, according to V3S without self-citations.

- J. Bohata, M. Komanec, J. Spacil, R. Slavik, and S. Zvanovec, "Transmitters for combined radio over a fiber and outdoor millimeter-wave system at 25 GHz", *IEEE Photonics Journal*, vol. 12, no. 3, pp. 1–14, Jun. 2020, ISSN: 1943-0647. DOI: 10.1109/jphot.2020.2997976. [Online]. Available: https://doi.org/10.1109/JPHOT.2020.2997976

  This article has been cited 4 times, according to V3S without self-citations.

- D.-N. Nguyen, J. Bohata, J. Spacil, M. Komanec, N. Stevens, Z. Ghassemlooy, P. T. Dat, and S. Zvanovec, "Polarization division multiplexing-based hybrid microwave photonic links for simultaneous mmW and Sub-6 GHz wireless transmissions", *IEEE Photonics Journal*, vol. 12, no. 6, pp. 1–14, Dec. 2020, ISSN: 1943-0647. DOI: 10.1109/jphot.2020.3036440. [Online]. Available: https://doi.org/10.1109/JPHOT.2020.3036440

  This article has been cited 14 times, according to V3S.

- J. Bohata, M. Komanec, J. Spáčil, P. Hazdra, T. Lonský, Z. Hradecký, and S. Zvánovec, "Experimental demonstration of a microwave photonic link using an optically phased antenna array for a millimeter wave band", *Applied Optics*, vol. 60, no. 4, p. 1013, Jan. 2021, ISSN: 2155-3165. DOI: 10.1364/ao.414069. [Online]. Available: https://doi.org/10.1364/AO.414069

  This article has been cited 3 times, according to V3S.

- J. Bohata, D. N. Nguyen, J. Spáčil, M. Komanec, B. Ortega, L. Vallejo, Z. Ghassemlooy, and S. Zvánovec, "Experimental comparison of DSB and CS-DSB mmW formats over a hybrid fiber and FSO fronthaul network for 5G", *Optics Express*, vol. 29, no. 17, p. 27 768, Aug. 2021, ISSN: 1094-4087. DOI: 10.1364/oe.434334. [Online]. Available: https://doi.org/10.1364/OE.434334

  The paper has been cited in: This article has been cited 9 times, according to V3S.

- J. Bohata, D.-N. Nguyen, J. Spáčil, D. Suslov, D. Dousek, S. Zvánovec, Z. Ghassemlooy, and M. Komanec, "Performance evaluation of seamless 5G outdoor RoFSO transmission at 39 GHz", *IEEE Photonics Technology Letters*, pp. 1–1, 2021. DOI: 10.1109/LPT.2021.3134559. [Online]. Available: https://ieeexplore.ieee.org/document/9645565

  This article has been cited 13 times, according to V3S without self-citations.

Conferences

- J. Bohata, M. Komanec, J. Spacil, S. Zvanovec, Z. Ghassemlooy, and R. Slavik, "Hybrid RoF-RoFSO system using directly modulated laser for 24 – 26 GHz 5G networks", in *2018 11th International Symposium on Communication Systems, Networks & Digital Signal Processing (CSNDSP)*, IEEE, Jul. 2018. DOI: 10.1109/csndsp.2018.8471867. [Online]. Available: https://doi.org/10.1109/CSNDSP.2018.8471867

  This article has been cited 6 times, according to V3S without self-citations.

- J. Bohata, J. Spacil, D.-N. Nguyen, S. Zvanovec, L. Vallejo, and B. Ortega, "Radio over 50 km fiber and joint 80 m FSO/wireless links using photonic frequency doubling for 5G", in *2019 IEEE Global Communications Conference (GLOBECOM)*, IEEE, Dec. 2019. DOI: 10.1109/globecom38437.2019.9013212. [Online]. Available: https://doi.org/10.1109/GLOBECOM38437.2019.9013212

  This article has been cited 3 times, according to V3S without self-citations.

- J. Bohata, T. Lonsky, J. Spacil, P. Hazdra, Z. Hradecky, M. Komanec, S. Zvanovec, L. Vallejo, and B. Ortega, "Antenna phased array beamforming at 26 GHz using optical true time-delay", in *2020 12th International Symposium on Communication Systems, Networks and Digital Signal Processing (CSNDSP)*, IEEE, Jul. 2020. DOI: 10.1109/csndsp49049.2020.9249587. [Online]. Available: https://doi.org/10.1109/CSNDSP49049.2020.9249587

Applied results

- Z. Hradecký, J. Bohata, M. Komanec, S. Zvánovec, P. Hazdra, J. Spáčil, and T. Lonský, *Radio-optical transmission terminal*, 2020
- P. Hazdra, M. Komanec, J. Bohata, S. Zvánovec, T. Lonský, Z. Hradecký, and J. Spáčil, *Equipment with radio terminal*, Czech, 2020

List of candidate's work non-related to the thesis

Papers in Peer-Reviewed Journals with Impact Factor

- T. Korinek, M. Valek, J. Spacil, and M. Mazanek, "Pre-assessment of radiated fields from small electronic submodules", *Radioengineering*, vol. 27, no. 3, pp. 640–645, Sep. 2018, ISSN: 1210-2512. DOI: 10.13164/re.2018.0640

Conferences

- M. Komanec, P. Vidner, J. Spacil, D. Suslov, P. Pesek, T. Nemecek, and S. Zvanovec, "Polarization-maintaining fiber-optic gyroscope using a closed-loop with kalman filtering", in *29th Conference and Exhibition on OPTICAL COMMUNICATIONS 2018*, 2018

Applied results

- J. Kraček, T. Kořínek, V. Kabourek, M. Mazánek, M. Švanda, T. Lonský, and J. Spáčil, "Analysis of uncertainties by TEMPEST measurement for NÚKIB facility", CTU FEE. Department of Electromagnetic Field, Tech. Rep., 2018